DISSERTATION | DOCTORAL THESIS

Titel | Title

Derivation and Analysis of Biological Kinetic Models: Diffusion in Channels, Collective Behaviour, Coagulation Phenomena

verfasst von | submitted by

Dott.ssa Dott.ssa mag. Carmela Moschella

angestrebter akademischer Grad | in partial fulfilment of the requirements for the degree of

Doktorin der Naturwissenschaften (Dr.rer.nat.)

Wien | Vienna, 2025

Studienkennzahl lt. Studienblatt | Degree programme code as it appears on the student record sheet:	UA 796 605 405
Dissertationsgebiet lt. Studienblatt | Field of study as it appears on the student record sheet:	Mathematik
Betreut von | Supervisor:	ao. Univ.-Prof. i.R. Dr. Christian Schmeiser Univ.-Prof. Sara Merino Aceituno PhD

Abstract

This thesis contributes to the mathematical analysis of kinetic equations describing emergent phenomena in biological systems through asymptotic analyses. This framework connects individual-based models, characterized by microscopic interactions, with macroscopic equations formulated as partial differential equations (PDEs). The manuscript is organized into four major sections, each addressing a different question in the application of kinetic theory to biological systems. The first part focuses on a third-order stochastic differential equation (SDE) system that combines orientation alignment dynamics with angular velocity synchronization to describe the collective behavior of flagellated bacteria. From this agent-based model, we derive hydrodynamic equations using the concept of Generalized Collision Invariants, yielding a macroscopic system for the density, mean direction, and angular velocity of particles. Numerical simulations of the particle system reveal diverse emergent patterns, including rotating clusters, traveling orientation waves, and pulsating dynamics, which are compared to simulations of the macroscopic model. Motivated by biological phenomena where interactions between multiple agents occur over finite time spans and involve continuous state changes, the second part of the manuscript extends the classical kinetic theory to account for non-instantaneous, multi-particle collisions. Inspired by coagulation-fragmentation processes, we introduce a system of equations governing the evolution of cluster distribution densities $f_k(v_1, ..., v_k)$. We first derive a first-order correction to the instantaneous model that captures the effects of finite duration interactions. We then establish the well-posedness of the approximated model and its convergence to the classical instantaneous kinetic equation in the limit as the interaction duration tends to zero. This result confirms that the first-order correction yields a consistent approximation of the instantaneous model in the regime of short interaction times. Furthermore, the third section examines the existence of steady-state solutions to a transport-coagulation-nucleation equation that models aggregate formation in biological processes, particularly autophagy. Under suitable decay assumptions on the transport velocity, the existence of non-trivial stationary solutions with finite mass is established via Schauder fixed-point theorem. Lastly, the thesis explores protein transport mechanisms within the cell, specifically between the endoplasmatic reticulum and the nuclear envelope. We introduce a simplified diffusion model, from which asymptotic analysis provides explicit expressions for transport rates in agreement with experimental data, illustrating how

the geometry of intracellular compartments can influence the transport of some proteins within the cell.

Zusammenfassung

Diese Dissertation leistet einen Beitrag zur mathematischen Analyse kinetischer Gleichungen, die mittels asymptotischer Analysen emergente Phänomene in biologischen Systemen beschreiben. Im Zuge dessen werden agentenbasierte Modelle, die durch mikroskopische Interaktionen beschrieben werden, mit makroskopischen Gleichungen, die mittels partielle Differentialgleichungen (PDEs) formuliert werden, verknüpft

Die vorliegende Arbeit ist in vier Abschnitte gegliedert, von denen jeder eine andere Fragestellung bezüglich der Anwendung der kinetischen Theorie auf biologische Systeme behandelt.

Der erste Abschnitt behandelt ein System stochastischer Differentialgleichungen dritter Ordnung, das Orientierungsangleichung und Synchronisation der Winkelgeschwindigkeit kombiniert, um das kollektive Verhalten flagellierter Bakterien zu beschreiben. Ausgehend von diesem agentenbasierten Modell leiten wir mithilfe des Konzepts der "Generalized Collision Invariants" hydrodynamische Gleichungen her. Diese beschreiben ein makroskopisches System für die Dichte, die mittlere Richtung und die Winkelgeschwindigkeit der Partikel. Numerische Simulationen des individuenbasierten Systems zeigen vielfältige emergente Muster, darunter rotierende Cluster, wandernde Wellen bezüglich der Orientierung und pulsierende Dynamiken, die mit Simulationen des makroskopischen Modells verglichen werden.

Motiviert durch biologische Phänomene, bei denen Wechselwirkungen zwischen mehreren Individuen über endliche Zeitspannen stattfinden und kontinuierliche Zustandsänderungen beinhalten, erweitert der zweite Teil der Dissertation die klassische kinetische Theorie, um nicht-instantane Mehrteilchenkollisionen zu berücksichtigen. Inspiriert von Koagulations-Fragmentations-Prozessen führen wir ein Gleichungssystem ein, das die Entwicklung der Cluster-Verteilungsdichten $f_k(v_1, \dots, v_k)$ beschreibt. Zunächst leiten wir eine Korrektur erster Ordnung des instantanen Modells her, die die Effekte von Wechselwirkungen mit endlicher Dauer erfasst. Anschließend zeigen wir die Wohlgestelltheit des approximierten Modells und seine Konvergenz zur klassischen instantanen kinetischen Gleichung wenn die Wechselwirkungsdauer gegen Null strebt. Dieses Ergebnis bestätigt, dass die Korrektur erster Ordnung im Regime kurzer Interaktionszeiten eine konsistente Approximation des instantanen Modells liefert.

Darüber hinaus untersucht der dritte Abschnitt die Existenz stationärer Lösungen einer Transport-Koagulations-Nukleations-Gleichung, die die Bildung von Aggregaten in biologischen Prozessen, insbesondere in der Autophagie, modelliert. Unter geeigneten Abklingannahmen für die Transportgeschwindigkeit wird mittels des Fixpunktsatzes von Schauder die Existenz nicht-trivialer stationärer Lösungen mit endlicher Masse nachgewiesen.

Abschließend untersucht die Arbeit Proteintransportmechanismen innerhalb der Zelle, insbesondere zwischen dem endoplasmatischen Retikulum und der Kernhülle. Wir stellen ein vereinfachtes Diffusionsmodell vor, aus dessen asymptotischer Analyse sich explizite Ausdrücke für Transportraten ergeben, die mit experimentellen Daten übereinstimmen und verdeutlichen, wie die Geometrie intrazellulärer Kompartimente den Transport bestimmter Proteine beeinflussen kann.

Contents

Front Matter **i**

Abstract . . . iii
Zusammenfassung . . . v
List of Tables . . . xi
List of Figures . . . xiii
List of Symbols . . . xix

Introduction **1**

1 From microscopic dynamics to macroscopic models . . . 1
1.1 Models of collective motion — Some examples . . . 3
1.2 The mean field description . . . 8
1.3 The macroscopic description . . . 10
2 Chapter summaries . . . 10
2.1 A third-order model for collective dynamics . . . 10
2.2 Non-instantaneous and non-binary collisions . . . 13
2.3 Stationary solutions for a Coagulation–Transport–Nucleation equation 16
2.4 Modeling protein transport between the Endoplasmic Reticulum and the Nuclear Envelope . . . 19

1 Collective dynamics with alignment and rotation synchronisation **23**

1 Introduction . . . 24
2 Individual-Based model, mean-field limit and scaling . . . 27
2.1 The IBM . . . 27
2.2 Mean–field equations . . . 28
2.3 Scaling of the kinetic model (1.10) . . . 29
3 Macroscopic limit . . . 31
3.1 Generalized collisional invariant . . . 33
3.2 Proof of theorem 3.1 . . . 35
3.3 Periodic solutions . . . 39
4 Simulation of the microscopic model . . . 39

4.1 Numerical integration of the particle system 40
4.2 Patterns: phase diagrams 40
5 Simulation of the macroscopic model 43
5.1 Comparison between microscopic and macroscopic simulations . . 46
5.2 Conclusions 47

2 Non-Instantaneous corrections in kinetic alignment models 51
1 Introduction 51
2 System of non-instantaneously interacting particles 53
3 Well-posedness and instantaneous limit for the first order accurate model 60
3.1 Dynamics of the moments 61
3.2 Existence and uniqueness 63
3.3 Instantaneous limit 65
4 A first order accurate, non-instantaneous, scalar model 68

3 Steady states of Transport-Coagulation-Nucleation models 71
1 Introduction 72
2 The choice of the transport velocity 73
3 The inverse problem – explicit examples of steady state solutions 75
4 Existence and properties of steady states 77
4.1 Qualitative properties of steady states 81
5 Numerical results 82
5.1 Comparison with exact solutions 83
5.2 Behavior of the numerical solution close to $\boldsymbol{x_0}$ 84

4 Protein Diffusion Across ER–NE Junctions 89
1 Introduction 90
2 Materials and methods 91
2.1 Cell culture 91
2.2 Live cell imaging and photobleaching 91
2.3 Quantification of diffusion coefficient and transport rate constant 92
2.4 Shape of ER-NE junctions 92
2.5 The mathematical model 93
3 Results 94
3.1 Live-cell reporters for quantifying luminal protein flux 94
3.2 Quantifying ER-to-NE protein flux using photobleaching 95
3.3 Prediction of the transport rate by the mathematical model . . . 95
3.4 Comparison between experimental observations and model predictions 96
4 Discussion 97

Appendices **103**

A List of supplementary videos to Chapter 1 **105**

1 Particle simulations 105

2 Macroscopic simulations 106

B Supplementary numerical results to Chapter 3 **107**

C Derivation of the mathematical model of Chapter 4 **111**

Bibliography **113**

List of Tables

1.1 **Parameters used for the microscopic simulations.** The values considered for k_θ and k_ω are specified in the caption of the corresponding figures. 41

4.1 **Parameters values used in the mathematical model.** Apparent diffusion coefficients for the small and large protein reporters were obtained from FRAP measurements (Figure 1B,C). Volumes of the ER and the NE are based on data from volume electron microscopy studies [64], [73]. Junction number and radius were quantified using electron tomography, as described in a previous study [19]. Although two types of junctions were identified in that study (those with and without lumen), only lumen-containing junctions were included in the model, as junctions lacking lumen are unlikely to contribute to luminal ER-to-NE transport. A correction factor was applied to account for a 17% shrinkage caused by the electron microscopy process. 97

List of Figures

1 **Various examples of self-organised collective behaviour. (a)** A flock of starlings forming complex aerial patterns above Rome (pictured by *Søren Solkær*). **(b)** A school of fish exhibiting coordinated vortex-like motion (Source: Ocean Photographer of the Year 2022). **(c)** Spontaneous lane formation in a dense pedestrian crowd (taken from [65]). 1

2 **The three-body problem.** Approximate trajectories of three identical bodies initially placed at the vertices of a scalene triangle and subject to mutual gravitational attraction. The coloured curves represent the paths of the bodies in the plane, while the grey lines connect their positions (black crosses). The centre of mass (orange cross) remains fixed, in accordance with the conservation of the momentum. 2

3 **Comparison of microscopic interaction rules. (a)** *Boltzmann hard-sphere collision*: particles interact via elastic collisions. Two particles i, j collide with velocities $\boldsymbol{v}_i$ and $\boldsymbol{v}_j$. After the collision, particles adopt velocities $\boldsymbol{v}_i'$ and $\boldsymbol{v}_j'$. During the collision mass, momentum, and kinetic energy are conserved, and the dynamics is time-reversible. **(b)** *Alignment-type interaction*: self-propelled agents with velocities $\boldsymbol{v}_i$ and $\boldsymbol{v}_j$ within a finite sensing radius (dashed) adjust their direction toward the local average velocity depicted as $\langle \boldsymbol{v} \rangle$. Momentum and energy are not conserved during the interaction, and the dynamics is irreversible. 4

4 **Velocity evolution as a jump process driven by collisions.** Particles are in free flight and move at constant speeds v_0, v_1, v_2 (horizontal segments). Collisions occur at exponentially distributed times T_i^1, T_i^2, T_i^3; each collision produces an instantaneous jump in velocity from v_{k-1} to v_k. 8

5 **Velocity evolution with stochastic finite-duration collisions.** Horizontal segments represent free flight phase. During each collision interval $\left[T_{i,\text{in}}^k, T_{i,\text{out}}^k\right]$ the velocity relaxes toward a target value prescribed by the alignment dynamics of the model. Because the exit time $T_{i,\text{out}}^k$ is random, the interaction may end before full alignment is achieved. 14

6 **Coagulation dynamics.** Binary coagulation of particles x and y forming a particle of size $x + y$. The coagulation rate is given by the coagulation kernel $K(x, y)$. 17

7 **Schematic of the model domain.** Proteins diffuse passively from the endoplasmic reticulum (ER) to the nuclear envelope (NE) through narrow junctions. The model parameters include the ER and NE volumes V_{ER} and V_{NE}, the diffusion coefficient D, the number of junctions k, the junction length L, and its base radius R. The angle α characterizes the conical geometry of the junctions. The image has been provided by the group of Shotaro Otsuka (Max Perutz Laboratories). 20

1.1 Results of microscopic simulations for varying values of the alignment parameters k_θ and k_ω, with all other parameters fixed as reported in Table 1.1. Each simulation involves 15,000 agents interacting within an interaction radius $R = 2$. The columns (from left to right) correspond to increasing values of the angular velocity alignment strength $k_\omega = 1, 11, 51, 61, 81$, while the rows (from bottom to top) correspond to increasing values of the directional alignment strength $k_\theta = 1, 11, 21, 61, 71$. The colormap, shown on the right hand side of the figure, provides the correspondence between orientation angles and colors. 43

1.2 Sequence of snapshots showing the emergence of a traveling wave in orientation for alignment parameters $k_\theta = 21$ and $k_\omega = 81$. The system evolves towards a state with nearly uniform spatial density, while the orientation field propagates with a wave-like motion across the domain. The corresponding video can be found in Appendix A (Video 2). 44

1.3 Sequence of snapshots illustrating the steady-state dynamics for alignment parameters $k_\theta = k_\omega = 71$. To highlight the pulsating behavior, we display multiple time frames from the same simulation. The particles rotate collectively as a rigid body, with the orientation field evolving in time across the entire domain. This global rotation characterizes the pulsating regime, where the direction of motion changes uniformly for all the particles in the domain, while the distribution of particles remains uniform in space. The corresponding video can be found in Appendix A (Video 3). 44

1.4 Macroscopic simulation of the Vicsek–Kuramoto system with $k_\theta/\alpha^2 = 8$. **(a)** Snapshot at early time $t = 0.20$, showing the formation of localized rotating clusters. These are transient structures similar to those observed in the microscopic simulations with small k_θ and k_ω, corresponding to weak orientational and angular velocity alignment. The color scale represents the density $\rho(x,t)$, while arrows indicate the local mean orientation field $\Omega(x,t)$ computed in each grid cell. The video of the simulation is included in Appendix A (Video 5) **(b)** Same configuration as in (a), with the color scale representing the average orientation angle of each cell grid between $[-\pi,\pi]$. The video of the simulation is included in Appendix A (Video 6) **(c)** Snapshot of Video 5 at time $t = 95.0$. The density ρ becomes nearly uniform in space, and the system reaches a rotating regime driven by a non-zero mean average angular velocity. **(d)** Snapshot of Video 6 at time t =95, with colorbar indicating the angle. The global coherent rotation of the direction field confirms the emergence of a pulsating state, in qualitative agreement with the behavior observed in the microscopic simulations of Video 4. 48

3.1 **Comparison of the numerical and exact steady state solution for $K(x,y) = 2$.** The left figure shows the initial profile of the numerical solution (green line), a snapshot of the numerical solution after 200 time steps (blue line), and the exact analytical solution derived in Section 3 (red dashed line). The right figure compares the numerical solution at final time (blue line) and the exact steady state solution computed in Section 4.1 (red dashed line). The peak of the numerical solution on the right at x_0 (gray vertical line) is a numerical error caused by the discontinuity of the numerical flux at x_0. This error diminishes as the spatial grid is refined, as evidenced by the decreasing L^1 discrete error norm plotted in Figure 3.2. 84

3.2 **Time evolution of the L^1-discrete error norm for $K(x,y) = 2$.** **(a)** Discrete L^1-error in linear scale. The error decreases with respect to smaller values of Δx. The results are showed for $\Delta x = 0.12$ (blue dashed line), $\Delta x = 0.06$ (green dashed line) and $\Delta x = 0.03$ (gray dashed line). **(b)** Discrete L^1-error in semi-log scale, showing polynomial decay in time. . . 85

3.3 **Behavior of the numerical solution near x_0 for $K(x, y) = xy$. (a)** Numerical solution at the final time for different values of Δx, for $c < 1$. The results are shown for $\Delta x = 0.027$ (green dashed line), $\Delta x = 0.014$ (red dashed line), and $\Delta x = 0.0093$ (blue solid line). **(b)** Numerical solution at the final time for different values of Δx, for $c = 1$. **(c)** Numerical solution at the final time for different values of Δx, for $c > 1$. The results are shown for $\Delta x = 0.027$ (blue solid line), $\Delta x = 0.014$ (red dashed line), and $\Delta x = 0.0093$ (green dashed line). **(d)** Plot of the maximum value of the numerical solution at final time near x_0 for different values of Δx. The blue line corresponds to the case $c < 1$, the red line to $c = 1$, and the gray line to $c > 1$. 87

4.1 **Quantifying ER-to-NE transport of luminal proteins. (A)** Illustration of two reporters used to measure intraluminal protein transport between the ER and NE. **(B)** Representative images of HeLa cells expressing the transport reporters: moxGFP-KDEL (top) and NusA-moxGFPx2-KDEL (bottom). Diffusion within the ER was monitored by photobleaching a small region (indicated by the green line) and tracking fluorescence recovery over time. **(C)** Fluorescence intensity in the bleached area was quantified for moxGFP-KDEL (top) and NusA-moxGFPx2-KDEL (bottom). Experimental data (black triangles) and simulated diffusion curves (gray lines) for the cells shown in (B) are shown. **(D)** Photobleaching in fixed cells to assess the degree of fluorescence loss across the entire NE, serving as a control for ER-to-NE transport measurements. The left panels show a HeLa cell expressing moxGFP-KDEL before (top) and after (bottom) photobleaching the entire NE. Orthogonal views of the indicated positions (white dashed lines) are shown on the right. **(E)** ER-to-NE diffusion of two reporters was monitored following photobleaching of the entire NE, indicated by white dotted lines. **(F)** Fluorescence intensity at the NE was quantified. Black and gray lines represent the mean and standard deviation (s.d.) of measurements from 40 cells across 4 independent experiments for moxGFP-KDEL (top) and 71 cells across 4 independent experiments for NusA-moxGFPx2-KDEL (bottom). Scale bars: 10 μm. 98

4.2 **The differential equation model with a geometric constraint predicted ER-to-NE flux that closely matches the experimental data.** **(A)** Schematic illustration of the parameters used in the mathematical model. **(B)** Membrane profiles of the ER-NE junction from a previous study [19]. Although two types of junctions were identified in that study (those with a visible lumen and those without), only lumen- containing junctions were included in the model, as the non-luminal junctions are unlikely to support luminal ER-to-NE transport. The averaged shape of the junction neck, highlighted by a bold rectangle in the left panel, is shown in the right panel. **(C,D)** Simulated ER-to-NE diffusion at different junction length **(C)** and membrane angles **(D)** (green dotted lines) compared with experimental data from Figure 1E,F (black solid line) for moxGFP-KDEL. **(E,F)** Simulated ER-to-NE diffusion at different junction length **(E)** and membrane angles **(F)** (green dotted lines) compared with experimental data from Figure 1E,F (black solid line) for NusA-moxGFPx2-KDEL. . 99

B.1 **Comparison of the numerical and exact steady state solution for $K(x, y) = x + y$.** The left figure shows the initial profile of the numerical solution (green line), a snapshot of the numerical solution after 200 time steps (blue line), and the exact analytical solution (red dashed line). The right figure compares the numerical solution at final time (blue line) and the exact steady state solution (red dashed line). The peak of the numerical solution on the right at x_0 (gray vertical line) is a numerical error caused by the discontinuity of the numerical flux at x_0. This error diminishes as the spatial grid is refined, as evidenced by the decreasing L^1 discrete error norm plotted in Figure B.2. 108

B.2 **Time evolution of the L^1-discrete error norm for $K(x, y) = x + y$.** **(a)** Discrete L^1-error in linear scale. The error decreases with respect to smaller values of Δx. The results are showed for $\Delta x = 0.12$ (blue dashed line), $\Delta x = 0.06$ (green dashed line) and $\Delta x = 0.03$ (gray dashed line). **(b)** Discrete L^1-error in semi-log scale. Although the error decreases over time, it does not follow a clear decay trend. 108

B.3 **Comparison of the numerical and exact steady state solution for $K(x, y) = xy$.** The corresponding L^1 discrete error norm is plotted in Figure B.4. 109

B.4 **Time evolution of the L^1-discrete error norm for $K(x, y) = xy$.** **(a)** Discrete L^1-error in linear scale. The error decreases with respect to smaller values of Δx. The results are showed for $\Delta x = 0.12$ (blue dashed line), $\Delta x = 0.06$ (green dashed line) and $\Delta x = 0.03$ (gray dashed line). **(b)** Discrete L^1-error in semi-log scale. As in the case of the linear coagulation kernel, the error decreases over time, but it does not follow a clear decay trend. 109

C.1 **Cross-sectional slice of a junction** 112

List of Symbols

Sets

$C(E)$	Continuous functions on E.
$C_B(E)$, $C_B^k(E)$	Bounded continuous functions on E; functions with $k \geq 1$ bounded continuous derivatives on E.
$L^p(E)$ $(p \geq 1)$	Set of measurable functions φ defined almost everywhere on a measured space (E, μ) such that $\lvert\varphi\rvert^p$ is integrable for $p \geq 1$. When $p = +\infty$, this is the set of functions with a bounded essential supremum.
$\mathcal{M}^+(E)$	Positive measures on E.
$\mathcal{P}(E)$	Probability measures on E.
$\mathbb{R}^+$	Interval $[0, +\infty)$.
$\mathbb{R}^d$	d-dimensional Euclidean space.
$\mathbb{S}^{d-1}$	Unit sphere of dimension $d-1$.

Generic elements and operators

$\binom{k}{j}$	Binomial coefficient defined as $\frac{k!}{j!(k-j)!}$.
$C(k, j)$	Set of j-combinations of $\{1, \ldots, k\}$, with $k \geq j$.
$\nabla \cdot V$	Divergence of a vector field $V : \mathbb{R}^d \to \mathbb{R}^d$ or of a matrix field $V : \mathbb{R}^d \to \mathcal{M}_d(\mathbb{R})$ is respectively defined by $\nabla \cdot V = \sum_{i=1}^d \partial_{x_i} V_i$ or componentwise by $(\nabla \cdot V)_i = \sum_{j=1}^d \partial_{x_j} V_{ij}$.
Id	Identity 2×2 matrix.
$x \cdot y$	Euclidean inner product $\sum_i x_i y_i$.
$P_{u^\perp}$	Projection matrix $\mathrm{Id} - \Omega \otimes \Omega$ on the plane orthogonal to the vector $u \in \mathbb{R}^d$.

$u \otimes v$, $\mu \otimes \nu$	Respectively, the matrix tensor product of two vectors $u, v \in \mathbb{R}^d$, defined componentwise by $(u \otimes v)_{ij} = u_i v_j$; the product measure on $E \times F$ of two measures μ, ν respectively on E and F.
x, $\lvert x \rvert$	Generic vector and its Euclidean norm.

Probability and measures

δ_x	Dirac measure at x.
$\delta(x)$	Delta distribution at x.
$\mathcal{L}(X)$	Distribution of X.
E	State space of the particles.
$X \sim \mu$	Random variable X has law μ.
f_t^N	N-particle distribution in $\mathcal{P}(E^N)$ at time $t \geq 0$.
$f_t^{N,(k)}$	k-th marginal of f_t^N, defined as $\int f_t^N(x_1, \ldots, x_k, x_{k+1}, \ldots, x_N)\, \mathrm{d}x_{k+1} \cdots \mathrm{d}x_N$.
$f_t^{\otimes k}$	Tensor product measure in $\mathcal{P}(E^k)$ at time $t \geq 0$.
f_t	Limit law in $\mathcal{P}(E)$.
μ_t^N	Empirical measure of a system of N particles $\frac{1}{N}\sum_{i=1}^N \delta_{x^i}$.
f_k^*	Evaluation of the distribution of groups of size k at a fixed configuration $(v_1^*, \ldots, v_k^*) \in (\mathbb{R}^d)^k$.
$f_j \odot f_{k-j}$	Symmetric tensor product of f_j and f_{k-j}, defined as $\binom{k}{j}^{-1} \sum_{c \in C(k,j)} f_j(v_c) f_{k-j}(v_{c'})$, where c' is the complement of $C(k,j)$.

Acronyms

CFL	Courant–Friedrichs–Lewy condition
ER	Endoplasmatic Reticulum
FRAP	Fluorescence Recovery After Photobleaching
GCI	Generalised Collision Invariant
IBM	Individual Based Model
NE	Nuclear Envelope
ODE	Ordinary Differential Equation
PDE	Partial Differential Equation

PDMP	Piecewise-Deterministic Markov Process
PTWA	Persistent Turning Walker with Alignment
SDE	Stochastic Differential Equation
SOH	Self-Organized Hydrodynamics

Introduction

1 From microscopic dynamics to macroscopic models

One of the key challenges in life science modelling is explaining how complex macroscopic patterns may emerge from simple local interaction rules at the microscopic scale. Such macroscopic structures are ubiquitous and observed, for instance, in numerous biological and physical systems. Examples include the coordinated motion of bird flocks, the formation of vortical structures in fish schools and bacterial colonies, or the spontaneous lane formation in pedestrian crowds. In each of these examples, individual agents – whether animals, cells, or humans – move based on local information of their surrounding environment, yet the resulting system exhibits global, self-organized behavior (Figure 1).

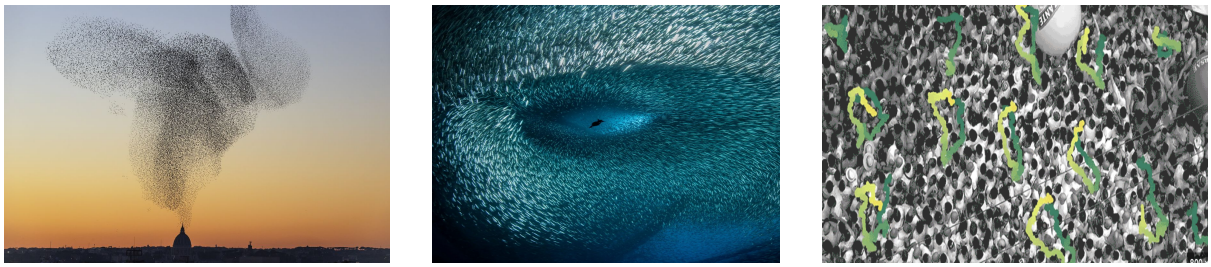

(a) **(b)** **(c)**

Figure 1: Various examples of self-organised collective behaviour. (a) A flock of starlings forming complex aerial patterns above Rome (pictured by *Søren Solkær*). **(b)** A school of fish exhibiting coordinated vortex-like motion (Source: Ocean Photographer of the Year 2022). **(c)** Spontaneous lane formation in a dense pedestrian crowd (taken from [65]).

To illustrate the difficulty of connecting microscopic dynamics to macroscopic ones and, more generally, of making **predictions** about the future states of such systems, we consider an example from classical mechanics. Let us consider the following "experiment", which consists of measuring the state of a point-like particle over time. In classical mechanics, the state of such a particle is fully characterized by its position and velocity vectors. According to Newton's second law, the evolution of this state is governed by the

equations

$$\frac{d\mathbf{p}}{dt} = \mathbf{F}(\mathbf{x}), \quad \frac{d\mathbf{x}}{dt} = \frac{\mathbf{p}}{m},$$

where $\mathbf{x}$ is the particle's position, $\mathbf{p}$ its momentum, m its mass, and $\mathbf{F}(\mathbf{x})$ the force field acting on it. This problem is fully deterministic, hence repeating this "experiment" with the same initial conditions will always produce the same result. However, in practice, even systems that appear "simple" can be analytically intractable. A classic example, as described in [98], is the three-body problem, *i.e.*, the motion of the Sun, Earth, and Moon (see Figure 2), which, despite its deterministic formulation, admits no general closed-form solution and requires numerical approximation. This simple example shows that indeed the Newtonian description could be applied only to a restricted class of phenomena. As the

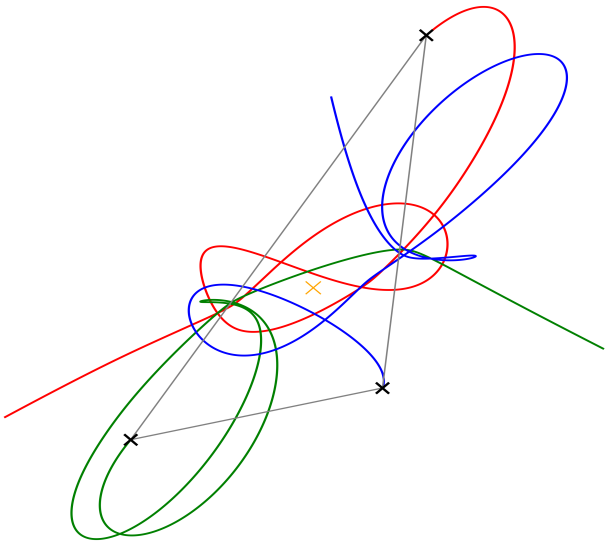

Figure 2: The three-body problem. Approximate trajectories of three identical bodies initially placed at the vertices of a scalene triangle and subject to mutual gravitational attraction. The coloured curves represent the paths of the bodies in the plane, while the grey lines connect their positions (black crosses). The centre of mass (orange cross) remains fixed, in accordance with the conservation of the momentum.

number of interacting agents increases and the interactions among them become complex, gaining knowledge of the system's state evolution is not only extremely difficult or not possible but also, in many cases, practically unnecessary for understanding its collective behavior. The need for a more tractable representation of many-particle systems guided the pioneering work of Maxwell, Boltzmann, and Gibbs, who introduced a statistical description of such systems in the late 19th century. In this probabilistic approach, rather than tracking individual particle trajectories, the system is described by a distribution

function that encodes the probability of finding particles in specific regions of the phase space, and the evolution of this distribution reflects the evolution in time of the **system's average behavior**. This probabilistic approach gave rise to kinetic theory and statistical mechanics and provided the fundamental tools for deriving macroscopic equations from microscopic ones.

This statistical framework is closely related to a wide range of real-world systems and, in this thesis, is mainly applied to the analysis of active particle systems, *i.e.,* models describing large populations of self-propelled agents that consume energy to generate motion or exert forces [11]. A fundamental trait of active systems is the presence of interaction mechanisms that cannot be merely attributed to mechanical forces and are commonly referred to as *social interactions*. By social interactions, we mean the ability of agents to adapt their behavior in response to information from their surrounding environment, such as the position, motion of nearby individuals, or their internal state. Typically, such interactions involve alignment, attraction-repulsion dynamics, or more complex decision-making processes that may depend on the configuration of the external environment, such as the chemotaxis in bacteria [30] or the consensus of opinions in social networks [116]. A fundamental difference between classical particle systems and active particle systems lies in the nature of their microscopic dynamics (see Figure 3). A classical example is provided by the Boltzmann equation, which models the statistical behavior of dilute gases undergoing binary, instantaneous, and elastic collisions [27]. During elastic collisions, mass, linear momentum, and kinetic energy are conserved, and the dynamics is time-reversible. In the context of the Boltzmann equation, this property is referred to as *microreversibility*. In contrast, active particle systems, such as those describing self-propelled agents with alignment interactions, are governed by interaction rules that typically violate these conservation laws. In alignment-based models, particles adjust their velocities according to the velocity of neighboring agents. These interactions are not elastic, and they generally do not conserve momentum or kinetic energy. Furthermore, the dynamics is intrinsically *irreversible*. The lack of conserved quantities breaks the standard analytical framework used for classical particle systems and necessitates the development of novel mathematical techniques.

1.1 Models of collective motion — Some examples

The complexity and richness of collective behavior observed in systems of many interacting agents have inspired the development of a broad class of mathematical models designed to capture their emergent dynamics, and motivated significant research activity within the mathematical community over the past few decades.

Individual-based models (IBMs) provide a natural framework for describing the dynam-

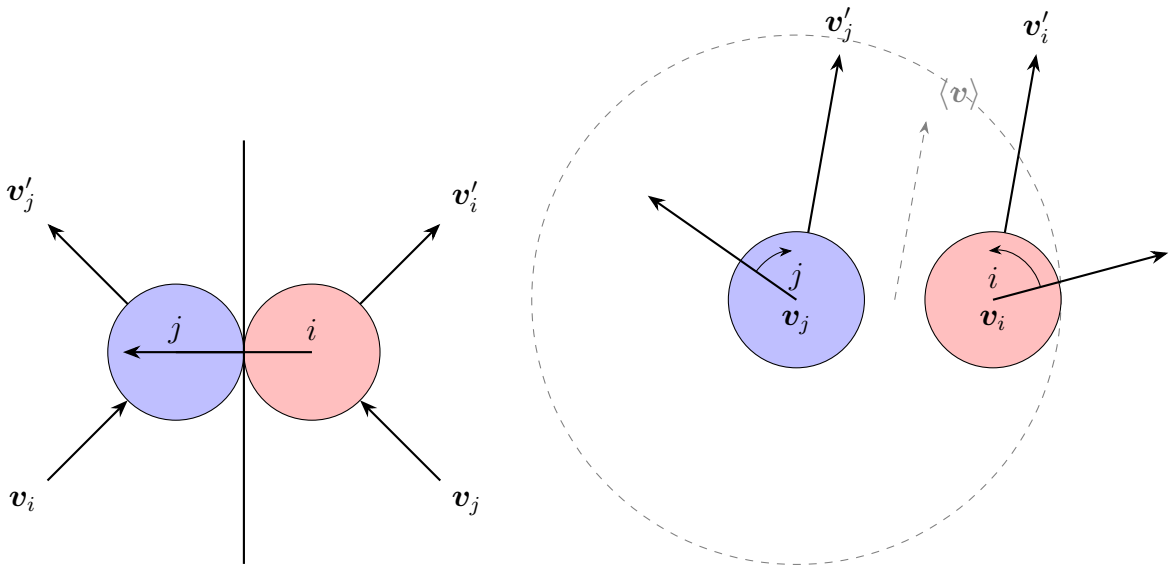

(a) Elastic collision (Boltzmann) **(b)** Alignment update (Vicsek model)

Figure 3: Comparison of microscopic interaction rules. **(a)** *Boltzmann hard-sphere collision*: particles interact via elastic collisions. Two particles i, j collide with velocities $\boldsymbol{v}_i$ and $\boldsymbol{v}_j$. After the collision, particles adopt velocities $\boldsymbol{v}'_i$ and $\boldsymbol{v}'_j$. During the collision mass, momentum, and kinetic energy are conserved, and the dynamics is time-reversible. **(b)** *Alignment-type interaction*: self-propelled agents with velocities $\boldsymbol{v}_i$ and $\boldsymbol{v}_j$ within a finite sensing radius (dashed) adjust their direction toward the local average velocity depicted as $\langle \boldsymbol{v} \rangle$. Momentum and energy are not conserved during the interaction, and the dynamics is irreversible.

ics of interacting particle systems. In such models, a system of N agents is described by a set of coupled ODEs, where the state of each agent $i = 1, \ldots, N$ is tracked individually over time. A typical example is when each agent is characterized by its position $x_i(t) \in \mathbb{R}^d$ and velocity $v_i(t) \in \mathbb{R}^d$ where $d \geq 1$ is the dimension of the space, which evolve according to

$$\begin{cases} \dfrac{dx_i}{dt} = v_i, \\ \dfrac{dv_i}{dt} = F_i(x_1, \ldots, x_N, v_1, \ldots, v_N), \end{cases}$$

where F_i denotes the sum of the forces acting on each agent i. Depending on the model, this force may encode effects such as alignment, attraction, repulsion, or stochastic noise. More generally, IBMs may include additional internal variables, such as orientation, phase, or chemical concentration, depending on the biological or physical system under consideration. Regardless of the specific formulation, IBMs provide a flexible microscopic framework for encoding interaction rules. Below, we present several representative and

widely studied models of collective dynamics.

- **The Vicsek model** [119], introduced in the 1990s, was initially formulated as a discrete-time algorithm in which particles move at a constant speed and at each time iteration update their velocity based on the average direction of neighboring agents within a fixed interaction radius. In its continuous-time reformulation, as proposed in [42] the model considers a system of N particles where each agent $i \in 1, \dots, N$ is described by its position $x_i(t) \in \mathbb{R}^d$ and velocity $v_i(t) \in \mathbb{S}^{d-1}$, constrained to lie on the unit sphere $\mathbb{S}^{d-1}$. The dynamics are given by the following system of ODEs:

$$\begin{cases} \dfrac{dx_i}{dt} = c\, v_k, \\ \dfrac{dv_i}{dt} = \nu\, (\mathrm{Id} - v_i \otimes v_i)\, \bar{v}_k, \end{cases}$$

  where $c > 0$ is the speed of each agent and $\nu \geq 0$ is a parameter controlling the strength of the alignment interaction. The operator $\mathrm{Id} - v_i \otimes v_i$ is the orthonormal projection operator onto v_i. Id is the identity matrix and $\otimes$ denotes the tensor product, defined as $(v \otimes u)_{i,j} = v_i u_j$, for any $v, u \in \mathbb{R}^d$. The operator $\mathrm{Id} - v_i \otimes v_i$ ensures that $|v_i|(t) = |v_i|(0) = 1$, so that $v_i \in \mathbb{S}^{d-1}$ for all times. Indeed one can check that $\frac{d}{dt}|v_i|^2 = 0$. Moreover, notice that $(\mathrm{Id} - v \otimes v)u = \nabla_v (u \cdot v)$, for any $v \in \mathbb{S}^{d-1}, u \in \mathbb{R}^d$, with ∇_v being the gradient on $\mathbb{S}^{d-1}$. Therefore, the dynamics for v_i corresponds to a gradient dynamics that maximize the potential $v_i \cdot \bar{v}_i$. Since the maximum is given by $v_i = \bar{v}_i$, the dynamics produce alignment. The term $\bar{v}_k \in \mathbb{S}^{d-1}$ denotes the normalized local average direction, computed from the vector $J_k(t) \in \mathbb{R}^d$ given by

$$J_k(t) = \frac{1}{N} \sum_{j=1}^{N} K(|X_j - X_k|) v_j(t),$$

  where $K : \mathbb{R}_+ \to \mathbb{R}_+$ is a symmetric interaction kernel, typically compactly supported. The quantity $\bar{v}_k = \frac{J_k}{|J_k|}$ (when $J_k \neq 0$) defines the target direction toward which agent k aligns.

  Despite its simplicity, the Vicsek model exhibits rich dynamical features, including phase transitions from disordered to globally aligned motion [4], [41], [97], and the emergence of high-density traveling bands [31]. These phenomena have been extensively studied through numerical simulations and theoretical analysis in several works; for a comprehensive review on these topics, we refer to [120].

- **The Cucker-Smale model** [35] is a microscopic model describing the emergence of *flocking* in a population of N interacting agents. Each agent $i = 1, \dots, N$ is described by its position $x_i(t) \in \mathbb{R}^d$ and velocity $v_i(t) \in \mathbb{R}^d$, evolving according to

the system:

$$\begin{cases} \dfrac{dx_i}{dt} = v_i, \\ \dfrac{dv_i}{dt} = \dfrac{1}{N}\displaystyle\sum_{j=1}^{N} \psi(|x_j - x_i|)(v_j - v_i), \end{cases}$$

where $\psi : [0, \infty) \to [0, \infty)$ is a *communication rate function* that quantifies the strength of interaction between agents as a decreasing function of their spatial distance r. A commonly used form is

$$\psi(r) = \frac{1}{(1 + r^2)^{\beta}}, \quad \beta \geq 0,$$

where the parameter β controls how rapidly the interaction decays with distance. By flocking, we refer to the emergence of two key collective behaviors. First, the velocities of all agents progressively align, so that, over time, each agent moves in the same direction and at the same speed. Second, as this alignment occurs, the group remains spatially cohesive: the relative distances between agents stay uniformly bounded, thereby preventing the population from dispersing [35].

An important result about the Cucker–Smale model is that if $\beta < 1/2$, then flocking emerges for any initial configuration of positions and velocities, regardless of how widely spread the agents are. In this case, the model is said to exhibit unconditional flocking. In contrast, when $\beta \geq 1/2$, flocking may still occur, but only under additional assumptions on the initial conditions, such as sufficient spatial concentration [35]. The Cucker–Smale model plays a central role in the mathematical analysis of consensus dynamics and has led to numerous extensions that address more realistic or complex scenarios, including:

- **Delayed interactions:** incorporating time-lags in the equation to introduce a fixed response time for the agents to process information from their surroundings and update their velocities accordingly [72].
- **Hierarchical interactions:** incorporating leadership in the communication rate function [110].
- **Topological models:** where each agent interacts with a fixed number of nearest neighbors, independent of distance [71].

- **The Kuramoto model** [1] is a fundamental microscopic model for studying synchronization phenomena in large populations of coupled oscillators. Each oscillator is characterized by a phase variable $\theta_i(t) \in \mathbb{S}^1$ and a natural frequency $\omega_i \in \mathbb{R}$, and its dynamics is governed by the ODE

$$\dot{\theta}_i = \omega_i + \frac{C}{N}\sum_{j=1}^{N} \sin(\theta_j - \theta_i),$$

where $C > 0$ is the coupling strength. The term $\sin(\theta_j - \theta_i)$ is a relaxation term that creates phase alignment among the oscillators. A central feature of the Kuramoto model is the emergence of synchronization, indeed when the coupling strength C exceeds a critical threshold, a subset of oscillators with sufficiently close frequencies begins to oscillate collectively with the same phase. This behavior is commonly referred as *phase locking* [67], where the phase differences between synchronized oscillators remain bounded over time. As the coupling strength increases, the size of the synchronized cluster grows, potentially leading to full phase locking in the population. One notable application of the Kuramoto model is in the study of neuronal synchronization; indeed, it has been observed that some areas of the brain exhibit synchronous activity, even in the absence of direct anatomical connections. The Kuramoto framework, particularly when $C = C_{i,j}(t)$ provides a tractable way to model this behavior by representing interacting neuronal populations as coupled phase oscillators [36].

All the previously described models can be extended to include Brownian motion, in order to account for non-deterministic effects.

1.1.1 PDMP formulation of binary instantaneous Collisions

Many of these models can be described as piecewise-deterministic Markov processes (PDMP) [47]. In the simplest setting we have:

- **Free flight:** between collisions, each particle is in *free flight* and it follows

$$\dot{x}_i(t) = v_i(t)\,, \qquad \dot{v}_i(t) = 0.$$

- **Poisson process:** each agent $i \in 1, \dots, N$ carries an independent Poisson process with constant rate $\lambda > 0$, producing jump times $(T_i^k)_{k\geq 1}$. The waiting time between successive jumps is exponentially distributed and has mean $1/\lambda$.

- **Velocity update at a jump:** at a jump time T_i^k, the velocity of particle i is instantaneously reset according to some distribution $\mathcal{D}$ (see Figure 4)

$$V_i^+ \;\sim\; \mathcal{D}((x_1^-, v_1^-, ..., x_N^-, v_N^-)),$$

  where $\mathcal{D}$ may depend on the whole configuration of the system and encodes the chosen collision rules (Boltzmann hard spheres, alignment collision, chemical reactions, *etc.*). Here, V_i^+ denotes the post-collision velocity of particle i, while x_i^- and v_i^- refer to the position and velocity of particle i immediately before the collision.

- **Start the process afresh.**

This PDMP viewpoint will turn out to be useful in Chapter 2, where we generalise this framework to *non-instantaneous collisions* whose finite stochastic duration can still be captured by suitably constructed Poisson processes.

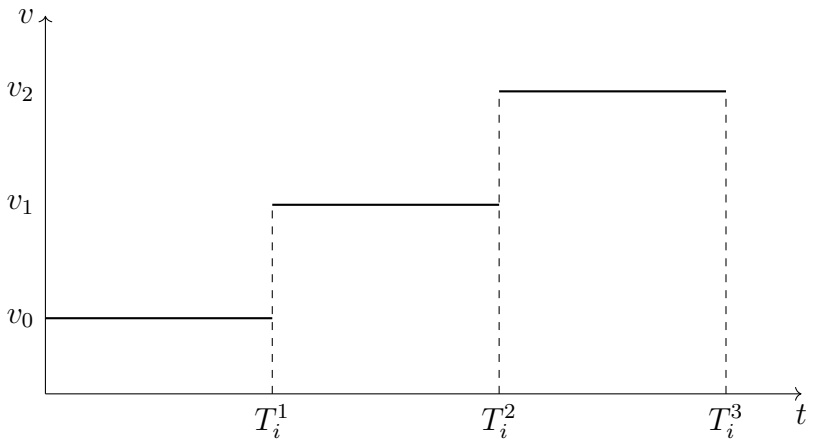

Figure 4: Velocity evolution as a jump process driven by collisions. Particles are in free flight and move at constant speeds v_0, v_1, v_2 (horizontal segments). Collisions occur at exponentially distributed times T_i^1, T_i^2, T_i^3; each collision produces an instantaneous jump in velocity from v_{k-1} to v_k.

1.2 The mean field description

As already observed in Section 1, when the number N of interacting particles becomes very large, tracking the full trajectory $(X_t^1, V_t^1, \dots, X_t^N, V_t^N)$ becomes extremely expensive (especially from a numerical point of view), since it evolves in a space of dimension $2Nd$. A more tractable description is obtained from a probability perspective. Instead of prescribing a deterministic initial configuration $(X_0^1, V_0^1, \dots, X_0^N, V_0^N) \in (\mathbb{R}^{2d})^N$, the system is initialized by a given distribution function $f_0^N \in (\mathbb{R}^{2d})^N$:

$$f_0^N = \mathcal{L}(X_0^1, V_0^1, \dots, X_0^N, V_0^N),$$

where $\mathcal{L}(Z)$ denotes the law of Z. Then, for each time $t \geq 0$, we denote

$$f_t^N := \mathcal{L}(X_t^1, V_t^1, \dots, X_t^N, V_t^N).$$

In the context of the mean-field limit, this law is always assumed to be *symmetric*, meaning it is invariant under any permutation of the particle indices. The evolution of f_t^N is then governed by the linear Kolmogorov (or Liouville) equation. The problem of working with f_t^N is that it is a probability measure on a space whose dimension grows with N.

To overcome this, let's consider a more natural object for studying symmetric particle systems: the *empirical measure*, defined as

$$\mu_t^N := \frac{1}{N}\sum_{i=1}^{N} \delta_{(X_t^i, V_t^i)}\,,$$

where $\delta_{(X_t^i,V_t^i)}$ is the Dirac delta measure centered in (X_t^i, V_t^i). The empirical measure is a random probability measure on $\mathbb{R}^{2d}$, and it is invariant under permutations of the particles. The key advantage of this representation is that all μ_t^N belong to the same infinite-dimensional space $\mathcal{P}(\mathbb{R}^{2d})$ of probability measures on $\mathbb{R}^{2d}$, regardless of N. Hence this makes it meaningful to ask whether μ_t^N converges, as $N \to \infty$. Moreover, the empirical measure provides a direct link between the microscopic particle description and the mean-field probabilistic framework. In particular, since the joint law is assumed to be symmetric, the expectation of the empirical measure coincides with the one-particle marginal law [114]:

$$\mathcal{L}(X_t^1, V_t^1) = \mathbb{E}\left(\mu_t^N\right).$$

Starting from an initial empirical measure μ_0^N that converges in some sense to a limiting probability measure μ_0, one asks whether, for each $t > 0$, μ_t^N converges (in some sense) to μ_t as $N \to \infty$, where $(\mu_t)_{t\geq 0}$ solves some differential equation. In the context of the mean-field models considered in Chapter 1, we will assume that, for each fixed time $t > 0$, the empirical measure μ_t^N converges weakly as $N \to \infty$ to a deterministic probability density $f_t = f(t, x, v)$. This limiting object describes the macroscopic distribution of particles in phase space and is governed by a nonlinear kinetic partial differential equation of the form

$$\partial_t f + v \cdot \nabla_x f = Q(f),$$

where the nonlinear operator $Q(f)$ is indicated as the *collisional operator* and captures the interaction dynamics of the underlying microscopic model. The previously stated convergence is known as the *propagation of chaos*. The idea is that if the particles are initially independent, i.e. $f_0^N = \mu_0^{\otimes N}$, then for every fixed $k \geq 1$ and each $t > 0$ the k-particle marginal $f_t^{N,(k)}$ converges weakly to the product measure $f_t^{\otimes k}$ as $N \to \infty$. While the molecular chaos assumption was introduced by Maxwell [87] and Boltzmann [18], a rigorous probabilistic formulation was first given by Kac [79] and later extended by McKean [88] and Sznitman [114]; see also [28], [29] for a comprehensive review on the topic. The kinetic formulation of active particle systems is an intermediate asymptotic description necessary for deriving the macroscopic (or hydrodynamic) equations presented in the next section. We note here, though, that the limit to derive the Boltzmann equation is not a mean-field limit [60], [45].

1.3 The macroscopic description

Macroscopic (or hydrodynamic) equations provide a continuum description of large systems of interacting agents by capturing the evolution of a set of macroscopic observables, typically the mass density and the mean velocity (or orientation). These equations are formally derived from the kinetic description by performing an appropriate asymptotic analysis carried out through rescaling some of the quantities of the system. This asymptotic analysis is necessary to obtain close equations for the macroscopic quantities. In particular, in Chapter 1, for a variant of the Vicsek model we adopt the hyperbolic scaling, such that space and time are rescaled simultaneously according to

$$\tilde{t} = \frac{\varepsilon t}{t_0}, \qquad \tilde{x} = \frac{\varepsilon x}{x_0},$$

where $x \in \mathbb{R}^d$, $t \in \mathbb{R}_+$ denote the microscopic space and time variables, x_0, t_0 are characteristic microscopic length and time scales, and $\varepsilon \ll 1$ is a dimensionless parameter measuring the ratio between microscopic and macroscopic scales. The corresponding macroscopic variables are denoted by $(\tilde{x}, \tilde{t})$, and the dimensionless speed is given by $\tilde{c}_0 = \frac{c_0 t_0}{x_0}$. The function f^ε satisfies the rescaled kinetic equation

$$\varepsilon\Big(\partial_t f^\varepsilon + c_0 v \cdot \nabla_x f^\varepsilon\Big) = Q(f^\varepsilon)\,.$$

The formal hydrodynamic limit corresponds to the regime $\varepsilon \to 0$, in which the collisional dynamics dominate over the transport. In this limit, the distribution f^ε is expected to converge to a local equilibrium, characterized as an element of the kernel of the collision operator Q and depending on the macroscopic quantities of the system.

In classical kinetic theory, macroscopic closure relies on the existence of *collisional invariants*, *i.e.*, quantities conserved through the collision dynamics. However, as discussed in Section 1, momentum or energy are generally not conserved in active particle models. As a result, the set of standard collisional invariants is insufficient to close the macroscopic system. To address this difficulty, in Chapter 1 we employ the concept of *Generalized Collisional Invariants* (GCI), introduced by Degond and Motsch [42], which extends the classical notion of collisional invariant to systems with alignment dynamics, such as the Vicsek model.

2 Chapter summaries

2.1 A third-order model for collective dynamics

Chapter 1 investigates an IBM combining features from both the Vicsek and Kuramoto models. Each agent is described by its position $\mathbf{x}_i \in \mathbb{R}^2$, its orientation angle θ_i, and

its angular velocity ω_i. The motion occurs at constant speed $c > 0$ along the direction $\vec{\tau}(\theta) = (\cos\theta_i, \sin\theta_i)$, while the angular velocity relaxes toward the mean angular velocity of neighbors. In parallel, we introduce a distinct alignment mechanism that acts directly on the orientation angle. The orientation alignment is reminiscent of phase synchronization in the Kuramoto model, except that here the interaction occurs only locally in space, as in the Vicsek model. The resulting dynamics defines a third-order system that captures alignment in both the orientation and the angular velocity, each influenced by independent stochastic noise:

$$\frac{d\mathbf{x}_i}{dt} = c\,\vec{\tau}(\theta_i), \tag{1}$$

$$d\theta_i = \omega_i\,dt + k_\theta \sin(\overline{\theta}_i - \theta_i)\,dt + a\,dB_t^i, \tag{2}$$

$$d\omega_i = k_\omega(\overline{\omega}_i - \omega_i)dt + b\,d\tilde{B}_t^i, \tag{3}$$

where B_t^i and $\tilde{B}_t^i$ are standard Brownian motions, independent for each agent $i \neq j$. Here, $\overline{\theta}_i$ denotes the average orientation angle of agents in a neighborhood of agent i, and $\overline{\omega}_i$ is the corresponding local average angular velocity. The constants $k_\theta > 0$ and $k_\omega > 0$ control the strength of the alignment in orientation and angular velocity, respectively, while $a, b > 0$ represent the noise intensity in the orientation and angular velocity dynamics.

The model is motivated by experimental observations in dense suspensions of self-propelled particles, such as sperm vortices [106], gliding biofilaments [113], and swimming fish [61], that exhibit underdamped turning dynamics not captured by classical second-order alignment models. A similar approach has been first considered in the Persistent Turning Walker with Alignment model (PTWA) [43], which incorporates the curvature of each particle as a dynamical variable that relaxes toward a specific target curvature. The latter is determined by the misalignment between the agent's direction of motion and the average direction of its neighbors. In contrast, our model introduces an additional alignment mechanism that acts directly on the orientation angle, leading to simultaneous alignment of both orientation and angular velocity under independent stochastic noise.

Starting from this individual-based dynamics, and following the formalism presented in Section 1.2, we derive a non-linear kinetic equation of Fokker–Planck type for the one-particle distribution function, defined over the phase space of position, orientation, and angular velocity. The hydrodynamic description is then obtained in the asymptotic regime where alignment interactions dominate the transport, using the Generalized Collision Invariant (GCI) method [42]. This leads to a closed Euler-type system for the agent

density ρ, mean orientation Ω, and average angular velocity $\overline{\omega}$ of the form:

$$\partial_t \rho + c_1 \nabla_x \cdot (\rho\, \Omega) = 0\,, \tag{4}$$

$$\partial_t (\rho\, \overline{\omega}) + c_1 \nabla_x \cdot (\rho\, \overline{\omega}\, \Omega) = 0\,, \tag{5}$$

$$\rho \left(\partial_t \Omega + c_2 (\Omega \cdot \nabla_x)\Omega - \overline{\omega}\, \Omega^{\perp} \right) + \frac{1}{\kappa} P_{\Omega^{\perp}} \nabla_x \rho = 0\,, \tag{6}$$

where $P_{\Omega^{\perp}} = \mathrm{Id} - \Omega \otimes \Omega$ is the projection onto the orthogonal direction $\Omega^{\perp} = (-\sin\overline{\theta}, \cos\overline{\theta})$, with Id denoting the 2×2 identity matrix, $\kappa = \frac{k_\theta}{\alpha^2}$, and the constants c_1, c_2 arise from the closure procedure. A key difference between the macroscopic system (4)–(6) and those obtained from the classical Vicsek model lies in the presence of the term $-\bar{\omega}\Omega^{\perp}$ which encodes the influence of angular velocity on the evolution of the mean orientation of the system.

In contrast to previous works such as [40], our particle model allows the angular velocity to evolve dynamically, resulting in a third-order stochastic differential equation (SDE) system. In [40] instead, the angular velocity is assumed constant, hence the dynamics remain of the second-order. Despite this key difference at the microscopic level, the macroscopic equations derived in [40], in one specific asymptotic regime, resemble the system obtained in (4)-(6). Although [40] develops a related theoretical framework, it does not provide numerical results, neither at the microscopic nor the macroscopic scale.

In addition to the analytical derivation of the macroscopic system, Chapter 1 aims to asses the accuracy of the macroscopic model through numerical simulations. The goal is to qualitatively compare its behavior with that of the individual-based model (IBM), particularly in a high-density regime consistent with the mean-field scaling. Numerical experiments on the IBM exhibit a variety of emergent collective phenomena, such as rotating clusters, traveling orientation waves, and synchronized oscillatory states. These patterns are then compared with the solutions of the macroscopic system.

The main difficulty in the numerical approximation of the system (4)–(6) lies in the fact that the equation of the mean orientation Ω is not written in conservative form. As a result, standard tools for hyperbolic conservation laws are not directly applicable. To overcome this, we adopt the relaxation approach introduced for the Self-Organized Hydrodynamics (SOH) model in [91]. Following this methodology, one can show that the macroscopic system (1.26)–(1.28) arises as the relaxation limit of a conservative system with a source term.

At the current stage of our analysis, we observe that the macroscopic model, while successfully capturing some large-scale qualitative features seen in the microscopic simulations, fails to reproduce certain patterns that emerge in the IBM, such as the traveling wave observed in the orientation variable.

2.2 Non-instantaneous and non-binary collisions

Classical kinetic theory, as for example the Boltzmann equation, is built on the assumption that collisions are instantaneous, meaning that the effect of a collision drives an immediate change in particle velocities. As a consequence, the resulting collision dynamics can be described by a pure jump process in velocity space, as detailed in Section 1.1.1. However, empirical observations across a range of biological and physical systems suggest that interaction dynamics are rarely instantaneous. A representative example is the run-and-tumble dynamics of E. coli bacteria, where the common modeling assumption of an instantaneous tumble phase [21] may not be accurate, given that its actual duration constitutes approximately 10% of the typical run phase [12]. Similarly, in processes such as contact inhibition of locomotion (a phenomenon observed in cell migration where cells repolarize and change direction upon contact) the interaction involves mechanical contact and consequent reorganization of the cytoskeleton, a process that unfolds over a non-negligible timescale [37]. Comparable temporal delays also arise in social systems, where interactions involve the exchange of information or decision-making processes that are intrinsically non-instantaneous. This is evident in models of opinion formation [52] and more generally in collective dynamics involving social interactions (see Section 1.1).

Altogether, these considerations motivate the attempt to revise the classical assumption of instantaneous collisions in kinetic theory. Notably, [80] introduces, for the first time, a framework that models non-instantaneous interactions through two independent Poisson processes (in contrast to the classical representation as a single one). In analogy with the PDMP setting of Section 1.1.1, each particle $i = 1, \dots, N$ is equipped with two independent Poisson processes:

- **Collision process:** each particle is equipped with a Poisson process of rate $\lambda > 0$, generating a sequence $(T^k_{i,\text{in}})_{k\geq 1}$, which determine the moments at which particle i enters a collision.
- **Exit from the collision process:** each particle is equipped with a second Poisson process of rate $\gamma > 0$, generating a sequence $(T^k_{i,\text{out}})_{k\geq 1}$, which determine when the particle i leaves the collision state.

This framework provides a minimal stochastic model for collisions with finite, random durations. Unlike classical PDMPs, where the velocity changes instantaneously, here the particle velocity evolves continuously during the collision process, following a prescribed collision dynamics. For example, in [80], particles undergo continuous alignment of their states (e.g., velocity or opinion) throughout the collision period, as illustrated in Figure 5. The first objective of Chapter 2 is to extend the stochastic finite-duration collision framework introduced in [80] to account for *non-binary* interactions. In classical

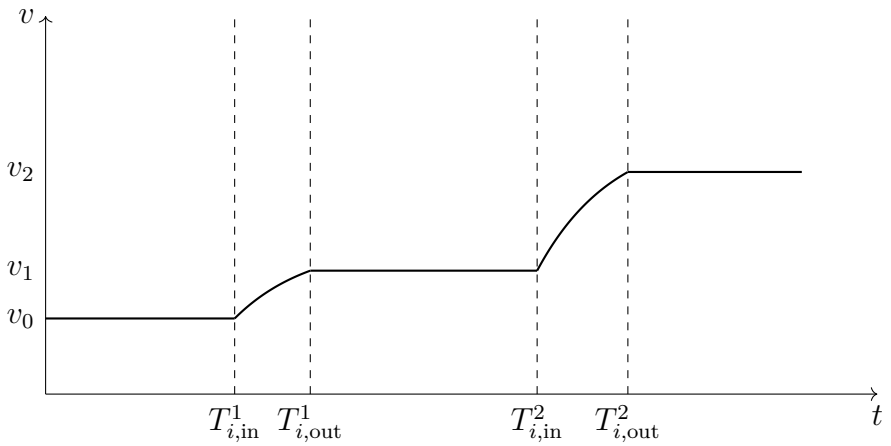

Figure 5: Velocity evolution with stochastic finite-duration collisions. Horizontal segments represent free flight phase. During each collision interval $\left[T^k_{i,\text{in}}, T^k_{i,\text{out}}\right]$ the velocity relaxes toward a target value prescribed by the alignment dynamics of the model. Because the exit time $T^k_{i,\text{out}}$ is random, the interaction may end before full alignment is achieved.

kinetic theory, the assumption of instantaneous collisions justifies restricting the model to binary interactions. Indeed, in the Boltzmann–Grad limit, the probability that a collision involves more than two particles becomes negligible [27]. However, this idealization breaks down in the setting of extended interaction duration, indeed, while a pair of agents is engaged in a collision, additional particles may enter and join the interaction before it ends.

To capture the emergence of multi-particle interactions, we formulate a model in which the collision processes can involve $k \geq 2$ particles. The system is described by a hierarchy of k-particle symmetric distribution functions $(f_k)_{k\geq 1}$, where f_1 represents the distribution of particles in free flight, and f_k for $k \geq 2$ characterizes the distribution of k-agent clusters engaged in a collision process. The symmetry condition expresses the indistinguishability property, *i.e.,* f_k is invariant under permutations of its arguments. Each group of size $k \in \mathbb{N}$ is represented by a k-tuple $(v_1, \ldots, v_k) \in \mathbb{R}^k$, encoding the individual states of its members (e.g., velocities, opinions, etc.). The resulting structure naturally gives rise to a kinetic equation of coagulation–fragmentation type, in which the entrance into the collision state corresponds to coagulation (cluster aggregation), and the exit corresponds to fragmentation (cluster splitting). For example, when a single agent joins a collision group of size k, a new group of size $k + 1$ is formed. Conversely, the termination of a collision may lead to the partial fragmentation into smaller subgroups. The evolution of

the system is hence governed by the following coagulation–fragmentation model

$$\begin{aligned}\partial_t f_k + \nabla_{(v_1,\dots,v_k)} \cdot (U_k f_k) = \frac{1}{2}\sum_{j=1}^{k-1} \lambda_{j,k-j} f_j \odot f_{k-j} - \sum_{j\geq 1} \lambda_{j,k} f_k \int_{\mathbb{R}^j} f_j^*\, d(v_1^*,\dots,v_j^*) \\ + \sum_{j\geq 1} \mu_{k,j} \int_{\mathbb{R}^j} f_{k+j}\, d(v_{k+1},\dots,v_{k+j}) - \frac{1}{2}\sum_{j=1}^{k-1} \mu_{j,k-j} f_k,\end{aligned} \tag{7}$$

for all $k \geq 1$, where f_j^* denotes evaluation at $(v_1^*,\dots,v_j^*)$. The symmetric tensor product is defined by

$$(f_j \odot f_{k-j})(v_1,\dots,v_k) := \binom{k}{j}^{-1} \sum_{c\in C(k,j)} f_j(v_c)\, f_{k-j}(v_{c'}),$$

where $C(k,j)$ denotes the set of j-combinations of $\{1,\dots,k\}$, and c' is the complement of c. The model is parametrised by the following interaction rates:

- $\lambda_{i,j} = \lambda_{j,i} \geq 0$: the rate of coagulation between groups of sizes i and j, corresponding to the entrance in a joint interaction;
- $\mu_{i,j} = \mu_{j,i} \geq 0$: the rate of fragmentation of a group of size $i+j$ into subgroups of sizes i and j, corresponding to the end of a collision.

The fields $U_k \in \mathbb{R}^k, k \geq 1$ describe the evolution dynamics of a group of size k. In the context of alignment-type dynamics, this is modelled by relaxation towards the mean state:

$$(U_k)_i := \frac{1}{k}\sum_{j=1}^{k} v_j - v_i, \quad i = 1,\dots,k, \qquad k > 1. \tag{8}$$

In Chapter 2 we establish key formal properties of the derived model (7). First, the total number of individuals M, defined as $M = \sum_{k\geq 1} kM_k$, where M_k denotes the number of clusters of size k, is conserved by the dynamics. The same holds for the total first-order moment I, defined as $I = \sum_{k\geq 1} I_k$, where $I_k = \frac{1}{k}\int \sum_{j=1}^{k} v_j f_k(v_1,\dots,v_k)\, dv_1 \cdots dv_k$. As a result, the average state of the system, given by $v_\infty = I/M$, remains constant in time. Moreover, a heuristic argument shows that if $\{M_k(t)\}_{k\geq 1}$ converges to a detailed-balance equilibrium $\{M_k^\infty\}_{k\geq 1}$, then the average state within each group, defined by $v_k := I_k/M_k$, converges to v_∞ as $t \to \infty$. Finally, we show that the state of each individual also approaches v_∞, and this is supported by the decrease of the total variance of the system over time.

The second aim of Chapter 2 is to derive a first-order corrections to the instantaneous limit problem by considering the following regime of fast collisions

$$\mu_{i,j} \mapsto \varepsilon^{-1}\mu_{i,j}, \quad U_k \mapsto \varepsilon^{-1}U_k, \quad f_k \mapsto \varepsilon^{k-1} f_k\,.$$

This scaling yields a system of two equations, one for the distribution of particles in free flight and a second one for the distribution of particle pairs undergoing binary collisions and the resulting formulation also includes terms that account for the effect of three-particle collisions. We prove existence and uniqueness of mild solutions to this system, as well as a rigorous justification of the instantaneous limit as $\varepsilon \to 0$.

In addition, we seek an approximate model of comparable accuracy that reduces to a scalar equation for the one-particle distribution. In [80], it is shown that the dynamics of non-instantaneous binary collisions can be reformulated as a scalar equation involving time delays. Using a Taylor expansion in the delay parameter, as done for instance in [50], [82], would lead to an equation of the form

$$\partial_t f_1 = \mathcal{Q}_2(f_1, f_1) + \varepsilon\, \mathcal{Q}_3(f_1, f_1, f_1),$$

where the operator $\mathcal{Q}_2$ encodes the binary collision process, and $\mathcal{Q}_3$ contains contributions from three-particle interactions. However, such approximations done through Taylor expansion may fail to preserve the nonnegativity of the solution. To address this, at the end of Chapter 2 we propose an alternative delay-based scalar model that is both accurate to first order and preserves the nonnegativity of the solution.

2.3 Stationary solutions for a Coagulation–Transport–Nucleation equation

In contrast to the previous section, which introduced a coagulation–fragmentation model for finite-duration and non-binary interactions, Chapter 3 considers a more classical setting: particles are characterized solely by their size $x \in \mathbb{R}$, and coagulation is assumed to be instantaneous and binary (see Figure 6). In this framework, the outcome of an interaction is the immediate merging of two clusters into a single one whose size equals the sum of the sizes of the interacting clusters.

The model we study in Chapter 3 builds on the framework introduced in [44], which describes the formation of protein aggregates in the context of *selective autophagy*. Autophagy is a fundamental quality-control mechanism in cells, where damaged components, such as misfolded proteins or dysfunctional organelles, are enclosed within membrane vesicles (autophagosomes) and delivered to lysosomes for degradation and recycling. In selective autophagy, specific cargos are marked for removal via molecular tags recognized by specific adaptor proteins. One adaptor is the p62, which not only binds ubiquitinated proteins (those tagged for degradation) but also promotes their clustering into larger aggregates, improving their recognition by the autophagy machinery. In [44], aggregates are described by their internal molecular composition, specifically the numbers of p62 units and ubiquitin molecules in various binding states.

In Chapter 3, we adopt a different viewpoint compared to [44], in which aggregates are described solely by their size, without tracking their internal molecular composition. This approach simplifies the model and allows us to focus on the evolution of the aggregate size distribution over time, driven by three key mechanisms:

- **Binary coagulation**, as in the classical Smoluchowski model [122], in which two clusters merge instantaneously to form a larger one. The coagulation is governed by the symmetric coagulation kernel $K(x, y)$, which specifies the rate at which two clusters of sizes x and y coalesce.
- **Size transport**, since aggregates may grow or shrink continuously due to the attachment or detachment of monomers.
- **Nucleation**, corresponding to a continuous influx of monomers (*i.e.,* particles of size zero) in the system.

The model does not include fragmentation, in line with experimental observations that p62–ubiquitin aggregates are structurally stable and do not exhibit splitting or internal rearrangement [126].

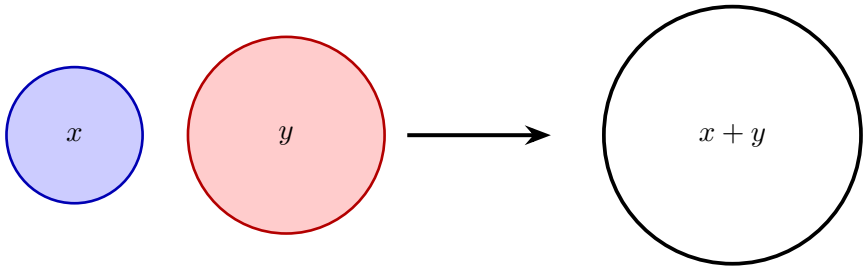

Figure 6: Coagulation dynamics. Binary coagulation of particles x and y forming a particle of size $x + y$. The coagulation rate is given by the coagulation kernel $K(x, y)$.

These mechanisms give rise to a nonlinear integro-differential equation that describes the time evolution of the cluster size distribution, given by the system

$$\begin{cases} \frac{\partial}{\partial t} f(x,t) + \frac{\partial}{\partial x}\Big(v(x) f(x,t)\Big) = \ \mathcal{C}(f)(t,x), \\ f(0,t) = f_0\,, \end{cases} \tag{9}$$

where $f(x, t)$ denotes the density of aggregates of size $x \in \mathbb{R}_+$ at time t, $v(x)$ models the rate at which a cluster of size x grows or shrinks and $\mathcal{C}(f)$ is the classical Smoluchowski coagulation operator:

$$\mathcal{C}(f)(x) = \frac{1}{2}\int_0^x K(y, x-y) f(y) f(x-y)\, dy - f(x) \int_0^\infty K(x, y) f(y)\, dy\,.$$

Finally, the nucleation is encoded via the boundary condition $f(0,t) = f_0$, prescribing a constant influx of monomers within the system.

Coagulation equations have been extensively studied in both physical and biological contexts, for example, in aerosol dynamics [49], [56], [108] and in modeling polymerization processes in biological systems [127]. More generally, coagulation–fragmentation equations have been the focus of substantial analytical and numerical investigation; see [10], [9] for comprehensive reviews. In contrast, coagulation equations considering a transport term in the size variable, such as (9), have received relatively less interest. The main objective of Chapter 3 is to study the existence of non-trivial stationary solutions to (9), particularly in the case of the multiplicative kernel $K(x,y) = xy$.

When both coagulation and fragmentation are present, the dynamics are reversible, in the sense that each coagulation event can, in principle, be counteracted by a corresponding fragmentation event. One can therefore intuitively expect the existence of non-trivial steady states. This intuition can be formalized, as explained for instance in [10], by examining the stationary coagulation–fragmentation (C-F) equation. In particular, a steady-state solution $f(x)$ to the C-F equation must satisfy the following *detailed balance condition*:

$$K(x,y)f(x)f(y) = F(x,y)f(x+y), \quad \text{for all } x,y > 0,$$

where $K(x,y)$ is the coagulation kernel and $F(x,y)$ is the binary fragmentation rate at which a cluster of size $x+y$ breaks into two fragments of size x and y respectively. In contrast, models that involve only coagulation or only fragmentation are fundamentally irreversible. It is therefore natural to expect that such systems do not admit non-trivial steady states: in pure coagulation, mass is irreversibly transferred toward larger cluster sizes; in pure fragmentation, mass is continually broken into smaller and smaller pieces. However, in certain cases, particularly for specific classes of coagulation and multiple-fragmentation kernels, exact stationary solutions have been constructed—for example, in [51].

More recently, the existence of stationary non-equilibrium solutions has been established in [54] for coagulation equations, both in the discrete and continuous settings, with a source term modeling the continuous injection of small particles within the system. This setting shares structural similarities with our model, where the boundary condition at zero encodes the persistent nucleation of monomeric units.

Coagulation–transport models with strictly positive velocity were first studied in [59], where global existence in L^2 has been obtained in the case

$$0 \le K(x,y) \le C_0 \left(1 + (x\,y)^{-\beta_0}\right), \quad (x,y) \in (0,\infty)^2,$$

for some constants $\beta_0 \ge 0$ and $C_0 > 0$. This work was later extended in [58], where the regularity assumptions on the kernel is relaxed, and a source term is incorporated in the

model. The analysis in both papers is based on semigroup theory in the L^2-framework. However, these results do not address more general, physically relevant spaces such as weighted L^1. Moreover, they do not cover coagulation kernels that become unbounded for large cluster sizes.

A significant advance in the treatment of more general models is provided by [63], where the authors establish global well-posedness for coagulation–transport equations in L^1, for kernels that are singular at small sizes and grow at most linearly at infinity. This extends the theory to a much broader class of biologically and physically motivated models.

In Chapter 3, the interplay between coagulation and transport in equation (9), induces a nontrivial balance, indeed while coagulation transports mass toward larger cluster sizes, the drift term may counteract this flux by slowing down growth or inducing shrinkage of large clusters. The central analytical question we want to address is the identification of conditions under which a stationary profile can exist and be sustained, despite the mass transfer toward large sizes driven by coagulation and the continuous input of monomers via nucleation. In the absence of fragmentation, coagulation alone drives mass toward large sizes, and unless this growth is counteracted, the system exhibits finite-time *gelation*, that is, a fraction of the mass is lost because it "escapes to infinity". We show that indeed this occurs when the transport velocity is strictly positive, in particular for $v(x) = 1$.

In contrast, we show that a sign-changing transport velocity is necessary to counteract the growth of large aggregates. Moreover, the velocity must not only change sign, but also decay sufficiently fast at infinity to balance the effects of coagulation and nucleation. Under these conditions, we prove the existence of stationary profiles using the Schauder fixed point theorem. We also present formal asymptotic analysis of the solutions and provide preliminary numerical results supporting the analytical findings.

2.4 Modeling protein transport between the Endoplasmic Reticulum and the Nuclear Envelope

Chapter 4 is motivated by the experimental observation of fast protein transport between two intracellular compartments: the endoplasmic reticulum (ER) and the nuclear envelope (NE). These compartments are connected via ER–NE junctions, which are sparse and extremely narrow (occurring at a density of approximately 0.1 junctions per square micrometer and measuring less than 20 nanometers in diameter). Given their rarity and small cross-section (see Figure 7), it is not *a priori* clear whether passive diffusion alone could explain the experimentally observed transport rates.

To qualitatively describe this phenomena, we model the dynamics as purely passive diffusion between the ER and NE through narrow connecting junctions. Since the geometry

of the ER and NE is complex and their volumes are much larger than that of the junctions, we treat them as well-mixed compartments with homogeneous protein concentrations. We moreover assume that all junctions are identical and share the geometry of a truncated cone. However, because the precise geometry of the junction—particularly its length—is not well resolved in the experimental data, we argue that its length is much larger than its cross-sectional radius. Under this assumption, asymptotic analysis allows us to reduce the three-dimensional diffusion equation to an effective one-dimensional model describing protein diffusion along the length of the junction.

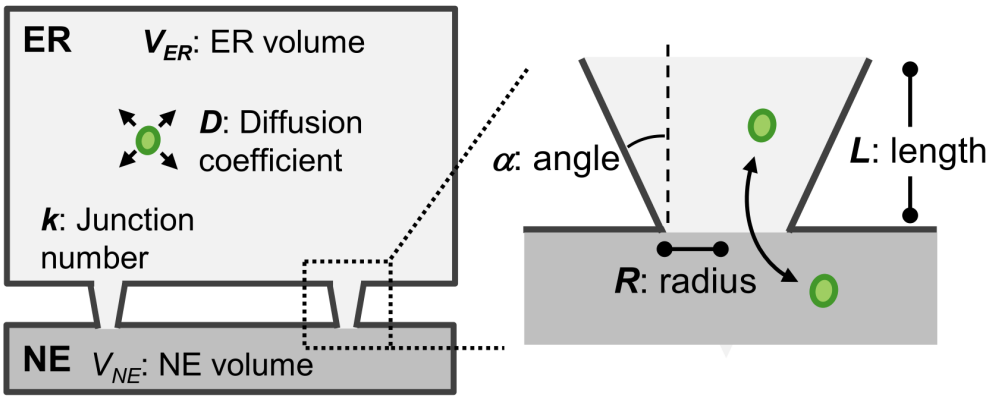

Figure 7: Schematic of the model domain. Proteins diffuse passively from the endoplasmic reticulum (ER) to the nuclear envelope (NE) through narrow junctions. The model parameters include the ER and NE volumes V_{ER} and V_{NE}, the diffusion coefficient D, the number of junctions k, the junction length L, and its base radius R. The angle α characterizes the conical geometry of the junctions. The image has been provided by the group of Shotaro Otsuka (Max Perutz Laboratories).

For this one dimensional problem, the dimensional analysis reveals the presence of three well-separated time scales in the system, corresponding to the relative sizes of the involved compartments. Diffusion within the narrow junctions occurs on a fast time scale due to their small volume and short length. In contrast, diffusion in the NE takes place on an intermediate time scale, reflecting its moderate size relative to the ER. Finally, changes in the ER concentration occur on the slowest time scale, owing to its comparatively large volume. This time scale separation enables further simplification: since the dynamics within the junction equilibrate rapidly, they can be approximated as quasi-stationary, and the ER concentration can be treated as constant on the time scale relevant to NE dynamics.

Since the experimental data track the protein concentration within the NE, we focus on the intermediate time scale associated with NE dynamics. On this time scale, the

model reduces to the equation

$$\frac{d\rho_{\mathrm{NE}}}{dt}(t) = \kappa\left(\rho_{\mathrm{ER},0} - \rho_{\mathrm{NE}}(t)\right), \qquad \text{with} \quad \kappa = \frac{kDA^*}{V_{\mathrm{NE}}L},$$

where ρ_{NE} denotes the protein concentration in the NE, κ is the trasnport rate constant, D is the diffusivity of the cargos, $\rho_{\mathrm{ER},0}$ is the (assumed constant) ER concentration, V_{NE} is the volume of the NE, L is the junction length, and A^* is the average cross-sectional area of the junctions. Solving the this equation yields

$$\rho_{\mathrm{NE}}(t) = \rho_{\mathrm{ER},0}\left(1 - e^{-\kappa t}\right),$$

which describes the exponential recovery of the NE concentration toward equilibrium. This approximation proves sufficient to recover the correct order of magnitude for the experimentally observed transport rate, suggesting that passive diffusion alone—when combined with the structural properties of the ER–NE junctions—may be enough to account for the surprisingly fast protein transport. Furthermore, at the end of Chapter 4, we discuss potential sources of variability in the estimated transport rates; for instance, how the shape of the transported cargos may influence the obtained results.

Chapter 1

Collective dynamics with alignment and angular velocity synchronisation: macroscopic equations and pattern formation

Joint work with S. Merino-Aceituno

In this work, we investigate an individual-based model (IBM) for self-propelled agents interacting locally on a plane. Agents are characterized by their position, the angle determining their direction of motion, and their angular velocity. The dynamics combine features of the well-known Vicsek and Kuramoto models, which describe collective dynamics and synchronization, respectively. The evolution of the directions of motion follows a Vicsek model, where agents align their orientations with the mean orientation of their neighbors, subject to some noise. Similarly, the angular velocities relax towards the average angular velocity of the neighboring agents, also subject to noise.

We derive the corresponding kinetic equation in the limit of a large number of agents and formally obtain the macroscopic equations through a macroscopic (hydrodynamic) limit. Numerical simulations of the IBM reveal a variety of patterns, including rotating clusters, traveling orientation waves, and globally synchronized rotational motion. A preliminary qualitative comparison with simulations of the macroscopic system show the ability of the macroscopic model to reproduce some emergent behavior of the IBM.

Contents

1 Introduction 24

2 Individual-Based model, mean-field limit and scaling 27

2.1 The IBM 27

2.2 Mean–field equations 28

2.3 Scaling of the kinetic model (1.10) 29
3 Macroscopic limit 31
3.1 Generalized collisional invariant 33
3.2 Proof of theorem 3.1 35
3.3 Periodic solutions 39
4 Simulation of the microscopic model 39
4.1 Numerical integration of the particle system 40
4.2 Patterns: phase diagrams 40
5 Simulation of the macroscopic model 43
5.1 Comparison between microscopic and macroscopic simulations 46
5.2 Conclusions 47

1 Introduction

This work investigates an individual-based model (IBM) describing the collective behavior of self-propelled agents subject to multiple local alignment mechanisms. We propose a model related to the Persistent Turning Walker with Alignment (PTWA) model [43], namely, we consider a third-order particle model in which the acceleration evolves dynamically in response to interactions. In the PTWA model, each agent moves at a constant speed and updates its orientation according to the curvature of its trajectory, which relaxes toward a target curvature. The latter is computed from the misalignment between the agent's direction of motion and the mean direction of its neighbors within a fixed interaction radius. This framework, as observed for example in [93], captures key aspects of the persistent trajectories and curvature-based coordination characteristic of schooling fish. Indeed, under-damped dynamics, where the effective force acts on a particle's curvature rather than directly on its direction of motion, have been shown to better capture the smooth directional changes characteristic of chemically propelled rods [100], [115], steadily swimming fish [61], and biofilaments gliding in high motor density motility assays [113].

In our model, particles are characterized by their positions x_i, their direction of motion θ_i, and their angular velocity ω_i. Each particle moves at constant speed in the direction given by $(\cos\theta_i, \sin\theta_i)$, and its acceleration influences the evolution of its orientation; namely, the orientation evolves under the influence of an intrinsic angular velocity ω_i, which itself relaxes toward the average angular velocity of neighboring particles. In addition, we introduce a distinct local alignment mechanism acting directly on each agent's orientation angle. The inclusion of alignment interactions in the model is motivated by numerous

studies in the physics literature showing that such terms are essential for capturing large-scale collective dynamics, including rotational behaviors such as vortex formation in dense suspensions of self-propelled agents [113]. Similar self-organized vortex structures have been observed in other biological systems, such as suspensions of sperm cells, which form stable vortex arrays [106]. While this term reflects phase synchronization in the spirit of the Kuramoto model [1], the alignment occurs only between spatially neighboring agents, as in the Vicsek model [119]. As a result, the dynamics feature simultaneous alignment in the angular velocity and the orientation angle, each influenced by independent stochastic noise.

Both the Vicsek and Kuramoto models have played a fundamental role in the modeling of collective behavior, particularly in biological systems. The Vicsek model, initially proposed as a minimal framework for flocking, describes self-propelled particles aligning their orientation to that of nearby neighbors under the influence of noise. Despite its simplicity, the model exhibits rich emergent dynamics, including phase transition between disordered and ordered motion [4], [31], [41], [97], [119], traveling density bands [62] and milling states [84]. In some cases, alignment interactions can emerge from more fundamental physical interactions, such as steric repulsion or volume exclusion, particularly in systems of elongated self-propelled particles [102], [89]; for a comprehensive review on these topics, we refer to [120]. Within this class of models describing swarming agents, the transition to a large number of interacting individuals justifies a mean-field approximation, where the system is described by a kinetic equation governing the time evolution of a probability density function in phase space [17], [68]. A further level of coarse-graining yields hydrodynamic equations for macroscopic observables such as local density and momentum [69]. Specifically, in the context of the Vicsek alignment model, the first hydrodynamic description was proposed by Degond and Motsch, resulting in the Self-Organized Hydrodynamics (SOH) equations [42], which was later made rigorous in [78].

The first aim of the present work is to derive a mean-field description of the previously described individual-based model. In the limit of a large number of interacting particles, this leads to a kinetic equation of Fokker–Planck type for the one-particle distribution function, defined over position, orientation, and angular velocity space. Next, we seek a macroscopic description of the dynamics via a hydrodynamic limit. A common feature of active particle systems, such as the Vicsek model, is that momentum and kinetic energy are generally not conserved. This is due to self-propulsion and to the fact that energy is typically dissipated as particles align with their neighbors. As a result, the system lacks a sufficient number of standard conserved quantities, or collisional invariants, to close the macroscopic equations. To overcome this difficulty, we use the framework of Generalized Collisional Invariants [42], which allows us to derive a closed macroscopic

system describing the agent density, mean orientation, and average angular velocity. The resulting equations form an Euler-type system, consisting of two conservative equations for the mass and the angular momentum, coupled with an evolution equation for the mean orientation. The latter includes a term accounting for the system's rotation under the geometric constraint enforcing unit norm of the orientation vector.

Beyond the analytical derivation, a further objective of this work is to assess the validity of the macroscopic model through numerical simulations and to qualitatively compare its behavior with that of the individual-based model (IBM) in a high-density regime consistent with the mean-field scaling. Simulations of the IBM exhibit various collective behaviors, including rotating clusters, traveling orientation waves, and synchronized oscillatory states. We then proceed to compare these solutions to those of the macroscopic system. At this point of our analysis, we observe that the macroscopic model fails to reproduce certain structures that emerge in the IBM. While it successfully captures some large-scale qualitative features, it cannot account for the full range of patterns present in the microscopic dynamics. This mismatch suggests that, due to the averaging nature of macroscopic models, fine-scale structures and stochastic effects may be smooth out in the hydrodynamic limit. This also happens in other individual based models, where phenomena like bistability, or symmetry breaking, clearly visible in the IBM, may be absent in the corresponding hydrodynamic description [25].

A related approach to the present work is presented in [40], where agents are assigned a constant angular velocity, leading to persistent circular trajectories. In contrast, our model introduces third-order dynamics, where the angular velocity evolves in time and is influenced by interactions with neighboring agents. Although [40] develops a related theoretical framework, it does not provide numerical results, neither at the microscopic nor the macroscopic scale. Finally, another similarity can be observed with the swarmalator model introduced in [39], where each particle moves at a constant self-propulsion speed and carries an internal phase, evolving under a combination of interaction mechanisms: alignment of the propulsion direction toward local averages, synchronization of internal phases, attraction-repulsion forces, and external confinement. Notably, the microscopic simulations presented in [39] exhibit traveling wave patterns in the phase variable that qualitatively resemble those emerging in our model under suitable parameter regimes. Although the two models exhibit similar behaviors, their underlying dynamics differ fundamentally. The swarmalator model features non-symmetric interactions, with each agent's phase directly influencing its spatial motion. In contrast, our model is based on symmetric interactions, where angular velocity affects motion only indirectly, through its influence on orientation.

The paper is organized as follows. In Section 2, we introduce the individual-based model, derive its mean-field kinetic description, and present the hydrodynamic scaling.

Section 3 states the main theorem of the paper and details the derivation of the macroscopic equations using the Generalized Collision Invariant (GCI) method. Section 4 presents numerical simulations of the IBM, highlighting the emergence of various collective behaviors. Section 5 introduces the macroscopic simulations and provide a qualitative comparison with those of the IBM. Finally, Appendix A contains supplementary videos illustrating representative microscopic and macroscopic simulation results discussed in Sections 4 and 5.

2 Individual-Based model, mean-field limit and scaling

2.1 The IBM

We consider a system of N interacting agents moving in the two-dimensional plane $\mathbb{R}^2$ at constant speed $c > 0$. The state of the i-th agent at time t is described by its position $\mathbf{x}_i(t) \in \mathbb{R}^2$, orientation angle $\theta_i(t) \in (-\pi, \pi]$ and angular velocity $\omega_i(t) \in \mathbb{R}$. The unit vector $\vec{\tau}(\theta_i) = (\cos\theta_i, \sin\theta_i)$ gives the direction of motion. The following system of coupled stochastic differential equations governs the dynamics of the system

$$\frac{d\mathbf{x}_i}{dt} = c\,\vec{\tau}(\theta_i), \tag{1.1}$$

$$d\theta_i = \omega_i\,dt + k_\theta \sin(\overline{\theta}_i - \theta_i)\,dt + a\,dB_t^i, \tag{1.2}$$

$$d\omega_i = k_\omega(\overline{\omega}_i - \omega_i)dt + b\,d\tilde{B}_t^i, \tag{1.3}$$

where $B_t^i, \tilde{B}_t^i$ are standard Brownian motions, independent between themselves and those of each agent $i \neq j$. The positive constants a and b quantify the intensity of the random perturbation acting on the orientation angle and the angular velocity, respectively. In this model, agents are subject to two alignment mechanisms. The first induces a relaxation of the orientation angle θ_i of each agent towards the average orientation of its neighbors $\bar{\theta}_i$, with a relaxation frequency $k_\theta > 0$. The second prescribes a relaxation of the angular velocity ω_i of each agent towards the local average angular velocity $\bar{\omega}_i$, with relaxation frequency $k_\omega > 0$. In the absence of these interaction forces and the Brownian motions, each particle is subjected to its intrinsic angular velocity ω_i, which results in a circular trajectory of radius $r_i = \frac{c}{|\omega_i|}$, rotating counter-clockwise if $\omega_i > 0$ and clockwise if $\omega_i < 0$. The average direction $\bar{\theta}_i$ is defined as the orientation corresponding to the normalized local average of the velocity directions of surrounding agents, where the influence of each neighbor is modulated by a radially symmetric interaction kernel $K = K(|x|)$, i.e.

$$\vec{\tau}(\overline{\theta}_i) = \overline{\Omega}_i\,, \qquad \overline{\Omega}_i = \frac{J_i}{|J_i|}\,, \qquad J_i = \frac{1}{N}\sum_{j=1}^{N} K\Big(|x_i - x_j|\Big)\,\vec{\tau}(\theta_j). \tag{1.4}$$

Similarly, $\bar{\omega}_i$ denotes the local average angular velocity among neighboring agents

$$\bar{\omega}_i = \frac{1}{\mathcal{N}_i} \sum_{j=1}^{N} K\left(|x_i - x_j|\right) \omega_j \,, \qquad \mathcal{N}_i = \sum_{j=1}^{N} K\left(|x_i - x_j|\right), \tag{1.5}$$

where $\mathcal{N}_i$ indicates the number of neighboring particles weighted by the kernel K. Moreover we impose that

$$\int K dx = 1.$$

We observe that the interaction term for ω_i is divided by $\mathcal{N}_i$. This normalization ensures that the interaction force remains of order one, regardless of the total number of particles. In contrast, such normalization is not required in the orientation interaction term, as the vector Ω_i is of order one by construction.

As a preliminary step toward deriving the macroscopic model, we introduce a non-dimensional form of the system (1.1)–(1.3). We choose a fixed time scale t_0 and the associated space scale $x_0 = c\, t_0$, which represents the typical distance traveled by a particle over that timescale. The characteristic angular velocity scale is set to $\omega_0 = t_0^{-1}$. Moreover, $\overline{\theta}_i$ remains unchanged since it represents a direction on the unit circle, while $\overline{\omega}_i$ rescales as $\tilde{\overline{\omega}}_i = \frac{\overline{\omega}_i}{\omega_0}$, consistently with the scaling of ω_i. With these choices, we introduce the following dimensionless variables $\tilde{x} := \frac{x}{x_0}$, $\tilde{t} := \frac{t}{t_0}$ and $\tilde{\omega} := \frac{\omega}{\omega_0}$ and the rescaled interaction kernel $\tilde{K}$, defined by $K(x_0|\tilde{x}|) = \tilde{K}(|\tilde{x}|)$. In particular, if K is the indicator function of a ball of radius R, then $\tilde{K}$ corresponds to the indicator function of a ball of radius $\tilde{R} = R/x_0$. The noise intensities are now encoded in the dimensionless parameter $\alpha^2 = \frac{a^2 t_0}{2}$ and $\beta^2 = \frac{b^2 t_0}{2}$, while the rescaled interaction forces are given by

$$\tilde{k}_\theta = k_\theta t_0 \,, \qquad \tilde{k}_\omega = k_\omega t_0 \,.$$

This leads to the following dimensionless system (dropping the tildes for simplicity):

$$dx_i = \vec{\tau}(\theta_i)\, dt \,, \tag{1.6}$$

$$d\theta_i = \omega_i\, dt + k_\theta \sin(\overline{\theta}_i - \theta_i)\, dt + \sqrt{2\alpha^2} dB_t^i \,, \tag{1.7}$$

$$d\omega_i = k_\omega(\overline{\omega}_i - \omega_i)\, dt + \sqrt{2\beta^2}\, d\tilde{B}_t^i \,. \tag{1.8}$$

2.2 Mean–field equations

The first step in our analysis consists in deriving the mean-field equation corresponding to the agent-based dynamics (1.6)–(1.8). As is standard in the mean-field analysis of interacting particle systems (see, e.g., [111]), we study the empirical distribution associated with the particle system,

$$f^N(t, x, \theta, \omega) = \frac{1}{N} \sum_{i=1}^{N} \delta_{(x_i(t), \theta_i(t), \omega_i(t))}(x, \theta, \omega) \,. \tag{1.9}$$

Formal arguments indicate that in the limit for $N \to \infty$ the empirical distribution converges weakly to the distribution function f that satisfies the following Fokker-Planck equation

$$\partial_t f + \vec{\tau}(\theta) \cdot \nabla_x f + \partial_\theta(\omega f) = -k_\theta \, \partial_\theta(f F_f^K) - k_\omega \, \partial_\omega(f G_f^K) + \alpha^2 \partial_\theta^2 f + \beta^2 \partial_\omega^2 f \,, \quad (1.10)$$

with

$$\begin{aligned} F_f^K &= \sin(\overline{\theta}_f - \theta) \,, \quad \vec{\tau}(\overline{\theta}_f)(t,x) = \overline{\Omega}_f^K \,, \quad \overline{\Omega}_f^K = \frac{J_f^K(x)}{|J_f^K(x)|} \,, \\ J_f^K &= \int_{\mathbb{R}^2 \times (-\pi,\pi] \times \mathbb{R}} K_R\Big(|x-y|\Big) \vec{\tau}(\theta) f(t,y,\theta,\omega) dy \, d\theta \, d\omega \,, \end{aligned} \quad (1.11)$$

$$\begin{aligned} G_f^K &= \overline{\omega}_f - \omega \,, \quad \overline{\omega}_f(t,x) = \frac{1}{\rho_f^K(x)} \int_{\mathbb{R}^2 \times (-\pi,\pi] \times \mathbb{R}} K_R\Big(|x-y|\Big) \omega \, f(t,y,\theta,\omega) dy \, d\theta \, d\omega \,, \\ \rho_f^K(x) &= \int_{\mathbb{R}^2 \times (-\pi,\pi] \times \mathbb{R}} K_R\Big(|x-y|\Big) \, f(t,y,\theta,\omega) dy \, d\theta \, d\omega \,, \end{aligned} \quad (1.12)$$

where K_R is the scaled interaction kernel

$$K_R(x) := \frac{1}{R^2} K\left(\frac{x}{R}\right) \,,$$

so that

$$\int_{\mathbb{R}^2} K_R(x) \, dx = 1.$$

We have finally introduced the parameter $R > 0$, which represents the typical interaction radius.

The proof of the mean–field limit can be made rigorous since all terms are Lipschitz, following classical coupling arguments (see for example [17], [114], [23]). Finally, by the fact that the empirical measure (1.9) is a probability measure, f satisfies the normalization condition

$$\int_{\mathbb{R}^2 \times (-\pi,\pi] \times \mathbb{R}} f(x,\theta,\omega,t) dx \, d\theta \, d\omega = 1. \quad (1.13)$$

2.3 Scaling of the kinetic model (1.10)

We now make the following scaling assumptions, for a scaling parameter $\varepsilon \ll 1$:

$$R = \varepsilon \,, \quad k_\theta = \mathcal{O}\left(\frac{1}{\varepsilon}\right), \quad k_\omega = \mathcal{O}\left(\frac{1}{\varepsilon}\right), \quad \beta^2 = \mathcal{O}\left(\frac{1}{\varepsilon}\right), \quad \alpha^2 = \mathcal{O}\left(\frac{1}{\varepsilon}\right). \quad (1.14)$$

This scaling reflects a regime in which interaction forces and stochastic fluctuations dominate the dynamics. Thus, introducing k'_θ, k'_ω, β', and α' such that $k_\theta = k'_\theta/\varepsilon$, $k_\omega = k'_\omega/\varepsilon$, $\beta^2 = (\beta')^2/\varepsilon$, and $\alpha^2 = (\alpha')^2/\varepsilon$, we may assume that k'_θ, k'_θ, β' and α' are constants. After this scaling, equation (1.10) is written as (dropping the primes for simplicity):

$$\partial_t f^\varepsilon + \vec{\tau}(\theta) \cdot \nabla_x f^\varepsilon + \partial_\theta(\omega f^\varepsilon) = \frac{1}{\varepsilon} Q(f^\varepsilon) \,, \quad (1.15)$$

where

$$Q(f^\varepsilon) = k_\theta\,\partial_\theta(F^K_{f^\varepsilon}\,f^\varepsilon) + \alpha^2\partial^2_\theta f^\varepsilon + k_\omega\,\partial_\omega(G^K_{f^\varepsilon}\,f^\varepsilon) + \beta^2\partial^2_\omega\,f^\varepsilon\,, \tag{1.16}$$

and

$$\begin{aligned} F^K_{f^\varepsilon} &= \sin(\theta - \overline{\theta}_{f^\varepsilon})\,, \quad \vec{\tau}(\overline{\theta}_{f^\varepsilon})(t,x) = \Omega^K_{f^\varepsilon}\,, \quad \Omega^K_{f^\varepsilon} = \frac{J^K_{f^\varepsilon}(x)}{|J^K_{f^\varepsilon}(x)|}\,, \\ J^K_{f^\varepsilon} &= \int_{\mathbb{R}^2\times(-\pi,\pi]\times\mathbb{R}} K_\varepsilon\Big(|x-y|\Big)\,\vec{\tau}(\theta)\,f^\varepsilon(t,y,\theta,\omega)\,dy\,d\theta\,d\omega\,, \end{aligned} \tag{1.17}$$

$$\begin{aligned} G^K_f = (\omega - \overline{\omega}_{f^\varepsilon})\,, \quad \overline{\omega}_{f^\varepsilon}(t,x) = \frac{1}{\rho^K_f(x)}\int_{\mathbb{R}^2\times(-\pi,\pi]\times\mathbb{R}} K_\varepsilon\Big(|x-y|\Big)\omega\,f^\varepsilon(t,y,\theta,\omega)dy\,d\theta\,d\omega\,, \\ \rho^K_f(x) = \int_{\mathbb{R}^2\times(-\pi,\pi]\times\mathbb{R}} K_\varepsilon\Big(|x-y|\Big)\,f^\varepsilon(t,y,\theta,\omega)dy\,d\theta\,d\omega \end{aligned} \tag{1.18}$$

We now state the following lemma, which characterizes the localization of the interaction terms in space.

Lemma 2.1 (Expansion for localized interactions)**.** *The following expansions hold:*

$$\begin{aligned} F^K_f &= F_f + \mathcal{O}(\varepsilon^2), \\ G^K_f &= G_f + \mathcal{O}(\varepsilon^2), \end{aligned}$$

where the leading-order terms are given by

$$\begin{aligned} F_f = \sin(\overline{\theta}_f - \theta)\,, \quad \vec{\tau}(\overline{\theta}_f)(t,x) = \Omega_f(t,x), \quad \Omega_f = \frac{J_f(x)}{|J_f(x)|}\,, \\ J_f(x) = \int_{(-\pi,\pi]\times\mathbb{R}} \vec{\tau}(\theta)\,f(t,x,\theta,\omega)\,d\theta\,d\omega\,, \end{aligned}$$

$$G_f = \overline{\omega}_f - \omega, \quad \overline{\omega}_f(t,x) = \frac{1}{\rho_f(x)}\int_{(-\pi,\pi]\times\mathbb{R}} \omega\,f(t,x,\theta,v)\,d\theta\,d\omega\,, \quad \rho_f(x) = \int_{(-\pi,\pi]\times\mathbb{R}} f(t,y,\theta,\omega)\,d\theta\,d\omega\,.$$

Proof. We remind that the scaled interaction kernel is defined as

$$K_\varepsilon(x) := \frac{1}{\varepsilon^2}K\left(\frac{x}{\varepsilon}\right)\,,$$

hence we can rewrite the nonlocal alignment term as

$$\begin{aligned} J_f(t,x) &= \int_{\mathbb{R}^2\times(-\pi,\pi]\times\mathbb{R}} \frac{1}{\varepsilon^2}K\left(\frac{x-y}{\varepsilon}\right)\vec{\tau}(\theta)\,f(t,y,\theta,\omega)\,dy\,d\theta\,d\omega \\ &= \int_{\mathbb{R}^2\times(-\pi,\pi]\times\mathbb{R}} K(z)\,\vec{\tau}(\theta)\,f(t,x-\varepsilon z,\theta,\omega)\,dz\,d\theta\,d\omega\,, \end{aligned} \tag{1.19}$$

where in the last equality we have used the change of variable $y = x - \varepsilon z$, so $dy = \varepsilon^2 dz$. Assuming that f is smooth enough in the spatial variable, we perform a Taylor expansion at x:

$$f(t,x-\varepsilon z,\theta,\omega) = f(t,x,\theta,\omega) - \varepsilon z\cdot\nabla_x f(t,x,\theta,\omega) + \frac{}{2}z^T\nabla^2_x f(t,x,\theta,\omega)z + \mathcal{O}(\varepsilon^3)\,, \tag{1.20}$$

and we substitute it in the previous expressions, where z^T denotes the transpose of z. Finally, using the fact that K is even, i.e.

$$\int_{\mathbb{R}^2} z\, K\left(\frac{z}{r'}\right) dz = 0,$$

we find the leading-order approximation

$$J_f(t,x) = \int_{(-\pi,\pi]\times\mathbb{R}} \vec{\tau}(\theta)\, f(t,x,\theta,\omega)\, d\theta\, d\omega + \mathcal{O}(\varepsilon^2). \tag{1.21}$$

A similar argument applies to the term averaging the angular velocity ω, concluding the proof. □

The previous hydrodynamic scaling leads to the following kinetic problem, which depends on the scaling parameter ε:

$$\partial_t f^\varepsilon + \vec{\tau}(\theta)\cdot\nabla_x f^\varepsilon + \partial_\theta(\omega\, f^\varepsilon) = \frac{1}{\varepsilon} Q(f^\varepsilon) + \mathcal{O}(\varepsilon^2)\,, \tag{1.22}$$

where

$$Q(f) = k_\theta\, \partial_\theta(f\, F_f) + k_\omega\, \partial_\omega(f\, G_f) + \alpha^2 \partial_\theta^2 f + \beta^2 \partial_\omega^2 f\,, \tag{1.23}$$

with F_f and G_f given by Lemma 2.1. The hydrodynamic model is obtained as the $\varepsilon \to 0$ limit of this system.

3 Macroscopic limit

In this section, we state the main theoretical result of our analysis, namely the derivation of the macroscopic system obtained as the formal limit for $\varepsilon \to 0$ of equation (1.22). To this end, we begin by introducing the following distributions:

$$\begin{aligned} \mathcal{M}_{\overline{w}_f}(\omega) &= C_1 \exp\left(-\frac{k_\omega}{2\beta^2}(\omega-\overline{\omega}_f)^2\right), \qquad C_1 = \sqrt{k_\omega/2\pi\beta^2}\,, \\ \mathcal{N}_{\overline{\theta}_f}(\theta) &= C_2 \exp\left(\frac{k_\theta}{\alpha^2}\cos(\theta-\overline{\theta}_f)\right), \qquad C_2 = \frac{1}{2\pi I_0\left(k_\theta/\alpha^2\right)}\,, \end{aligned} \tag{1.24}$$

where $\mathcal{M}_{\overline{w}_f}$ corresponds to a Gaussian distribution centered at $\overline{\omega}_f$ and with variance β^2/k_ω. $\mathcal{N}_{\overline{\theta}_f}(\theta)$ is the von Mises distribution on the interval $(-\pi,\pi]$ centered at $\overline{\theta}_f$ and with variance $1-\frac{I_1(k_\theta/\alpha^2)}{I_0(k_\theta/\alpha^2)}$, where $I_j(\cdot)$ denotes the modified Bessel function of order j. We now proceed to the statement of the main theorem.

Theorem 3.1. *Suppose that there is a smooth solution f^ε to the kinetic model (1.22) for all $\varepsilon > 0$ and that this solution converges as $\varepsilon \to 0$ to some function f^0. Then*

$$f^\varepsilon \xrightarrow[\varepsilon\to 0]{} f^0 = \rho(x,t)\, \mathcal{N}_{\overline{\theta}}(\theta)\, \mathcal{M}_{\overline{w}}(\omega)\,, \tag{1.25}$$

where $\mathcal{N}$ and $\mathcal{M}$ are respectively the von Mises distribution and the Gaussian defined in (1.24)*. The density $\rho = \rho(x,t)$, the direction of the flux $\Omega = \Omega(x,t) = (\cos\bar{\theta}, \sin\bar{\theta})$ and the mean angular velocity $\bar{\omega} = \bar{\omega}(x,t)$ satisfy the following macroscopic system:*

$$\partial_t \rho + c_1 \nabla_x \cdot (\rho\, \Omega) = 0\,, \tag{1.26}$$

$$\partial_t (\rho\, \overline{\omega}) + c_1 \nabla_x \cdot (\rho\, \overline{\omega}\, \Omega) = 0\,, \tag{1.27}$$

$$\rho \left(\partial_t \Omega + c_2 (\Omega \cdot \nabla_x)\Omega - \overline{\omega}\, \Omega^{\perp} \right) + \frac{1}{\kappa} P_{\Omega^{\perp}} \nabla_x \rho = 0\,, \tag{1.28}$$

where $P_{\Omega^{\perp}} = \mathrm{Id} - \Omega \otimes \Omega$ is the projection onto the orthogonal direction $\Omega^{\perp} = (-\sin\overline{\theta}, \cos\overline{\theta})$, with Id *denoting the 2×2 identity matrix. The constant c_1 is defined as*

$$c_1 = \frac{I_1(\kappa)}{I_0(\kappa)}\,, \tag{1.29}$$

where $\kappa = \frac{k_\theta}{\alpha^2}$, and $c_2 = K_2/K_1$ with the constants K_1 and K_2 that are explicitly defined in section 3.2 by (1.52) *and* (1.55) *respectively.*

The macroscopic system (1.26)–(1.28) shares structural similarities with those derived in previous works on alignment-based models such as [42], [43]. In particular, it has the same form as the macroscopic system obtained in [40] in the regime of small angular velocity (SOHR-S model), despite being derived from a different microscopic dynamics. System (1.26)–(1.27) consists of two conservative equations, respectively for the mass density ρ and the angular momentum density $\rho\,\bar{\omega}$. In particular as observed in [40], the equation for $\rho\,\bar{\omega}$ can be rewritten (for smooth solutions) as a transport equation for the average rotation velocity $\bar{\omega}$ using equation (1.26):

$$\partial_t \bar{\omega} + c_1 \Omega \cdot \nabla_x \bar{\omega} = 0, \tag{1.30}$$

which simply expresses that the average rotation velocity $\bar{\omega}$ is convected at speed c_1 along the direction Ω. The equation (1.28) governs the evolution of the average direction of motion Ω, subject to the geometrical constraint $|\Omega| = 1$. This constraint is dynamically preserved by the presence of the projection matrix $P_{\Omega^{\perp}} = \mathrm{Id} - \Omega \otimes \Omega$. Indeed by taking the scalar product of the equation with Ω, we obtain $\partial_t |\Omega|^2 + c_2(\Omega \cdot \nabla_x)|\Omega|^2 = 0$, which shows that the norm $|\Omega|$ remains constant along the flow. Owing to the geometrical constraint $|\Omega| = 1$, the equation for Ω cannot be written in conservative form, as the dynamics evolve on the unit circle. This intrinsic non-conservative structure reflects the absence of momentum conservation in the underlying microscopic model. Finally, a key feature of this equation is the presence of the term $-\overline{\omega}\,\Omega^{\perp}$, which describes the turning of the collective direction field in proportion to the average angular velocity $\overline{\omega}$, encoding the influence of individual self-rotation at the macroscopic scale.

Formula (1.25) relies on the following Lemma, whose proof can be adapted from [42].

Lemma 3.2. *(i) Q can be written as*

$$Q(f^\varepsilon) = I_\theta(f^\varepsilon) + I_\omega(f^\varepsilon)\,, \tag{1.31}$$

where

$$I_\omega(f) = \beta^2\partial_\omega\Big[\mathcal{M}_{\overline{\omega}_f}\partial_\omega\Big(\frac{f}{\mathcal{M}_{\overline{\omega}_f}}\Big)\Big]\,, \qquad I_\theta(f) = \alpha^2\partial_\theta\Big[\mathcal{N}_{\overline{\theta}_f}\partial_\theta\Big(\frac{f}{\mathcal{N}_{\overline{\theta}_f}}\Big)\Big]\,. \tag{1.32}$$

(ii) Define the dissipation functional:

$$\mathcal{D}(f) := \int_{(-\pi,\pi]\times\mathbb{R}} Q(f)\,\frac{f}{\mathcal{N}_{\overline{\theta}_f}(\theta)\mathcal{M}_{\overline{w}_f}}\,d\theta\,d\omega. \tag{1.33}$$

Then we have:

$$\mathcal{D}(f) = -\int_{(-\pi,\pi]\times\mathbb{R}} \mathcal{N}_{\overline{\theta}_f}(\theta)\mathcal{M}_{\overline{w}_f}\left[\alpha^2\left|\partial_\theta\left(\frac{f}{\mathcal{N}_{\overline{\theta}_f}(\theta)\mathcal{M}_{\overline{w}_f}}\right)\right|^2 + \beta^2\left|\partial_\omega\left(\frac{f}{\mathcal{N}_{\overline{\theta}_f}(\theta)\mathcal{M}_{\overline{w}_f}}\right)\right|^2\right] d\theta\,d\omega \le 0. \tag{1.34}$$

(iii) The equilibria of Q (i.e., the functions $f = f(\theta,\omega) \ge 0$ such that $Q(f) = 0$) form a three-dimensional manifold $\mathcal{E}$ given by:

$$\mathcal{E} = \Big\{\rho\,\mathcal{N}_{\bar\theta}(\theta)\,\mathcal{M}_{\bar\omega}(\omega)\;\Big|\;\rho\in\mathbb{R}_+,\,\bar\theta\in(-\pi,\pi],\,\bar\omega\in\mathbb{R}\Big\}\,,$$

where ρ is the total mass, $\bar\theta$ is the mean orientation (i.e., the direction of the flux), and $\bar\omega_f$ is the mean angular velocity of $\rho\,\mathcal{N}_{\bar\theta}\,\mathcal{M}_{\bar\omega}$.

3.1 Generalized collisional invariant

To derive the hydrodynamic limit of f^ε, we must identify the collisional invariants of the operator Q, i.e., functions ψ such that

$$\int Q(f)\,\psi\,d\theta\,d\omega = 0, \quad \text{for all } f. \tag{1.35}$$

It is straightforward to verify that $\psi = 1$ is a collisional invariant, as it reflects the conservation of total mass. In our setting, the function $\psi = \omega$ is also a collisional invariant, corresponding to the conservation of total angular momentum. Beyond these, however, the collision operator admits no other standard invariants. Yet, since the equilibrium manifold of Q is three-dimensional, we need an additional conserved quantity to derive a closed macroscopic system. To overcome this difficulty, we use the notion of *Generalized Collisional Invariant (GCI)* introduced in [42]. The key idea is to relax condition (1.35).

Definition 3.3. *We define $\mathcal{I}(f;\bar\theta)$ for a given $\bar\theta\in(-\pi,\pi]$ by:*

$$\mathcal{I}(f;\bar\theta) = \partial_\theta\left(k_\theta\sin(\theta-\bar\theta)f + \alpha^2\partial_\theta f\right).$$

Definition 3.4 (Generalized Collisional Invariant)**.** *Let $\bar{\theta} \in (-\pi, \pi]$ be fixed and define $\Omega = (\cos\bar{\theta}, \sin\bar{\theta})$. We say that a function $\chi_{\bar{\theta}} : (-\pi, \pi] \to \mathbb{R}$ is a* Generalized Collisional Invariant (GCI) *associated to I_θ at orientation Ω, if and only if:*

$$\int_{(-\pi,\pi]} \mathcal{I}(f;\bar{\theta})\,\chi_{\bar{\theta}}(\theta)\,d\theta = 0 \quad \forall f \text{ such that } \quad \int_{(-\pi,\pi]} f(x,t,\theta,\omega)\,\sin(\theta-\bar{\theta})\,d\theta = 0. \tag{1.36}$$

The GCI will be useful since

$$\int I_\theta(f)\chi_{\bar{\theta}}\,d\theta = 0\,,$$

but $I_\theta(f) = \mathcal{I}(f;\bar{\theta}_f)$. This implies that

$$\int I_\theta(f^\varepsilon)\chi_{\bar{\theta}_{f^\varepsilon}} d\theta = 0 \qquad \forall \varepsilon > 0. \tag{1.37}$$

We indeed observe that condition (1.36) is equivalent to have

$$\int_{(-\pi,\pi]} \frac{f}{\mathcal{N}_{\bar{\theta}}} \partial_\theta\Big(\mathcal{N}_{\bar{\theta}}\partial_\theta\chi_{\bar{\theta}}\Big)d\theta = 0, \quad \forall f \text{ such that } \quad P_{\Omega^\perp}\Omega_f = 0\,,$$

which, as showed in [42], can be also be written as

$$\int_{(-\pi,\pi]} f(x,t,\theta,\omega)\,\Omega^\perp \cdot \vec{\tau}(\theta)d\theta = 0\,, \tag{1.38}$$

or, equivalently, to

$$\int_{(-\pi,\pi]} f\,\sin(\theta-\bar{\theta})\,d\theta = 0. \tag{1.39}$$

In [42] it is shown that (1.36) is equivalent to the fact that there exists $\beta \in \mathbb{R}$ such that

$$\int_{(-\pi,\pi]} \frac{f}{\mathcal{N}_{\bar{\theta}}}\left[\partial_\theta\Big(\mathcal{N}_{\bar{\theta}}\partial_\theta\chi_{\bar{\theta}}\Big) - \beta\sin(\theta-\bar{\theta})\mathcal{N}_{\bar{\theta}}\right]d\theta = 0, \quad \forall f\,, \tag{1.40}$$

and since it must hold for all f, we obtain the defining equation for $\chi_{\bar{\theta}}$

$$\partial_\theta\left(\mathcal{N}_{\bar{\theta}}(\theta)\partial_\theta\chi(\theta)\right) = \beta\,\mathcal{N}_{\bar{\theta}}(\theta)\,\sin(\theta-\bar{\theta}). \tag{1.41}$$

The following proposition characterizes the GCI $\chi_{\bar{\theta}}$ as the unique solution to equation (1.41), which depends only on the difference $\theta - \bar{\theta}$. For a detailed construction and proof, we refer to [42].

Proposition 3.5. *Let $\Omega \in \mathbb{S}^1$ be a fixed orientation and write $\Omega = (\cos\bar{\theta}, \sin\bar{\theta})$ for some $\bar{\theta} \in (-\pi, \pi]$. Then the space of Generalized Collisional Invariants (GCI) associated to Ω is the two-dimensional vector space*

$$C_\Omega = \mathrm{Span}\{1, \chi_{\bar{\theta}}\},$$

where $\chi_{\bar{\theta}} = g(\theta - \bar{\theta})$ and g is an odd function. A closed formula for g can be found in [57], where g is defined as

$$g(\Gamma) = \frac{\alpha^2}{k_\theta}\Gamma - \frac{\alpha^2}{k_\theta}\pi\,\frac{\int_0^\Gamma \exp(\frac{-k_\theta\cos(\varphi)}{\alpha^2})d\varphi}{\int_0^\pi \exp(\frac{-k_\theta\cos(\varphi)}{\alpha^2})d\varphi}. \tag{1.42}$$

We will use $\chi_{\bar{\theta}}$ to close the macroscopic equation for the orientation field $\Omega(x,t)$ by integrating the kinetic equation against $\chi_\Omega(\theta)$ and passing to the limit $\varepsilon \to 0$.

3.2 Proof of theorem 3.1

Remark 1. *When the meaning is clear from the context, we will omit writing explicitly the integration domain* $(-\pi,\pi]\times\mathbb{R}$ *in integrals over* (θ,ω).

By assumption, f^ε converges to f^0 as $\varepsilon\to 0$. Then we have:

$$Q(f^0)=0,$$

which means that f^0 is an equilibrium. Thanks to Lemma 3.2, f^0 is of the form

$$f^0=\rho^0\,\mathcal{N}_{\bar\theta_0}(\theta)\,\mathcal{M}_{\bar\omega_0}(\omega),$$

where $\rho^0=\rho^0(t,x)$, $\theta_0=\theta_0(t,x)$, and $\bar\omega_0=\bar\omega_0(t,x)$. Moreover $\mathcal{N}_{\bar\theta_0}$ and $\mathcal{M}_{\bar\omega_0}$ are the normalized distributions defined in (1.24). To determine the evolution of the unknown ρ^0, we first integrate the kinetic equation over (θ,ω) and obtain the conservation equation:

$$\partial_t\rho^\varepsilon+\nabla_x\cdot j^\varepsilon=0,$$

where the flux j^ε is defined by:

$$j^\varepsilon=\int\vec\tau(\theta)\,f^\varepsilon\,d\theta\,d\omega.$$

Because $\int_{\mathbb{R}}\mathcal{M}_{\bar\omega_0}(\omega)\,d\omega=1$, in the limit for $\varepsilon\to 0$, we obtain

$$j^0\;=\;\rho^0\int_{-\pi}^{\pi}\vec\tau(\theta)\,\mathcal{N}_{\bar\theta_0}(\theta)\,d\theta\;=\;\rho^0\int_{-\pi}^{\pi}\vec\tau(\theta)\,\frac{e^{\kappa\cos(\theta-\bar\theta_0)}}{2\pi I_0(\kappa)}\,d\theta,$$

where $\kappa=k_\theta/\alpha^2$. Moreover

$$\int_{-\pi}^{\pi}\vec\tau(\theta)\,\frac{e^{\kappa\cos(\theta-\bar\theta_0)}}{2\pi I_0(\kappa)}\,d\theta=\int_{-\pi}^{\pi}(\cos\theta,\sin\theta)\,\frac{e^{\kappa\cos(\theta-\bar\theta_0)}}{2\pi I_0(\kappa)}\,d\theta\,,$$

and we set $\Gamma=\theta-\bar\theta_0$, obtaining

$$\int_{-\pi-\theta_0}^{\pi-\theta_0}(\cos(\Gamma+\theta_0),\sin(\Gamma+\theta_0))\,\frac{e^{k\cos\Gamma}}{2\pi I_0(\kappa)}\,d\Gamma=\int_{-\pi}^{\pi}(\cos(\Gamma+\theta_0),\sin(\Gamma+\theta_0))\,\frac{e^{k\cos\Gamma}}{2\pi I_0(\kappa)}\,d\Gamma\,,$$

where in the last equality we have used the fact that each term is $2\pi-$periodic. We now use

$$(\cos(\Gamma+\theta_0),\sin(\Gamma+\theta_0))^T=\begin{pmatrix}\cos\Gamma\cos\theta_0-\sin\Gamma\sin\theta_0\\ \sin\Gamma\cos\theta_0+\cos\Gamma\sin\theta_0\end{pmatrix},$$

Since $\sin\Gamma\,e^{\kappa\cos\Gamma}$ is odd, its integral vanishes, while the $\cos\Gamma$ part yields

$$\int_{-\pi}^{\pi}\cos\Gamma\,\frac{e^{\kappa\cos\Gamma}}{2\pi I_0(\kappa)}\,d\Gamma\;=\;\frac{I_1(\kappa)}{I_0(\kappa)}=c_1.$$

We can the conclude that

$$\int_{-\pi}^{\pi} \vec{\tau}(\theta)\, \frac{e^{\kappa \cos(\theta-\bar{\theta}_0)}}{2\pi I_0(\kappa)}\, d\theta = c_1(\cos\theta_0, \sin\theta_0) = c_1\Omega^0\,,$$

where $\Omega^0 = (\cos\theta_0, \sin\theta_0)$. Hence, in the limit $\varepsilon \to 0$, we obtain:

$$j^\varepsilon \xrightarrow{\varepsilon\to 0} j^0 = c_1\rho^0\Omega^0\,.$$

Therefore, ρ^0 satisfies the macroscopic mass conservation equation

$$\partial_t\rho^0 + c_1\nabla_x\cdot(\rho^0\Omega^0) = 0.$$

To derive the evolution equation for the mean angular velocity $\overline{\omega}^0$, we multiply the kinetic equation (1.22) by ω and integrate over (θ, ω). We obtain

$$\partial_t(\rho^\varepsilon\overline{\omega}^\varepsilon) + \nabla_x\cdot\Big(\int \omega\,\vec{\tau}(\theta)\, f^\varepsilon\, d\theta\, d\omega\Big) = \frac{1}{\varepsilon}\int \omega\, Q(f^\varepsilon)\, d\theta\, d\omega + \mathcal{O}(\varepsilon).$$

The right-hand side integral is equal to zero for all ε, indeed

$$\begin{aligned}\int \omega\, Q(f^\varepsilon)\, d\theta\, d\omega = k_\theta \int \omega\, \partial_\theta\Big(f^\varepsilon F_{f^\varepsilon}\Big)\, d\theta\, d\omega + \alpha^2\int \omega\,\partial_\theta^2 f^\varepsilon\, d\theta\, d\omega \\ + k_\omega\int \omega\,\partial_\omega\Big(f^\varepsilon G_{f^\varepsilon}\Big)\, d\theta\, d\omega + \beta^2\int \omega\,\partial_\omega^2 f^\varepsilon\, d\theta\, d\omega\,,\end{aligned} \tag{1.43}$$

where the first two terms are zero by the fact that f is $2\pi-$ periodic and the fundamental theorem of calculus. For the third term we integrate by part and since $G_f = \bar{\omega}_f - \omega$ we have

$$-k_\omega\int(\bar{\omega}_f - \omega)\, f^\varepsilon d\theta d\omega = -k_\omega\,\bar{\omega}_f\rho^\varepsilon - k_\omega\int \omega f^\varepsilon d\theta d\omega = 0.$$

Similarly to the first two terms, also the term multiplying β^2 is equal to zero. Moreover, in the limit for $\varepsilon \to 0$, we have that

$$\int \omega\,\vec{\tau}(\theta)\, f^\varepsilon\, d\theta\, d\omega \xrightarrow{\varepsilon\to 0} \rho^0\overline{\omega}^0\int \vec{\tau}(\theta)\,\mathcal{N}_{\bar{\theta}_0}(\theta)\, d\theta = c_1\rho^0\overline{\omega}^0\Omega^0,$$

since $\overline{\omega}^0 = \int \omega\mathcal{M}_{\overline{\omega}_0}$ and c_1 is defined as before. We thus obtain the second macroscopic equation:

$$\partial_t(\rho^0\overline{\omega}^0) + c_1\nabla_x\cdot(\rho^0\overline{\omega}^0\Omega^0) = 0. \tag{1.44}$$

Now to obtain the equation for the mean orientation $\Omega = \Omega(t,x)$, we multiply (1.22) by the GCI $\chi_{\bar{\theta}_\varepsilon}$, where $\Omega^\varepsilon = \Omega_{f^\varepsilon}$, and integrate with respect to θ and ω. By (1.37) we have that

$$\int Q(f^\varepsilon)\chi_{\bar{\theta}_\varepsilon} d\theta\, d\omega = 0\,. \tag{1.45}$$

i.e.

$$\int I_\theta(f^\varepsilon)\chi_{\bar{\theta}_\varepsilon}\, d\theta = \int \mathcal{I}(f^\varepsilon;\overline{\theta}_f^\varepsilon)\,\chi_{\bar{\theta}_\varepsilon} d\theta = 0\,. \tag{1.46}$$

Hence we obtain that

$$\int \Big(\partial_t f^\varepsilon + \vec{\tau}(\theta)\cdot\nabla_x f^\varepsilon\Big)\chi_{\bar\theta_\varepsilon}(\theta)d\theta\,d\omega + \int \omega\partial_\theta f^\varepsilon\,\chi_{\bar\theta\varepsilon}(\theta)d\theta\,d\omega = 0\,, \tag{1.47}$$

which, in a more compact form, can be written as

$$\int \Big(\mathcal{T}^1 f^\varepsilon + \mathcal{T}^2 f^\varepsilon + \mathcal{T}^3 f^\varepsilon\Big)\chi_{\bar\theta_\varepsilon}(\theta)\,d\theta\,d\omega = 0\,, \tag{1.48}$$

where $\mathcal{T}^1, \mathcal{T}^2$, and $\mathcal{T}^3$ are defined by the following operator

$$\begin{aligned}\mathcal{T}^1 f &= \partial_t f\,,\\ \mathcal{T}^2 f &= \vec{\tau}(\theta)\cdot\nabla_x f\,,\\ \mathcal{T}^3 f &= \omega\partial_\theta f\,.\end{aligned} \tag{1.49}$$

We note that $\chi_{\bar\theta_\varepsilon}$ is smooth enough and therefore $\chi_{\bar\theta_\varepsilon}\to\chi_{\bar\theta_0}$ for $\varepsilon\to 0$. Hence in the limit $\varepsilon\to 0$ we get:

$$\int\Big[\partial_t\Big(\rho\mathcal{N}_{\bar\theta_0}(\theta)\,\mathcal{M}_{\bar\omega_0}(\omega)\Big)+\vec{\tau}(\theta)\cdot\nabla_x\Big(\rho\mathcal{N}_{\bar\theta_0}(\theta)\,\mathcal{M}_{\bar\omega_0}(\omega)\Big)+\omega\partial_\theta\Big(\rho\mathcal{N}_{\bar\theta_0}(\theta)\,\mathcal{M}_{\bar\omega_0}(\omega)\Big)\Big]\chi_{\bar\theta_0}\,d\theta\,d\omega = 0. \tag{1.50}$$

We start to compute the contribution of the operator $\mathcal{T}^1$ and separate each term, obtaining

$$\mathcal{T}^1 = (\partial_t\rho^0)\mathcal{N}_{\bar\theta_0}\mathcal{M}_{\bar\omega_0} + \rho^0\,(\partial_t\mathcal{N}_{\bar\theta_0})\mathcal{M}_{\bar\omega_0} + \rho^0\,\mathcal{N}_{\bar\theta_0}(\partial_t\mathcal{M}_{\bar\omega_0})\,,$$

where the first term vanishes upon integration against $\chi_{\bar\theta}$, due to the odd symmetry of $g(\theta-\bar\theta)$ and the even symmetry of $\mathcal{N}_{\bar\theta}$. The third term vanishes due to the identity

$$\int(\omega-\bar\omega)\mathcal{M}_{\bar\omega}(\omega)\,d\omega = 0.$$

Therefore, the only non zero term is

$$\begin{aligned}\int\mathcal{T}^1\,d\theta d\omega &= \frac{k_\theta}{\alpha^2}\rho\,\partial_t\bar\theta_0\int\sin(\theta-\bar\theta)\,\mathcal{N}_{\bar\theta}(\theta)\,g(\theta-\bar\theta)\,d\theta\\ &= \frac{k_\theta}{\alpha^2}\,\rho^0\,\partial_t\bar\theta_0\int\sin(\theta)\,\mathcal{N}_0\,g(\theta)\,d\theta\\ &= K_1\,\frac{k_\theta}{\alpha^2}\,\rho^0\,\partial_t\bar\theta_0\,,\end{aligned} \tag{1.51}$$

where in the last equality we have performed a change of variables, used the fact that g is a 2π periodic function and defined the constant

$$K_1 := \int\sin(\theta)\,\mathcal{N}_0(\theta)\,g(\theta)\,d\theta\,. \tag{1.52}$$

We now compute the transport term

$$\begin{aligned}\mathcal{T}^2 =&\Big(\vec{\tau}(\theta)\cdot\nabla_x\rho^0\Big)\mathcal{N}_{\bar\theta_0}(\theta)\mathcal{M}_{\bar\omega_0}(\omega) + \rho^0\,(\vec{\tau}(\theta)\cdot\nabla_x\bar\theta_0)\,\partial_{\bar\theta}\mathcal{N}_{\bar\theta_0}(\theta)\,\mathcal{M}_{\bar\omega_0}(\omega)\\ &+\rho^0\,\mathcal{N}_{\bar\theta_0}(\theta)\,(\vec{\tau}(\theta)\cdot\nabla_x\bar\omega_0)\,\partial_{\bar\omega}\mathcal{M}_{\bar\omega_0}(\omega) = \mathcal{T}_1^2+\mathcal{T}_2^2+\mathcal{T}_3^2.\end{aligned}$$

We use the decomposition $\vec{\tau}(\theta) = \cos(\Gamma)\,\Omega^0 + \sin(\Gamma)\,(\Omega^0)^\perp$, where $\Gamma = (\theta - \overline{\theta})$ and $(\Omega^0)^\perp = (-\sin\theta_0, \cos\theta_0)$, which leads to

$$\begin{aligned}\int \mathcal{T}_1^2 d\theta d\omega &= \int (\vec{\tau}(\theta)\cdot\nabla_x\rho)\,\mathcal{N}_{\bar{\theta}}\,\mathcal{M}_{\bar{\omega}}\,g(\theta-\overline{\theta})\,d\theta\,d\omega \\ &= \int (\vec{\tau}(\theta)\cdot\nabla_x\rho)\,\mathcal{N}_{\bar{\theta}_0}\,g(\theta-\overline{\theta})\,d\theta \\ &= \nabla_x\rho^0\cdot\int \sin(\theta-\overline{\theta})\mathcal{N}_{\bar{\theta}_0}g(\theta-\overline{\theta})\,d\theta\,(\Omega^0)^\perp\,, \\ &= K_1\nabla_x\rho^0\cdot(\overline{\Omega}^0)^\perp\,,\end{aligned} \tag{1.53}$$

due to the symmetry of the integrand. The second term gives:

$$\begin{aligned}\int \mathcal{T}_2^2 d\theta d\omega &= \int \rho^0\,(\vec{\tau}(\theta)\cdot\nabla_x\bar{\theta}_0)\,\partial_{\bar{\theta}}\mathcal{N}_{\bar{\theta}_0}(\theta)\,\mathcal{M}_{\bar{\omega}_0}(\omega)\,g(\theta-\overline{\theta})\,d\theta\,d\omega \\ &= \rho^0\frac{k_\theta}{\alpha^2}\nabla_x\overline{\theta}_0\cdot\int\vec{\tau}(\theta)\,\sin(\theta-\overline{\theta})\mathcal{N}_{\bar{\theta}_0}(\theta)\,g(\theta-\overline{\theta})\,d\theta \\ &= \rho^0\frac{k_\theta}{\alpha^2}\nabla_x\overline{\theta}_0\cdot\int(\cos\Gamma\Omega^0+\sin\Gamma(\Omega^0)^\perp)\sin\Gamma\,\mathcal{N}_{\bar{\theta}_0}g(\Gamma)d\theta \\ &= \rho^0\frac{k_\theta}{\alpha^2}\nabla_x\overline{\theta}_0\cdot\int\cos(\theta-\overline{\theta})\,\sin(\theta-\overline{\theta})\mathcal{N}_{\bar{\theta}_0}g(\theta-\overline{\theta})\,d\theta\,\Omega^0 \\ &= \rho^0\,\frac{k_\theta}{\alpha^2}K_2\,(\nabla_x\bar{\theta}_0\cdot\Omega^0),\end{aligned} \tag{1.54}$$

where

$$K_2 := \int\cos(\Gamma)\,\sin(\Gamma)\,\mathcal{N}_0(\Gamma)\,g(\Gamma)\,d\Gamma. \tag{1.55}$$

Finally, $\int\mathcal{T}_3^2 d\theta d\omega = 0$ since $\int_\omega\partial_{\bar{\omega}}\mathcal{M}_{\bar{\omega}_0}(\omega)\,d\omega = 0$. Therefore, the total contribution from the transport term is

$$\int\mathcal{T}^2 d\theta d\omega = K_1\,\nabla_x\rho^0\cdot(\Omega^0)^\perp + \rho^0\,\frac{k_\theta}{\alpha^2}K_2\,(\nabla_x\bar{\theta}_0\cdot\Omega^0)\,,$$

and thus

$$\int\left(\mathcal{T}^1 f^\varepsilon + \mathcal{T}^2 f^\varepsilon\right)\chi_{\bar{\theta}_\varepsilon}(\theta)\,d\theta\,d\omega = K_1\,\frac{k_\theta}{\alpha^2}\,\rho^0\,\partial_t\overline{\theta}_0 + K_1\nabla_x\rho^0\cdot(\overline{\Omega}^0)^\perp + \rho^0\,\frac{k_\theta}{\alpha^2}K_2\,(\nabla_x\bar{\theta}_0\cdot\Omega^0). \tag{1.56}$$

We now compute the contribution of the angular transport term $\mathcal{T}_3$:

$$\begin{aligned}\int\mathcal{T}_3 d\theta d\omega &= \int\omega\,\mathcal{M}_{\bar{\omega}_0}\,\partial_\theta\left(\rho\,\mathcal{N}_{\bar{\theta}_0}(\theta)\,(\omega)\right)\Big)g(\theta-\bar{\theta}_0)\,d\theta\,d\omega \\ &= -\frac{k_\theta}{\alpha^2}\omega^0\rho^0\int\sin(\theta-\overline{\theta}_0)\mathcal{N}_{\bar{\theta}_0}g(\theta-\overline{\theta}_0)\,d\theta \\ &= -K_1\frac{k_\theta}{\alpha^2}\omega^0\rho^0\end{aligned} \tag{1.57}$$

Combining (1.56) and (1.57) yields:

$$K_1\,\frac{k_\theta}{\alpha^2}\,\rho^0\,\partial_t\overline{\theta}_0 + K_1\nabla_x\rho^0\cdot(\overline{\Omega}^0)^\perp + \rho^0\,\frac{k_\theta}{\alpha^2}K_2\,(\nabla_x\bar{\theta}_0\cdot\Omega^0) - K_1\frac{k_\theta}{\alpha^2}\omega^0\rho^0 = 0. \tag{1.58}$$

Using that vector $\Omega^0 = \vec{\tau}(\bar{\theta}_0)$, elementary computations show that:

$$\partial_t \Omega^0 = \partial_t \bar{\theta}_0 \, (\Omega^0)^\perp \qquad \text{and} \qquad (\Omega^0 \cdot \nabla_x)\Omega^0 = ((\Omega^0)^\perp \otimes \Omega^0) \, \nabla_x \bar{\theta}_0. \tag{1.59}$$

Therefore, multiplying equation (1.58) by $(\Omega^0)^\perp$ leads finally to (dropping the superscript for simplicity of notation):

$$\rho\Big(K_1 \frac{k_\theta}{\alpha^2} \partial_t \Omega + K_2 \frac{k_\theta}{\alpha^2} (\Omega \cdot \nabla_x)\Omega - K_1 \frac{k_\theta}{\alpha^2} \overline{\omega}\, \Omega^\perp \Big) + K_1 P_{\Omega^\perp} \nabla_x \rho = 0 \,, \tag{1.60}$$

where $P_{\Omega^\perp} = \mathrm{Id} - \Omega \otimes \Omega$ is the projection operator onto $\Omega^\perp$. This concludes the formal derivation of the macroscopic system stated in Theorem 3.1.

3.3 Periodic solutions

We consider the macroscopic system (1.26)–(1.28) under the assumptions that the both the density and the average angular velocities are homogeneous in time and space, *i.e.,* $\rho(t,x) \equiv \rho_0 > 0$, $\overline{\omega}(t,x) \equiv \omega_0 \neq 0$. Hence from both (1.26) and (1.27) we obtain that also Ω is homogeneous in space. Moreover we plug the identities

$$\partial_t \Omega = \dot{\theta}(t)\, \Omega^\perp(t), \qquad \text{where} \quad \Omega^\perp(t) := (-\sin\theta(t), \cos\theta(t)).$$

into (1.28) and obtain

$$\rho_0 K_1 \frac{k_\theta}{\alpha^2} \left(\dot{\theta}(t) - \omega_0 \right) \Omega^\perp(t) = 0.$$

Since $\rho_0 > 0$ and $\Omega^\perp(t) \neq 0$, we conclude

$$\dot{\theta}(t) = \omega_0.$$

and integrating in time yields

$$\theta(t) = \theta_0 + \omega_0 t.$$

Therefore, the orientation evolves as

$$\Omega(t) = (\cos(\theta_0 + \omega_0 t), \sin(\theta_0 + \omega_0 t)) \,.$$

and the motion is clearly periodic in time with period $T = \frac{2\pi}{|\omega_0|}$, so that $\Omega(t+T) = \Omega(t)$.

4 Simulation of the microscopic model

In this section, we provide additional details on the numerical methods used to produce the simulations shown in Section 4.2. The code is freely available on the GitHub page of the second author at

https://github.com/MoschellaCa/Vicsek-Kuramoto/blob/main/paper_version/vicsek_kuramoto

4.1 Numerical integration of the particle system

We simulate the discrete particle system (1.1)–(1.3) in dimension $n = 2$ on a periodic square domain. The time integration is performed using a modified Euler–Maruyama scheme with adaptive time stepping. The adaptive time stepping is significant in this setting due to the potential stiffness introduced by certain parameter regimes. The implementation uses the `StochasticDiffEq.jl` package in Julia [105].

Although simulating mean-field particle systems is conceptually straightforward, the computational cost becomes significant when the number of particles is large, especially due to the computation of the interaction terms. To address this issue, we implement a Verlet neighbor list method that restricts the computation of the interaction forces to particles located within a fixed cutoff radius. The spatial domain is partitioned into a regular grid of cells, and during each update, interaction forces are computed only among particles that belong to the same or adjacent cells. This approach avoids unnecessary distance checks and reduces the computational complexity from $\mathcal{O}(N^2)$ to approximately $\mathcal{O}(N)$. The method is implemented using the `CellListMap.jl` package [86], which provides optimized routines for evaluating interaction kernels in two and three-dimensional periodic domains.

Simulations are conducted in a periodic square $[0, L_x] \times [0, L_y]$ with $L = L_x = L_y = 64$, and the number of particles is fixed at $N = 15{,}000$. The initial positions $(x_1, x_2)_i$ and directions θ_i of the particles are taken uniform and random for $i = 1, ..., N$ in $[0, L]$ and $[0, 2\pi]$ respectively, while the initial angular velocities ω_i are sampled from an asymmetric distribution. Indeed for a quarter of the particles we prescribe $\omega_i = 5 \cdot \text{rand}()$, where `rand()` denotes a uniform random variable on $[0, 1]$. For the remaining three-quarters, we set $\omega_i = -5 \cdot \text{rand}()$. This choice ensures that the local mean angular velocity is different from zero, thereby avoiding the particles relaxing toward a non-rotating state, which would prevent the formation of the patterns discussed in Section 4.2. All the simulations are run with a time step $\Delta t = 0.01$ and integrated up to a final time $t_{\text{end}} = 0.01 \times 2 \cdot 10^4$.

4.2 Patterns: phase diagrams

In this section, we present the results of the numerical simulations of the individual-based model (1.1)–(1.3) for various values of the alignment parameters k_θ and k_ω. In particular, Figure 1.1 shows the output of the simulations after time $t^* = 0.01 \times 1.9 \cdot 10^4$. At time t^*, the system have reached a steady state. In these figures, particles are represented as dots, and their color gives their orientation. The simulation results are organized in a table format, with columns (from left to right) corresponding to increasing values of the angular velocity alignment strength k_ω, and rows (from bottom to top) corresponding to increasing values of the orientation alignment coefficient k_θ. Moreover we refer the reader to the

caption of Figure 1.1 for the precise values of k_θ and k_ω used in each simulation. Among all the results, we select three representative cases that illustrate the main qualitative patterns observed across the parameter space. Videos corresponding to these cases are provided in the supplementary material (Appendix A), where additional details are provided.

Table 1.1: Parameters used for the microscopic simulations. The values considered for k_θ and k_ω are specified in the caption of the corresponding figures.

parameters	**value**	**description**
N	15 000	total number of individuals
k_θ	various	interaction strength in the direction variable
k_ω	various	interaction strength in the angular velocity variable
t_{end}	200	final time of the simulation
$\sqrt{2\alpha^2}$	0.5	angular noise in orientation dynamics
$\sqrt{2\beta^2}$	0.5	noise in angular velocity dynamics
dt	0.01	time step size
R	2	interaction radius
v_0	1	constant velocity of particles
L	64	size of the periodic domain

In Figure 1.1, we observe a rich spectrum of emergent collective behaviors as we explore the influence of different values of k_θ and k_ω. We classify the observed patterns into three main types, each highlighted in the figure using different colored frames corresponding to distinct regions in parameter space:

- **Rotating clusters** (framed in light blue): Agents self-organize into compact, rotating clusters within the domain. This pattern predominantly arises from weak angular velocity alignment ($k_\omega = 1$) combined with weak to moderate orientation alignment ($k_\theta = 1, 11, 21$).

- **Traveling waves in orientation** (framed in red): For small to moderate orientation alignment ($k_\theta = 1, 11, 21$) and moderate to strong angular velocity alignment ($k_\omega = 11, 61, 81$), the agents arrange themselves in configurations where the spatial density remains nearly uniform, but the orientation propagates as a traveling wave in the domain. Snapshots illustrating the traveling wave are shown in Figure 1.2.

- **Pulsating behavior** (framed in purple): We refer to the pulsating regime as a global, synchronized state characterized by large-scale, time-periodic oscillations in the mean orientation of the system. This regime emerges for large values of both the

alignment parameters, typically $k_\theta = 61, 71$ and $k_\omega = 51, 61, 81$. It represents the most stable and recurrent pattern observed in the regime characterized by strong alignment interactions. Although we show only a representative subset in Figure 1.1 for clarity of presentation, extensive simulations indicate that for $k_\theta, k_\omega \gtrsim 50$, the pulsating regime dominates the long-time dynamics of the system. Snapshots illustrating the pulsating behaviour are shown in Figure 1.3.

Finally, the simulations not enclosed in colored frames do not exhibit any clearly ordered or persistent collective behavior.

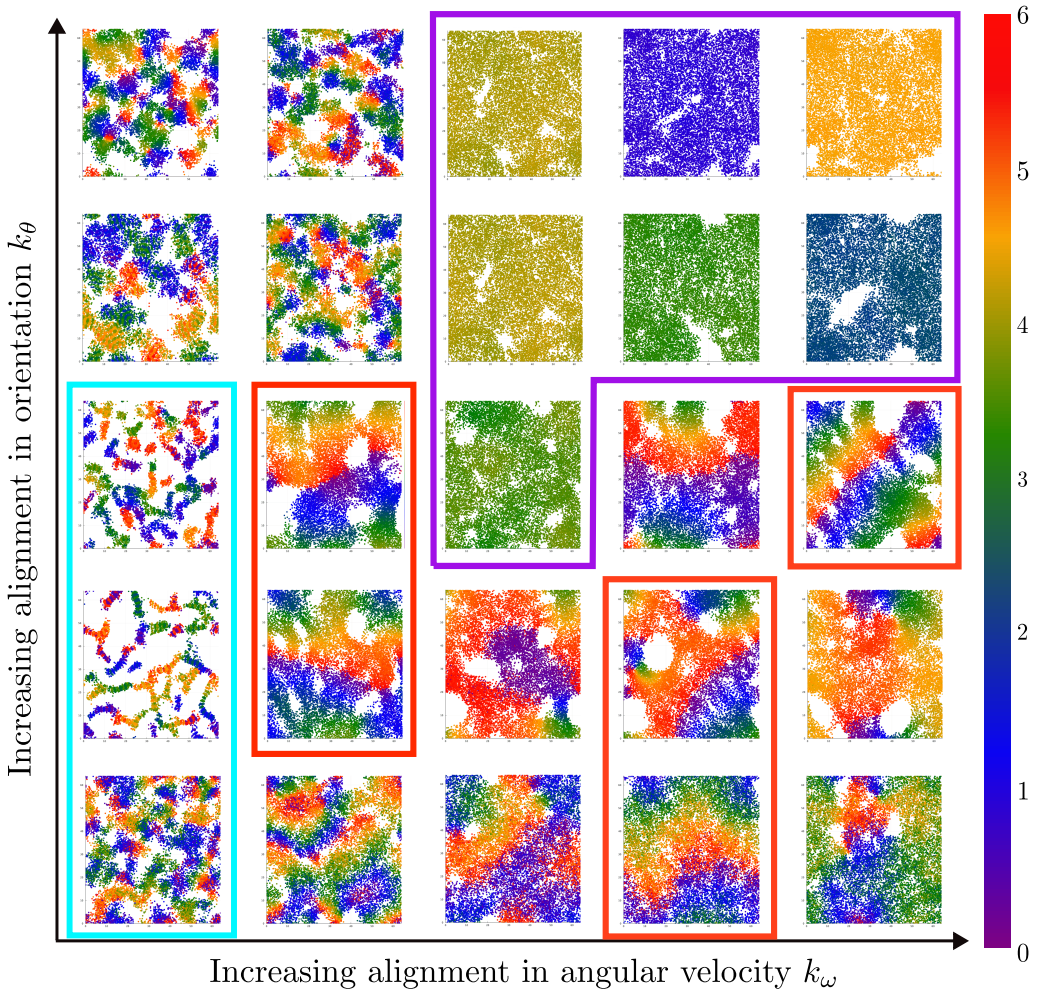

Figure 1.1: Results of microscopic simulations for varying values of the alignment parameters k_θ and k_ω, with all other parameters fixed as reported in Table 1.1. Each simulation involves 15,000 agents interacting within an interaction radius $R = 2$. The columns (from left to right) correspond to increasing values of the angular velocity alignment strength $k_\omega = 1, 11, 51, 61, 81$, while the rows (from bottom to top) correspond to increasing values of the directional alignment strength $k_\theta = 1, 11, 21, 61, 71$. The colormap, shown on the right hand side of the figure, provides the correspondence between orientation angles and colors.

5 Simulation of the macroscopic model

In this section, we present the numerical scheme used to simulate the macroscopic system (1.26)–(1.28). A central difficulty in the numerical treatment of systems like (1.26)–(1.28) arises from the fact that the equation governing the evolution of the mean direction Ω is not written in a conservative form. As a result, the weak solutions of the macroscopic system (1.26)–(1.28) are not uniquely defined in the presence of discontinuities: the

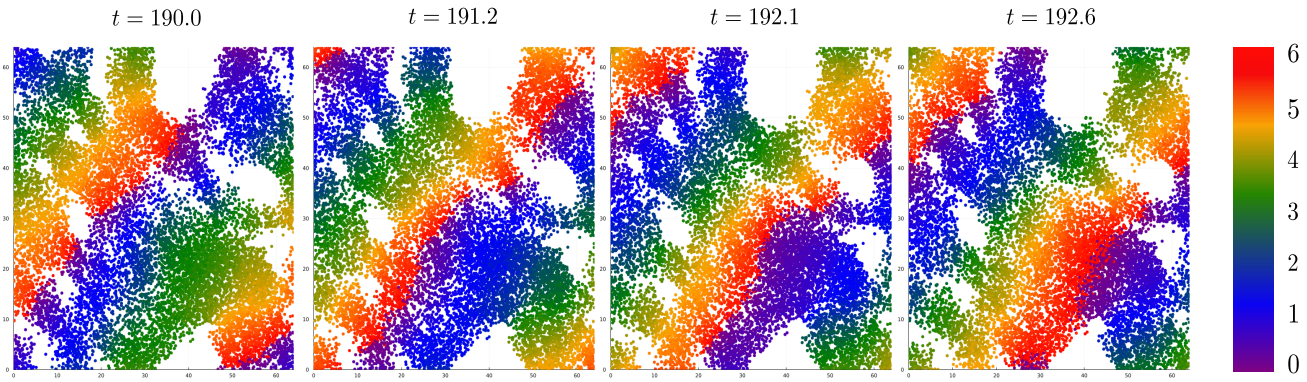

Figure 1.2: Sequence of snapshots showing the emergence of a traveling wave in orientation for alignment parameters $k_\theta = 21$ and $k_\omega = 81$. The system evolves towards a state with nearly uniform spatial density, while the orientation field propagates with a wave-like motion across the domain. The corresponding video can be found in Appendix A (Video 2).

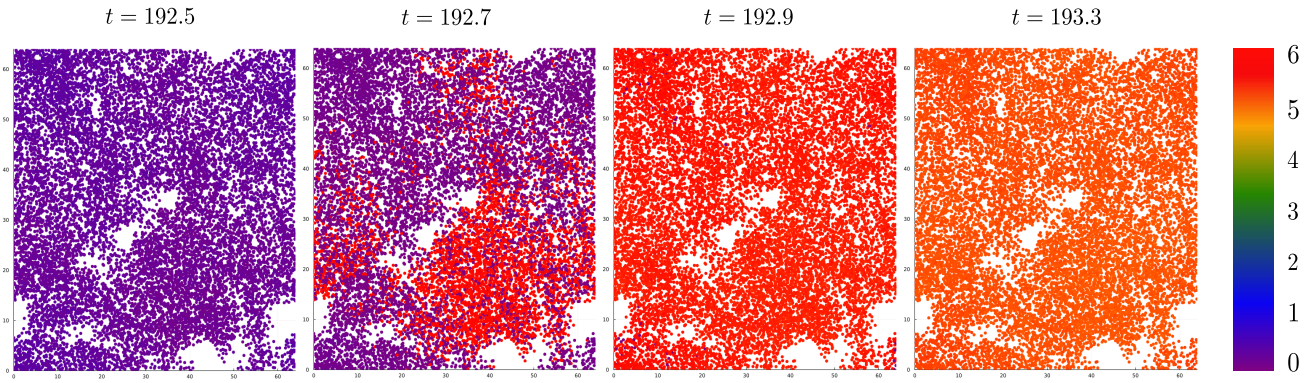

Figure 1.3: Sequence of snapshots illustrating the steady-state dynamics for alignment parameters $k_\theta = k_\omega = 71$. To highlight the pulsating behavior, we display multiple time frames from the same simulation. The particles rotate collectively as a rigid body, with the orientation field evolving in time across the entire domain. This global rotation characterizes the pulsating regime, where the direction of motion changes uniformly for all the particles in the domain, while the distribution of particles remains uniform in space. The corresponding video can be found in Appendix A (Video 3).

absence of a conservative formulation precludes the use of standard jump conditions (such as the Rankine–Hugoniot relations), and the lack of an associated entropy inequality prevents the application of entropy-based admissibility criteria commonly used to select physically relevant solutions in conservative hyperbolic systems. This issue has been addressed in [91] in the context of the Self-Organized Hydrodynamics (SOH) model. The authors showed that the SOH model can be recovered as the limit of a conservative system

in which the velocity field does not have any geometrical constraint. Moreover, they showed that the numerical solutions obtained via this relaxation limit approach align well with the behavior of the original microscopic model. In contrast, solutions constructed directly from the non-conservative SOH system can fail to capture the correct dynamics of the model and may deviate significantly from the underlying microscopic description. Following this approach, it is possible to show that the macroscopic system (1.26)–(1.28) can be obtained as a relaxation limit for $\eta \to 0$ of the following conservative system with source term:

$$\partial_t \rho^\eta + c_1 \nabla_x \cdot (\rho^\eta \Omega^\eta) = 0\,, \tag{1.61}$$

$$\partial_t \left(\rho^\eta \omega^\eta\right) + c_1 \nabla_x \cdot (\rho^\eta \omega^\eta \Omega^\eta) = 0\,, \tag{1.62}$$

$$\partial_t \left(\rho^\eta \Omega^\eta\right) + \frac{K_2}{K_1} \nabla_x \cdot (\rho^\eta \Omega^\eta \otimes \Omega^\eta) + \nabla_x \rho^\eta - \omega^\eta (\Omega^\eta)^\perp \rho^\eta = \frac{\rho^\eta}{\eta} \left(1 - |\Omega^\eta|^2\right) \Omega^\eta\,, \tag{1.63}$$

where $C = \frac{k_\theta}{\alpha^2}$. The scheme we propose relies on the following steps.

1. We first solve the conservative part of the relaxation system

$$\partial_t \rho^\eta + c_1 \nabla_x \cdot (\rho^\eta \Omega^\eta) = 0\,, \tag{1.64}$$

$$\partial_t \left(\rho^\eta \omega^\eta\right) + c_1 \nabla_x \cdot (\rho^\eta \omega^\eta \Omega^\eta) = 0\,, \tag{1.65}$$

$$\partial_t \left(\rho^\eta \Omega^\eta\right) + \frac{K_2}{K_1} \nabla_x \cdot (\rho^\eta \Omega^\eta \otimes \Omega^\eta + \rho^\eta \mathrm{Id}) = 0\,, \tag{1.66}$$

   which corresponds to a compressible Euler-type system in two dimensions. We use a custom Roe scheme with a Roe matrix computed following [83] page 156.

2. We use a dimensional splitting method, as described in Section 19.5 of [83], to solve the the relaxation part

$$\partial_t \rho^\eta = 0\,, \tag{1.67}$$

$$\partial_t \left(\rho^\eta \omega^\eta\right) = 0\,, \tag{1.68}$$

$$\partial_t \left(\rho^\eta \Omega^\eta\right) = \frac{\rho^\eta}{\eta} \left(1 - |\Omega^\eta|^2\right) \Omega^\eta\,. \tag{1.69}$$

3. Finally, using the same dimensional splitting procedure, we solve the part involving the source term

$$\partial_t \rho^\eta = 0\,, \tag{1.70}$$

$$\partial_t \left(\rho^\eta \omega^\eta\right) = 0\,, \tag{1.71}$$

$$\partial_t \Omega^\eta = \omega^\eta \left(\Omega^\eta\right)^\perp. \tag{1.72}$$

The implementation of our scheme is freely available at:

https://github.com/MoschellaCa/Vicsek-Kuramoto/tree/c646c0dce255a316591addf3d1d47f0e0797600d/paper_version/macro_code

and is a straightforward adaptation of the code provided at

https://github.com/antoinediez/SOH.jl

originally developed for the Self-Organized Hydrodynamics (SOH) model.

Simulations of the macroscopic Vicsek–Kuramoto model are performed on a square periodic domain $[0, L_x] \times [0, L_y]$, with $L_x = L_y = 1$. We fix the time step to $\Delta t = 0.001$ and integrate the system up to final time $t_{\text{end}} = 100$, while $\Delta x = \Delta y = 0.005$. The boundary conditions in both directions are taken to be periodic. The initial conditions for the macroscopic simulations are qualitatively comparable with those used in the microscopic setting. Specifically, the density field $\rho(x, 0)$ is initialized as a spatially homogeneous profile with small random perturbations, while the angular velocity field $w(x, 0)$ is prescribed with a non-zero spatial mean to replicate the asymmetric distribution of angular velocities employed in the simulations of the microscopic system. The mean orientation field $\Omega(x, 0)$ is sampled uniformly from the unit circle.

5.1 Comparison between microscopic and macroscopic simulations

We numerically validate the macroscopic Vicsek–Kuramoto model (1.26)–(1.28) by simulating the particle system (1.6)–(1.8), with parameters chosen according to the scaling regime in Section 2.3, which defines the hydrodynamic limit. We fix the time step to $\Delta t = 0.01$ and the particle speed to $c = 0.1$, so that particles move in a relatively big domain of side length $L = 1$.

Assuming an initial uniform particle distribution, the average number of interacting neighbors per particle is given by

$$N_{\text{neigh}} = \frac{N \pi R^2}{L^2},$$

where R denotes the interaction radius. To ensure that the system operates in the mean-field regime, a good approximation is given by $N_{\text{neigh}} \sim 10^2$. For this reason, we take $N = 2 \cdot 10^4$ and set $R = 0.04$. This choice corresponds to an interaction area of about 0.5% of the total domain, which guarantees the spatial locality required for the validity of the hydrodynamic limit. As detailed in Section 2.3, the interaction radius R acts as the fundamental scaling parameter from which all other parameters in the particle model are derived. For this reason we scale the simulation parameters as

$$k_\theta = \frac{k'_\theta}{R}, \quad k_\omega = \frac{k'_\omega}{R}, \quad \alpha^2 = \frac{(\alpha')^2}{R}, \quad \beta^2 = \frac{(\beta')^2}{R},$$

with k'_θ, k'_ω, α', and β' dimensionless constants. This scaling ensures that alignment and stochastic effects remain significant despite the shrinking spatial range of interactions. As dimensionless constants, we choose $k'_\theta = 1$, $k'_\omega = 1$, and noise intensities $(\alpha')^2 = 0.125$, $(\beta')^2 = 0.125$. At final time $t_{\text{end}} = 100$, the system exhibits the same pulsating behavior observed in earlier simulations: the orientation field rotates uniformly over time, while the spatial density remains approximately constant. A video of the simulation is included in Appendix A (Video 4). To enable a qualitative comparison of the macroscopic simulations with the microscopic ones, we use the same dimensionless parameters k_θ and α, which are the only ones influencing the macroscopic dynamics, in the way that $k_\theta/\alpha^2 = 8$.

5.2 Conclusions

The numerical simulations presented in Sections 4 and 5 provide a qualitative characterization of the patterns that arise in both the microscopic and macroscopic models. The results indicate that the interplay between orientation alignment and angular velocity synchronization is the key mechanism responsible for the emergence of distinct collective behaviors in the IBM. In the regime where both the alignment in angular velocity and direction are weak, the system self-organizes in localized rotating clusters. As the alignment strength in orientation becomes dominant over the one in angular velocity, the system exhibits tighter spatial aggregation, with clusters becoming more compact and localized. Conversely, when angular velocity alignment dominates and the orientation alignment remains weak, the particle distribution tends toward a spatially homogeneous configuration with minimal clustering.

Among the various regimes explored, the pulsating state emerges as the most robust and persistent collective pattern. This regime is typically observed when both alignment strengths are moderate to large. In contrast, traveling waves in the orientation field arise only within a narrow range of parameters, specifically when both the orientation and angular velocity alignment strengths lie in a low-to-intermediate regime. In fact, the macroscopic equations are derived under a hydrodynamic scaling in which both alignment interactions become large as $\varepsilon \to 0$. This could explain why traveling waves do not appear in the macroscopic simulations, which may lie outside the range of validity of the macroscopic approximation considered in this work. Accordingly, while the macroscopic model may initially exhibit localized rotating structures reminiscent of the microscopic clustering regime, this behavior persists only for a few time iterations before being rapidly averaged out. The system then tends toward a globally synchronized rotational state. This behavior is consistent with the hydrodynamic scaling introduced in Section 2.3, which favors the pulsating regime associated with strong alignment interactions.

A more comprehensive investigation of different initial configurations and parameter

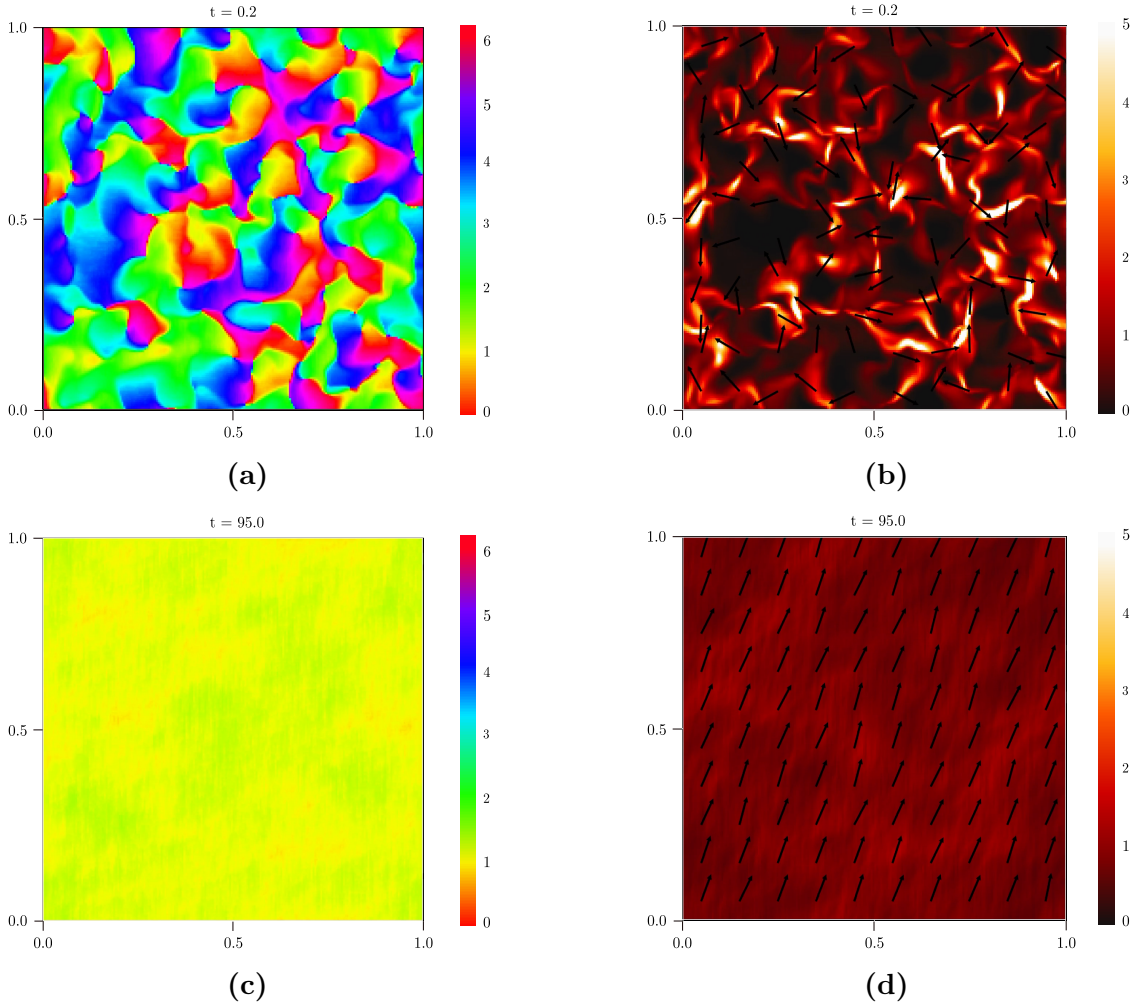

Figure 1.4: Macroscopic simulation of the Vicsek–Kuramoto system with $k_\theta/\alpha^2 = 8$. **(a)** Snapshot at early time $t = 0.20$, showing the formation of localized rotating clusters. These are transient structures similar to those observed in the microscopic simulations with small k_θ and k_ω, corresponding to weak orientational and angular velocity alignment. The color scale represents the density $\rho(x,t)$, while arrows indicate the local mean orientation field $\Omega(x,t)$ computed in each grid cell. The video of the simulation is included in Appendix A (Video 5) **(b)** Same configuration as in (a), with the color scale representing the average orientation angle of each cell grid between $[-\pi,\pi]$. The video of the simulation is included in Appendix A (Video 6) **(c)** Snapshot of Video 5 at time $t = 95.0$. The density ρ becomes nearly uniform in space, and the system reaches a rotating regime driven by a non-zero mean average angular velocity. **(d)** Snapshot of Video 6 at time t =95, with colorbar indicating the angle. The global coherent rotation of the direction field confirms the emergence of a pulsating state, in qualitative agreement with the behavior observed in the microscopic simulations of Video 4.

regimes, aiming to identify additional macroscopic behaviors and clarify their possible connection to the microscopic dynamics, is the subject of ongoing work.

Chapter 2

First order non-instantaneous corrections in collisional kinetic alignment models

Joint work with L. Kanzler and C. Schmeiser

In this work the standard kinetic theory assumption of instantaneous collisions is lifted. As a continuation of [80], a model for higher order non-instantaneous alignment collisions is presented and studied in the asymptotic regime of short collision duration. A first order accurate approximative model is derived as a correction to the instantaneous limit. Rigorous results on its well-posedness and on the instantaneous limit are proven. The approximative model is a system of two equations. An equally accurate scalar approximation is suggested.

Contents

1 Introduction 51

2 System of non-instantaneously interacting particles 53

3 Well-posedness and instantaneous limit for the first order accurate model 60

3.1 Dynamics of the moments 61

3.2 Existence and uniqueness 63

3.3 Instantaneous limit 65

4 A first order accurate, non-instantaneous, scalar model . . 68

1 Introduction

The Boltzmann equation of gas dynamics [26] is based on the simplifying assumption that collisions between particles are hard, i.e., instantaneous, such that the particle

dynamics in phase space is governed by a velocity jump process. The same is true for various kinetic models for living agents like bacteria [6], [13], [21], [22], [70], [74], [92], undergoing spontaneous velocity changes or hard collisions, but also for models of opinion formation, with instantaneous changes of opinion [52], [116]. In gas dynamics, the hard collision assumption also justifies the restriction to binary collisions, since collisions of more than two particles are too rare for having an influence on the particle distribution [26]. There have been efforts, however, to extend the Boltzmann equation to also include three-particle-collisions [5], [109]. Non-instantaneous collisions have apparently only been addressed in the context of quantum particles [85].

In [80] the authors have started an investigation of kinetic models with non-instantaneous collisions considering a model problem for particle alignment, where in binary collision processes of positive duration, the one-dimensional velocity variables of pairs of particles approach their mean value. This can be seen as a version of the Vicsek model [119] (see [17], [20] for kinetic formulations), where the interaction is only pairwise and it is turned on and off stochastically. Two versions of the model have been considered: one where collision processes have deterministic duration and end after the mean value (i.e., complete alignment) has been reached; and another one with stochastic collision duration governed by a Poisson process. The well posedness of the model problems has been studied in [80] as well as their instantaneous limits as the collision duration tends to zero. The instantaneous limit problems are hard collision kinetic models of standard form. The long time limit is a fully aligned state, where the distribution function collapses to a Delta distribution. This is a consequence of the energy loss in the collision processes, a property this model shares with other models for alignment [6], [22], [74], [92], and with the inelastic Boltzmann equation [16], [24], [90].

The present work can be seen as a continuation of [80]. It starts from a model including higher order non-instantaneous collisions, where more than two particles interact. The model, presented in the following section, takes the form of a system of coagulation-fragmentation equations [8] with additional drift terms. Coagulation and fragmentation correspond to (groups of) particles joining and, respectively, leaving a collision process, whose internal dynamics is described by the drift. The main goal is to consider the situation of short collision duration and to find (first order) corrections to the instantaneous limit model.

In the following section the higher order non-instantaneous collision model is presented. Some formal properties are discussed, and the formal asymptotics for short collision duration is presented. In particular, keeping first order corrections to the instantaneous limit problem results in a system of two equations for the distribution of free particles between collisions and for the distribution of pairs of particles involved in binary collision processes. These equations also contain an account of three-particle-collisions. Rigorous

results on this system are contained in Section 3. We prove an existence and uniqueness result for mild solutions as well as a rigorous justification of the instantaneous limit. Section 4 is devoted to the question of finding an equally accurate approximative model, which can be written as a scalar equation for a one-particle distribution. It has already been noted in [80] that the model for non-instantaneous binary collisions can be written as a scalar equation with time delays, which are small for small collision duration. It is then rather straightforward to derive first order corrections by Taylor expansion [50], [82]. Unfortunately, this asymptotic approximation is not structure preserving. For example, the resulting scalar equation does not preserve the nonnegativity of the solution in general. Therefore we propose a scalar model with delays, which is both accurate up to first order and preserves nonnegativity of the solution.

2 System of non-instantaneously interacting particles

We shall present a model, which can be interpreted in terms of different applications of alignment, e.g., myxobacteria [7] or liquid crystals [95]. Here it will be described in terms of opinion formation [116], where the opinion of individuals is represented by the one-dimensional variable $v \in \mathbb{R}$. Individuals may participate in discussion groups of arbitrary size, where the effect of the discussion is that all participants gradually approach the average opinion of the group. Two groups may combine to make a bigger group (this effect includes the possibility of individuals joining a group). On the other hand, a group may split into two smaller groups. Combination and splitting (i.e., coagulation and fragmentation [8]) are governed by Poisson processes with parameters depending on the sizes of the involved groups.

A group of size $k \in \mathbb{N}$ is characterized by the k-tuple $(v_1, \dots, v_k) \in \mathbb{R}^k$ of opinions of its participants. The distribution of groups of size k at time $t \in \mathbb{R}$ will be described by the density $f_k(v_1, \dots, v_k, t) \geq 0$. The assumption of indistinguishability of the individuals has the consequence that f_k is invariant under permutations of $(v_1, \dots, v_k)$. The family $\{f_1, f_2, \dots\}$ satisfies the system

$$\begin{aligned} \partial_t f_k \; + \nabla_{(v_1,\dots,v_k)} \cdot (U_k f_k) = & \frac{1}{2} \sum_{j=1}^{k-1} \lambda_{j,k-j} f_j \odot f_{k-j} - \sum_{j=1}^{\infty} \lambda_{j,k} f_k \int_{\mathbb{R}^j} f_j^* \, d(v_1^*, \dots, v_j^*) \\ & + \sum_{j=1}^{\infty} \mu_{k,j} \int_{\mathbb{R}^j} f_{k+j} \, d(v_{k+1}, \dots, v_{k+j}) - \frac{1}{2} \sum_{j=1}^{k-1} \mu_{j,k-j} f_k \,, \end{aligned} \tag{2.1}$$

$k \geq 1$, where f_k^* denotes evaluation at $(v_1^*, \dots, v_k^*)$, and where the symmetric tensor

product in the first term on the right hand side is defined by

$$(f_j \odot f_{k-j})(v_1, \dots, v_k) := \binom{k}{j}^{-1} \sum_{c \in C(k,j)} f_j(v_c) f_{k-j}(v_{c'}) \,.$$

Here $C(k,j)$ denotes the set of j-combinations of $\{1, \dots, k\}$, and c' is the complement of c. The factors $1/2$ in (2.1) corrects the fact that in the following sums every term appears twice. The parameters of the above mentioned Poisson processes are

- $\lambda_{i,j} = \lambda_{j,i} \geq 0$ for the rate of coagulation between groups of sizes i and j (beginning of collision or discussion processes) ,
- $\mu_{i,j} = \mu_{j,i} \geq 0$ for the rate of fragmentation of a group of size $i + j$ into groups of sizes i and j (end of collision or discussion processes).

The 'acceleration' fields $U_k \in \mathbb{R}^k$, $k \geq 1$, describe the interaction process within a group of k individuals. As indicated above, an alignment process (or trend to the average opinion) is assumed:

$$(U_k)_i := \frac{1}{k} \sum_{j=1}^{k} v_j - v_i \,, \quad i \in \{1, \dots, k\} \,, \qquad k > 1 \,. \tag{2.2}$$

We also define $U_1 = 0$, meaning that individuals not in a discussion group do not change their opinions. The absence of a factor in front of v_i indicates that in a nondimensionalization the relaxation time of the trend towards the average opinion (assumed independent of the size of the discussion group) has been taken as reference time.

Formal properties – moments

The suitability of the model requires certain formal properties. For example, nonnegativity of the distribution functions $f_1, f_2, \dots$ is formally preserved, since all terms with a minus sign on the right hand side of (2.1) have a factor f_k.

Since individuals only change their opinion, their total number should be preserved by the dynamics. Denoting the total number of groups of size k by M_k and the total number of individuals (or the total mass) by M, we have

$$M_k = \int_{\mathbb{R}^k} f_k \, d(v_1, ...v_k) \,, \quad k \geq 1 \,, \qquad M := \sum_{k=1}^{\infty} k \, M_k \,.$$

It turns out that the family $\{M_1, M_2, \dots\}$ solves a closed infinite system of ODEs:

$$\dot{M}_k = \frac{1}{2} \sum_{j=1}^{k-1} \lambda_{j,k-j} M_j \, M_{k-j} - \sum_{j=1}^{\infty} \lambda_{j,k} M_j M_k + \sum_{j=1}^{\infty} \mu_{k,j} M_{k+j} - \frac{1}{2} \sum_{j=1}^{k-1} \mu_{j,k-j} M_k \,, \quad k \geq 1 \,. \tag{2.3}$$

For the rate of change of the total mass we get (with $k = i + j$ in the first and the last term, with the symmetry of the rate constants, and with a symmetrization)

$$\begin{aligned}\dot{M} = \sum_{k=1}^{\infty} k\dot{M}_k =& \frac{1}{2}\sum_{i=1}^{\infty}\sum_{j=1}^{\infty}(i+j)\lambda_{j,i}M_j\,M_i - \sum_{k=1}^{\infty}\sum_{j=1}^{\infty}k\lambda_{j,k}M_k\,M_j \\ &+ \sum_{k=1}^{\infty}\sum_{j=1}^{\infty}k\mu_{k,j}\,M_{k+j} - \frac{1}{2}\sum_{i=1}^{\infty}\sum_{j=1}^{\infty}(i+j)\mu_{j,i}\,M_{i+j} = 0\,,\end{aligned} \tag{2.4}$$

as expected. This book-keeping result is actually independent from the choice of the rate constants $\lambda_{j,k}$, $\mu_{j,k}$, and of the interaction fields U_k.

System (2.3) is actually the standard discrete coagulation-fragmentation model [8]. Since coagulation and fragmentation can be seen as a chemical reaction and its reverse, one might hope for the existence of an equilibrium state, where they are balanced. This question cannot be answered in general, but let us assume that such an equilibrium $\{M_k^\infty\}_{k\geq 1}$ exists, which has the correct total mass,

$$\sum_{k=1}^{\infty} kM_k^\infty = M\,,$$

and also satisfies the *detailed balance* condition

$$\lambda_{j,k}M_j^\infty M_k^\infty = \mu_{j,k}M_{k+j}^\infty\,, \qquad j,k \geq 1\,.$$

By classical results for *mass-action kinetics* [76], the *relative entropy*

$$H\left(\{M_k\}_{k\geq 1}|\{M_k^\infty\}_{k\geq 1}\right) := \sum_{k=1}^{\infty}\left(M_k\log\frac{M_k}{M_k^\infty} - M_k + M_k^\infty\right)$$

is nonincreasing in time. This can be seen by first rewriting the right hand side of (2.3) in terms of $u_k := M_k/M_k^\infty$, $k \geq 1$, and using detailed balance:

$$\dot{M}_k = \frac{1}{2}\sum_{j=1}^{k-1}\mu_{j,k-j}M_k^\infty(u_ju_{k-j} - u_k) + \sum_{j=1}^{\infty}\mu_{j,k}M_{j+k}^\infty(u_{j+k} - u_ju_k)\,.$$

After summation against $\log u_k$ and symmetrization of the second term we obtain

$$\frac{d}{dt}H\left(\{M_k\}_{k\geq 1}|\{M_k^\infty\}_{k\geq 1}\right) = -\frac{1}{2}\sum_{j,k=1}^{\infty}\mu_{j,k}M_{k+j}^\infty(u_{k+j} - u_ju_k)\log\frac{u_{k+j}}{u_ju_k} \leq 0\,.$$

It is easily seen that under the constraint that the total mass of $\{M_k\}_{k\geq 1}$ is M, the right hand side (the *entropy dissipation*) only vanishes for $M_k = M_k^\infty$, $k \geq 1$. This raises the expectation that $\{M_k(t)\}_{k\geq 1}$ converges to $\{M_k^\infty\}_{k\geq 1}$ as $t \to \infty$. It is a classical result due to Aizenman and Bak [3] that this is true for the case that $\lambda_{j,k}, \mu_{j,k}$ are independent from (j,k) (when $\{M_k^\infty\}_{k\geq 1}$ can be computed explicitly).

Since the interaction in each discussion group preserves the average opinion, we expect the same for the whole ensemble. The average opinion is given by

$$v_\infty := \frac{I}{M}\,, \quad \text{with } I = \sum_{k=1}^{\infty} k\, I_k\,, \quad I_k = \frac{1}{k}\int_{\mathbb{R}^k} \sum_{j=1}^{k} v_j\, f_k\, d(v_1,...,v_k) = \int_{\mathbb{R}^k} v_1\, f_k\, d(v_1,...,v_k)\,.$$

The family $\{I_1, I_2, \ldots\}$ of first order moments again solves a closed ODE system (assuming to have solved (2.3)):

$$\begin{aligned} \dot I_k &= \sum_{j=1}^{k-1} \lambda_{j,k-j}\, \frac{j}{k} M_{k-j} I_j - \sum_{j=1}^{\infty} \lambda_{j,k}\, M_j\, I_k + \sum_{j=1}^{\infty} \mu_{k,j} I_{k+j} - \frac{1}{2}\sum_{j=1}^{k-1} \mu_{j,k-j} I_k \\ &=: \varphi_k(\{I_j\}_{j\geq 1}, \{M_j\}_{j\geq 1})\,. \end{aligned} \tag{2.5}$$

The first term on the right hand side needs some explanation: When the symmetric tensor product $f_j \odot f_{k-j}$ in (2.1) is multiplied by v_1 and then integrated, those terms, where v_1 appears in the argument of f_j, produce the contribution $I_j M_{k-j}$. The other terms produce $M_j I_{k-j}$. The first case occurs $\binom{k-1}{j-1}$ times, i.e. with probability $\binom{k-1}{j-1}/\binom{k}{j} = \frac{j}{k}$. Therefore we obtain 2 terms, which turn out to be the same after the coordinate change $j \mapsto k-j$, namely the first term on the right hand side of (2.5).

The derivation of (2.5) also uses the fact that the interaction within the groups does not contribute:

$$\begin{aligned} &\int_{\mathbb{R}^k} v_1 \nabla_{(v_1,...,v_k)} \cdot (U_k\, f_k) d(v_1,...,v_k) = -\int_{\mathbb{R}^k} (U_k)_1 f_k\, d(v_1,...,v_k) \\ &= -\frac{1}{k}\sum_{j=1}^{k} \int_{\mathbb{R}^k} v_j f_k\, d(v_1,...,v_k) + \int_{\mathbb{R}^k} v_1 f_k\, d(v_1,...,v_k) = 0\,. \end{aligned}$$

Similarly to (2.4) we obtain $\dot I = 0$, showing that the average opinion v_∞ is constant in time.

We shall give a heuristic argument that all the average opinions $\overline{v}_k := I_k/M_k$, $k \geq 1$, within groups converge to v_∞ as $t \to \infty$, if the group sizes $\{M_k\}_{k\geq 1}$ converge to a detailed-balance equilibrium $\{M_k^\infty\}_{k\geq 1}$. We start by writing the right hand side of (2.5) in terms of the $\overline{v}_k$ and then approximate it for large t, replacing M_k by M_k^∞:

$$\begin{aligned} \dot I_k &= \sum_{j=1}^{k-1} \lambda_{j,k-j} \frac{j}{k} M_{k-j} M_j \overline{v}_j - \sum_{j=1}^{\infty} \lambda_{j,k}\, M_j\, M_k \overline{v}_k + \sum_{j=1}^{\infty} \mu_{k,j} M_{k+j} \overline{v}_{k+j} - \frac{1}{2}\sum_{j=1}^{k-1} \mu_{j,k-j} M_k \overline{v}_k \\ &\approx \frac{1}{2}\sum_{j=1}^{k-1} \mu_{j,k-j} M_k^\infty \left(\frac{j}{k}\overline{v}_j + \frac{k-j}{k}\overline{v}_{k-j} - \overline{v}_k \right) + \sum_{j=1}^{\infty} \mu_{k,j} M_{k+j}^\infty (\overline{v}_{k+j} - \overline{v}_k) \end{aligned}$$

The distance of the average opinions to v_∞ can be measured by the quadratic relative entropy

$$\frac{1}{2}\sum_{k=1}^{\infty} k M_k (\overline{v}_k - v_\infty)^2 \approx \frac{1}{2}\sum_{k=1}^{\infty} k \frac{I_k^2}{M_k^\infty} - v_\infty I + \frac{1}{2} v_\infty^2 M\,,$$

and therefore

$$\frac{d}{dt}\frac{1}{2}\sum_{k=1}^{\infty} kM_k(\overline{v}_k - v_\infty)^2 \approx \sum_{k=1}^{\infty} k\overline{v}_k\dot{I}_k \approx -\sum_{i,j=1}^{\infty}\mu_{i,j}M_{i+j}^{\infty}i(\overline{v}_i - \overline{v}_{i+j})^2\,.$$

This suggests that all $\overline{v}_k(t)$ tend to the same value as $t\to\infty$, which has to be v_∞ by the conservation of the average opinion. As a consequence of the discussion processes, it is plausible to expect that not only the average opinions of all discussion groups but also the opinion of each individual approaches v_∞. This can be checked by introducing the variance

$$V = \sum_{k=1}^{\infty} kV_k\,,$$

with

$$V_k = \int_{\mathbb{R}^k}(v_1 - v_\infty)^2 f_k\, d(v_1,...,v_k) = E_k - 2v_\infty I_k + v_\infty^2 M_k\,, \qquad E_k = \int_{\mathbb{R}^k} v_1^2 f_k\, d(v_1,...,v_k)\,.$$

For $k>1$ the time derivative of E_k contains a contribution from the discussion process:

$$\begin{aligned}&\int_{\mathbb{R}^k} v_1^2\,\nabla_{(v_1,...,v_k)}\cdot(U_k\,f_k)d(v_1,...,v_k) = -2\int_{\mathbb{R}^k} v_1(U_k)_1 f_k\, d(v_1,...,v_k)\\ &= -\frac{2}{k^2}\sum_{i=1}^{k}\sum_{j=1}^{k}\int_{\mathbb{R}^k} v_i(v_j - v_i)f_k\, d(v_1,...,v_k) = \frac{1}{k^2}\sum_{i=1}^{k}\sum_{j=1}^{k}\int_{\mathbb{R}^k}(v_i - v_j)^2 f_k\, d(v_1,...,v_k)\\ &= \frac{k-1}{k}\int_{\mathbb{R}^k}(v_1 - v_2)^2 f_k\, d(v_1,...,v_k) =: \frac{k-1}{k}\widetilde{V}_k\,.\end{aligned}$$

The contributions from coagulation and fragmentation are as in (2.5). Therefore

$$\dot{E}_k = \varphi_k(\{E_j\}_{j\geq1},\{M_j\}_{j\geq1}) - \frac{k-1}{k}\widetilde{V}_k\,, \qquad k\geq1\,,$$

with the definition $\widetilde{V}_1 := 0$.

As we have seen for the zeroth and first order moments, it turns out that the moments of any order solve a closed ODE system, recursively depending on the lower order moments. All second order moments can be represented by E_k and $\widetilde{V}_k$. The time derivative of $\widetilde{V}_k$ is given by

$$\begin{aligned}\dot{\widetilde{V}}_k =& \frac{1}{2}\sum_{j=1}^{k-1}\lambda_{j,k-j}\left(\left(1 - \frac{2j(k-j)}{k(k-1)}\right)\widetilde{V}_j M_{k-j} + \frac{2j(k-j)}{k(k-1)}2\left(E_j M_{k-j} - I_j I_{k-j}\right)\right)\\ &- \sum_{j=1}^{\infty}\lambda_{j,k}\widetilde{V}_k M_j + \sum_{j=1}^{\infty}\mu_{k,j}\widetilde{V}_{k+j} - \frac{1}{2}\sum_{j=1}^{k-1}\mu_{j,k-j}\widetilde{V}_k - 2\widetilde{V}_k\,, \qquad k>1\,,\end{aligned}$$

where in the first line the coefficients $1-\frac{2j(k-j)}{k(k-1)}$ and $\frac{2j(k-j)}{k(k-1)}$ are the probabilities that, after splitting $\{v_1,\dots,v_k\}$ into groups of sizes j and $k-j$, both v_1 and v_2 end up in the same subgroup and, respectively, in different ones. The last term results from the discussion process.

Finally, we compute the time derivative of the variance:

$$\dot{V} = \sum_{k=1}^{\infty} k\dot{E}_k = -\sum_{k=2}^{\infty}(k-1)\widetilde{V}_k \leq 0\,.$$

This allows the formal conclusion that asymptotically agreement is reached within each discussion group, which completes a heuristic argument for the conjecture

$$f_k(v_1,\dots,v_k,t) \to M_k^{\infty}\prod_{j=1}^{k}\delta(v_j - v_\infty) \qquad \text{as } t\to\infty\,, \qquad k\geq 1\,,$$

if (2.3) has a detailed-balance equilibrium.

Fast collision regime and first order non-instantaneous approximation

We rescale equation (2.1) in such a way that collisions are short, which requires a large fragmentation rate. For the discussions to still have a significant effect, we also need strong interaction fields. As a consequence we also expect that larger discussion groups become less likely. This motivates the rescalings

$$\mu_{i,j} \to \varepsilon^{-1}\mu_{i,j}\,, \qquad U_k \to \varepsilon^{-1}U_k\,, \qquad f_k \to \varepsilon^{k-1}f_k\,, \tag{2.6}$$

with $\varepsilon \ll 1$. This changes (2.1) into

$$\begin{aligned}\varepsilon\partial_t f_k + \nabla_{(v_1,\dots,v_k)}\cdot(U_k\, f_k) =& \frac{1}{2}\sum_{j=1}^{k-1}\lambda_{j,k-j} f_j \odot f_{k-j} - \sum_{j=1}^{\infty}\varepsilon^j\lambda_{j,k} f_k \int_{\mathbb{R}^j} f_j^*\, d(v_1^*,\dots,v_j^*)\\ &+\sum_{j=1}^{\infty}\varepsilon^j\mu_{k,j}\int_{\mathbb{R}^j} f_{k+j}\, d(v_{k+1},\dots,v_{k+j}) - \frac{1}{2}\sum_{j=1}^{k-1}\mu_{j,k-j} f_k\,.\end{aligned} \tag{2.7}$$

All these equations have fast dynamics, except for $k=1$, where the $O(1)$-terms vanish and the equation can be divided by ε:

$$\partial_t f_1 = \sum_{j=1}^{\infty}\varepsilon^{j-1}\mu_{1,j}\int_{\mathbb{R}^j} f_{j+1}\, d(v_2,\dots,v_{j+1}) - \sum_{j=1}^{\infty}\varepsilon^{j-1}\lambda_{j,1} f_1\int_{\mathbb{R}^j} f_j^*\, d(v_1^*,\dots,v_j^*) \tag{2.8}$$

The ensemble of free individuals can gain only from fragmentation and lose only by coagulation.

The instantaneous limit $\varepsilon\to 0$ is the same as in [80], but we also include its discussion here for the sake of self consistency. The limiting equations for $k=1$ and $k=2$ are a closed system:

$$\begin{aligned}\partial_t f_1 &= \mu_{1,1}\int_{\mathbb{R}} f_2\, dv_2 - \lambda_{1,1} f_1\int_{\mathbb{R}} f_1^*\, dv_1^*\,,\\ \nabla_{(v_1,v_2)}\cdot(U_2\, f_2) &= \frac{1}{2}\lambda_{1,1} f_1\otimes f_1 - \frac{1}{2}\mu_{1,1} f_2\end{aligned} \tag{2.9}$$

This system can be reduced to an equation for f_1 after solving the second equation for f_2 by the method of characteristics:

$$f_2 = \frac{\lambda_{1,1}}{2} \int_0^\infty S_{2,0}(\sigma)(f_1 \otimes f_1) d\sigma \,, \tag{2.10}$$

with the semigroup

$$(S_{2,0}(\sigma)h)(v_1, v_2) = e^{(1-\mu_{1,1}/2)\sigma} h(v_1', v_2') \tag{2.11}$$

generated by $f_2 \mapsto -\nabla_{(v_1,v_2)} \cdot (U_2\, f_2) - \frac{1}{2}\mu_{1,1} f_2$, and with the *collision rule*

$$\begin{aligned} v_1' = \Phi_{2,1}^{-\sigma}(v_1, v_2) &:= \frac{1+e^\sigma}{2} v_1 + \frac{1-e^\sigma}{2} v_2 \,, \\ v_2' = \Phi_{2,2}^{-\sigma}(v_1, v_2) &:= \frac{1-e^\sigma}{2} v_1 + \frac{1+e^\sigma}{2} v_2 \,, \end{aligned} \tag{2.12}$$

connecting the opinions (v_1', v_2') at the beginning of a discussion between two individuals to the opinions (v_1, v_2) at the end of a discussion of duration σ. This relation can be inverted by changing the sign of σ:

$$v_1 = \Phi_{2,1}^{\sigma}(v_1', v_2') \,, \qquad v_2 = \Phi_{2,2}^{\sigma}(v_1', v_2') \,.$$

Substitution of f_2 in the equation for f_1 results in a kinetic model for binary collisions of standard form:

$$\partial_t f_1 = \lambda_{1,1} \int_{\mathbb{R}} \int_0^\infty b(\sigma) \Big(e^\sigma (f_1 \otimes f_1)' - f_1 \otimes f_1 \Big) d\sigma \, dv_2 \,, \tag{2.13}$$

with the probability density

$$b(\sigma) = \frac{\mu_{1,1}}{2} e^{-\sigma \mu_{1,1}/2}$$

for the collision duration, with the determinant e^σ of the Jacobian of the collision rule, and with the prime denoting evaluation at the pre-collisional state (v_1', v_2').

The solution of (2.13) approximates the solution component f_1 of (2.7) formally up to a $O(\varepsilon)$-error. It is our goal to improve this approximation by one order in ε. Since in (2.8) f_2 occurs at leading order, we also need to approximate f_2 up to $O(\varepsilon)$. In both equations for f_1 and f_2, the component f_3 appears in $O(\varepsilon)$-terms. Therefore we need a leading order approximation for f_3. Since in the equation for f_3 components f_k, $k > 3$, do not occur at leading order, the first step in the approximation procedure is to ignore discussions with more than 3 participants, i.e. $\lambda_{j,k} = \mu_{j,k} = 0$, $j + k > 3$:

$$\partial_t f_1 = \mu_{1,1} \int_{\mathbb{R}} f_2 \, dv_2 + \varepsilon \, \mu_{1,2} \int_{\mathbb{R}^2} f_3 \, d(v_2, v_3) - \lambda_{1,1} f_1 \int_{\mathbb{R}} f_1^* \, dv_1^* - \varepsilon \lambda_{1,2} f_1 \int_{\mathbb{R}^2} f_2^* \, d(v_1^*, dv_2^*) \,, \tag{2.14a}$$

$$\varepsilon \partial_t f_2 + \nabla_{(v_1,v_2)} \cdot (U_2\, f_2) = \frac{1}{2} \lambda_{1,1} f_1 \otimes f_1 - \varepsilon \lambda_{1,2} f_2 \int_{\mathbb{R}} f_1^* \, dv_1^* + \varepsilon \mu_{1,2} \int_{\mathbb{R}} f_3 \, dv_3 - \frac{1}{2} \mu_{1,1} f_2 \,, \tag{2.14b}$$

$$\varepsilon \partial_t f_3 + \nabla_{(v_1,v_2,v_3)} \cdot (U_3\, f_3) = \lambda_{1,2} f_1 \odot f_2 - \mu_{1,2} f_3 \,, \tag{2.14c}$$

Since we only need a leading order approximation of f_3, the final approximation step is to consider the quasi-stationary version

$$\nabla_{(v_1,v_2,v_3)} \cdot (U_3\, f_3) = \lambda_{1,2} f_1 \odot f_2 - \mu_{1,2} f_3\,, \tag{2.15}$$

of (2.14c) and to eliminate f_3:

$$f_3 = \lambda_{1,2} \int_0^\infty S_3(\sigma)(f_1 \odot f_2) d\sigma\,,$$

where

$$(S_3(\sigma)h)(v_1, v_2, v_3) = e^{(2-\mu_{1,2})\sigma} h(v_1', v_2', v_3')$$

is the semigroup generated by $f_3 \mapsto -\nabla_{(v_1,v_2,v_3)} \cdot (U_3\, f_3) - \mu_{1,2} f_3$ with the *three-particle collision rule*

$$\begin{aligned} v_1' &= \Phi_{3,1}^{-\sigma}(v_1, v_2, v_3) := \frac{1+2e^\sigma}{3} v_1 + \frac{1-e^\sigma}{3} v_2 + \frac{1-e^\sigma}{3} v_3\,, \\ v_2' &= \Phi_{3,2}^{-\sigma}(v_1, v_2, v_3) := \frac{1-e^\sigma}{3} v_1 + \frac{1+2e^\sigma}{3} v_2 + \frac{1-e^\sigma}{3} v_3\,, \\ v_3' &= \Phi_{3,3}^{-\sigma}(v_1, v_2, v_3) := \frac{1-e^\sigma}{3} v_1 + \frac{1-e^\sigma}{3} v_2 + \frac{1+2e^\sigma}{3} v_3\,. \end{aligned} \tag{2.16}$$

Finally we obtain a model, which is accurate up to $O(\varepsilon)$ for both f_1 and f_2:

$$\begin{aligned} \partial_t f_1 =& \mu_{1,1} \int_{\mathbb{R}} f_2\, dv_2 + \varepsilon \mu_{1,2} \lambda_{1,2} \int_{\mathbb{R}^2} \int_0^\infty S_3(\sigma)\, (f_1 \odot f_2)\, d\sigma\, d(v_2, v_3) \\ & - \lambda_{1,1} f_1 \int_{\mathbb{R}} f_1^*\, dv_1^* - \varepsilon \lambda_{1,2} f_1 \int_{\mathbb{R}^2} f_2^*\, d(v_1^*, v_2^*)\,, \end{aligned} \tag{2.17a}$$

$$\begin{aligned} \varepsilon \partial_t f_2 + \nabla_{(v_1,v_2)} \cdot (U_2 f_2) =& \frac{1}{2} \lambda_{1,1} f_1 \otimes f_1 - \varepsilon \lambda_{1,2} f_2 \int_{\mathbb{R}} f_1^*\, dv_1^* \\ & + \varepsilon \mu_{1,2} \lambda_{1,2} \int_{\mathbb{R}} \int_0^\infty S_3(\sigma)\, (f_1 \odot f_2)\, d\sigma\, dv_3 - \frac{1}{2} \mu_{1,1} f_2\,, \end{aligned} \tag{2.17b}$$

which will be considered below subject to initial conditions

$$f_1(v_1, 0) = f_1^I(v_1)\,, \qquad f_2(v_1, v_2, 0) = f_2^I(v_1, v_2)\,, \tag{2.17c}$$

with the initial data satisfying

$$f_1^I,\, f_2^I \geq 0\,, \quad \int_{\mathbb{R}} \left(1+v_1^2\right) f_1^I\, dv_1 < \infty\,, \quad \int_{\mathbb{R}} \left(1+v_1^2\right) f_2^I\, dv_1\, dv_2 < \infty\,, \quad f_2^I(v_1, v_2) = f_2^I(v_2, v_1). \tag{2.18}$$

3 Well-posedness and instantaneous limit for the first order accurate model

This Section 3 is dedicated to an investigation of model (2.17). It contains results on the long-term dynamics of moments (Subsection 3.1), on existence and uniqueness of solutions (Subsection 3.2), and on the rigorous instantaneous limit (Subsection 3.3).

3.1 Dynamics of the moments

We start by deriving formal properties similarly to Section 2. We expect that (2.17) conserves the total mass

$$M := M_1 + 2\varepsilon M_2\,, \qquad \text{where} \quad M_1 := \int_{\mathbb{R}} f_1\, dv_1\,, \quad M_2 := \int_{\mathbb{R}^2} f_2\, d(v_1, v_2)\,. \tag{2.19}$$

Note that there is no contribution from f_3, since discussions with 3 participants have vanishing duration by (2.15), which also implies $\mu_{1,2}M_3 = \lambda_{1,2}M_1M_2$. Therefore the partial masses M_1, M_2, satisfy the ODE system

$$\begin{aligned} \dot{M}_1 =& \mu_{1,1}M_2 - \lambda_{1,1}M_1^2\,, \\ 2\varepsilon\dot{M}_2 =& \lambda_{1,1}M_1^2 - \mu_{1,1}M_2\,, \end{aligned} \tag{2.20}$$

immediately implying the mass conservation

$$M = M_1(0) + 2\varepsilon M_2(0)\,,$$

which can be used to establish convergence $(M_1(t), M_2(t)) \to (M_1^\infty, M_2^\infty)$ as $t \to \infty$, with

$$M_1^\infty = \frac{2M}{1 + \sqrt{1 + 8\lambda_{1,1}\varepsilon M/\mu_{1,1}}}\,, \qquad M_2^\infty = \frac{\lambda_{1,1}}{\mu_{11}}(M_1^\infty)^2\,. \tag{2.21}$$

The same is expected for the total first moment of the system

$$I := I_1 + 2\varepsilon I_2\,, \qquad \text{where} \quad I_1 := \int_{\mathbb{R}} v_1\, f_1\, dv_1\,, \quad I_2 := \int_{\mathbb{R}^2} v_1\, f_2\, d(v_1, v_2)\,, \tag{2.22}$$

where the partial first moments again satisfy a closed ODE system:

$$\dot{I}_1 = -2\varepsilon\dot{I}_2 = \mu_{1,1}\, I_2 - \lambda_{1,1}\, M_1\, I_1 + \frac{2}{3}\varepsilon\lambda_{1,2}\,(M_1 I_2 - M_2 I_1)\,, \tag{2.23}$$

where we have again used (2.15) to get $\mu_{1,2}I_3 = \lambda_{1,2}(I_1M_2 + 2I_2M_1)/3$. as expected, the first moment is conserved: $I = I_1(0) + 2\varepsilon I_2(0)$. Using this for reduction to a scalar equation as well as the convergence of the partial masses, it is obvious that

$$\begin{aligned} I_1(t) \;&\to\; I_1^\infty := \frac{3\mu_{1,1} + 2\varepsilon\lambda_{1,2}M_1^\infty}{3\mu_{11} + 2\varepsilon(3\lambda_{1,1}M_1^\infty + \lambda_{1,2}M)} I = M_1^\infty v_\infty\,, \\ I_2(t) \;&\to\; I_2^\infty := \frac{3\lambda_{1,1}M_1^\infty + 2\varepsilon\lambda_{1,2}M_2^\infty}{3\mu_{1,1} + 2\varepsilon\lambda_{1,2}M_1^\infty} I_1^\infty = M_2^\infty v_\infty\,, \end{aligned}$$

as $t \to \infty$, with $v_\infty := I/M$, which is independent of time.

Analogously to the previous section, we define the total variance $V := V_1 + 2\varepsilon V_2$, where

$$V_k = \int_{\mathbb{R}^k} (v_1 - v_\infty)^2 f_k\, d(v_1, \ldots, v_k)\,, \qquad k = 1, 2, 3\,.$$

The partial variances satisfy the ODEs

$$\begin{aligned} \dot{V}_1 &= \mu_{1,1}V_2 + \varepsilon\mu_{1,2}V_3 - \lambda_{1,1}\, M_1\, V_1 - \varepsilon\lambda_{1,2}M_2\, V_1\,, \\ 2\varepsilon\dot{V}_2 &= \lambda_{1,1}M_1V_1 + 2\varepsilon\mu_{1,2}V_3 - 2\varepsilon\lambda_{1,2}M_1V_2 - \mu_{1,1}V_2 - 4\widetilde{V}_2\,, \end{aligned} \tag{2.24}$$

with

$$\widetilde{V}_k = \int_{\mathbb{R}^k} (v_1 - v_2)^2 f_k \, d(v_1, \ldots, v_k)\,, \qquad k = 2, 3\,.$$

An equation for V_3 is obtained from (2.15), after using the computation

$$\begin{aligned} &\int_{\mathbb{R}^3} (v_1 - v_\infty)^2 \nabla_{(v_1,v_2,v_3)} \cdot (U_3 f_3) d(v_1, v_2, v_3) = -\frac{2}{3}\int_{\mathbb{R}^3} v_1(v_2 - v_1 + v_3 - v_1) f_3 d(v_1, v_2, v_3) \\ &= -\frac{4}{3}\int_{\mathbb{R}^3} v_1(v_2 - v_1) f_3 d(v_1, v_2, v_3) = \frac{2}{3}\widetilde{V}_3\,, \end{aligned}$$

where the last equality follows from symmetrization. This implies

$$\mu_{1,2}V_3 = \frac{\lambda_{1,2}}{3}(V_1M_2 + 2V_2M_1) - \frac{2}{3}\widetilde{V}_3\,. \tag{2.25}$$

We conclude that the variance is nonincreasing:

$$\dot{V} = -4\widetilde{V}_2 - 2\widetilde{V}_3 \leq 0\,. \tag{2.26}$$

Further information can be derived from an equation for $\widetilde{V}_3$, also obtained from (2.15):

$$\mu_{1,2}\widetilde{V}_3 = \frac{\lambda_{1,2}}{3}(2V_1M_2 + 2V_2M_1 - 4(I_1 - v_\infty M_1)(I_2 - v_\infty M_2) + M_1\widetilde{V}_2)\,,$$

implying

$$\dot{V} \leq -\frac{4\lambda_{1,2}}{3\mu_{1,2}}(V_1M_2 + V_2M_1) + \frac{8\lambda_{1,2}}{3\mu_{1,2}}(I_1 - v_\infty M_1)(I_2 - v_\infty M_2)\,.$$

By our previous results, M_1 and M_2 converge to positive values as $t \to \infty$, and the last term converges to zero. Therefore for t large enough there exists $\gamma > 0$, such that

$$\dot{V} \leq -\gamma V + \frac{8\lambda_{1,2}}{3\mu_{1,2}}(I_1 - v_\infty M_1)(I_2 - v_\infty M_2)\,,$$

implying $V(t) \to 0$ as $t \to \infty$ and thus, at least formally,

$$f_1(v_1, t) \to M_1^\infty \delta(v_1 - v_\infty)\,, \qquad f_2(v_1, v_2, t) \to M_2^\infty \delta(v_1 - v_\infty)\delta(v_2 - v_\infty)\,, \qquad \text{as } t \to \infty\,.$$

3.2 Existence and uniqueness

We start by stating the *mild formulation* of the initial value problem (2.17), which can be obtained by integration of the system with respect to time

$$\begin{aligned} f_1(t) = {} & S_1(0,t) f_1^I + \mu_{1,1} \int_0^t S_1(s,t) \int_{\mathbb{R}} f_2(s)\, dv_2\, ds \\ & + \varepsilon \mu_{1,2} \lambda_{1,2} \int_0^t S_1(s,t) \int_{\mathbb{R}^2} \int_0^\infty S_3(\sigma)\, (f_1(s) \odot f_2(s))\, d\sigma\, d(v_2, v_3)\, ds\,, \end{aligned} \tag{2.27a}$$

$$\begin{aligned} f_2(t) = {} & S_{2,\varepsilon}\left(0, \frac{t}{\varepsilon}\right) f_2^I + \frac{\lambda_{1,1}}{2\varepsilon} \int_0^t S_{2,\varepsilon}\left(\frac{s}{\varepsilon}, \frac{t}{\varepsilon}\right) (f_1(s) \otimes f_1(s)) ds \\ & + \mu_{1,2} \lambda_{1,2} \int_0^t S_{2,\varepsilon}\left(\frac{s}{\varepsilon}, \frac{t}{\varepsilon}\right) \int_{\mathbb{R}} \int_0^\infty S_3(\sigma)\, (f_1(s) \odot f_2(s))\, d\sigma\, dv_3\, ds\,, \end{aligned} \tag{2.27b}$$

where we use the one-particle semigroup

$$S_1(s,t) := \exp\left(-\lambda_{1,1} \int_s^t M_1(r)\, dr - \varepsilon \lambda_{2,1} \int_s^t M_2(r)\, dr \right),$$

as well as the two-particle semigroup (written in terms of the fast variables $\sigma = s/\varepsilon$, $\tau = t/\varepsilon$)

$$\begin{aligned} & \Big(S_{2,\varepsilon}(\sigma,\tau) h \Big)(v_1, v_2) \\ & := \exp\left((1 - \mu_{1,1}/2)(\tau - \sigma) - \lambda_{1,2} \int_{\varepsilon\sigma}^{\varepsilon\tau} M_1(r)\, dr \right) h\left(\Phi_{2,1}^{\sigma-\tau}(v_1, v_2), \Phi_{2,2}^{\sigma-\tau}(v_1, v_2) \right), \end{aligned} \tag{2.28}$$

with the coordinate transformations as in (2.12). Note that the notation is consistent with the previous section in the sense that (2.11) is obtained with $\tau - \sigma$ replaced by σ and with $\varepsilon = 0$. The arguments v_1, v_2, v_3 are suppressed in (2.27) and in the following, whenever their choice is unambiguous.

Theorem 1. *Let $f_1^I \in L^1_+(\mathbb{R})$ and $f_2^I \in L^1_+(\mathbb{R}^2)$. Then (2.27) has a unique solution*

$$(f_1, f_2) \in C\left([0,\infty);\, L^1_+(\mathbb{R}) \times L^1_+(\mathbb{R}^2) \right).$$

Proof. Following our considerations regarding the moments in Section 3.1, M_1 and M_2 can be completely characterized by the dynamics of (2.20) and therefore can be assumed to be given in the definitions of S_1 and $S_{2,\varepsilon}$. It will be used in the following that the semigroups S_1, $S_{2,\varepsilon}$, and S_3 are L^1-contractions, since the factors $e^{\tau-\sigma}$ in $S_{2,\varepsilon}$ and $e^{2\sigma}$ in S_3 are the determinants of the Jacobians of the coordinate transformations $\Phi_2^{\sigma-\tau}$ and, respectively, $\Phi_3^{-\sigma}$.

Local existence and uniqueness will be proven by Picard iteration. The right hand-side of (2.27) defines the fixed-point operator $\mathcal{F}(f_1, f_2) = (\mathcal{F}_1(f_1, f_2), \mathcal{F}_2(f_1, f_2))$, which obviously preserves positivity and, by the contraction property of the semigroups, maps

$C([0,T];\, L^1_+(\mathbb{R}) \times L^1_+(\mathbb{R}^2))$ into itself for every $T > 0$. More precisely, with the natural norm $\|\cdot\|_{n,T}$ on $C([0,T];\, L^1_+(\mathbb{R}^n))$,

$$\begin{aligned} \|\mathcal{F}_1(f_1,f_2)\|_{1,T} &\leq M_1^I + T(\mu_{1,2}\|f_2\|_{2,T} + \varepsilon\lambda_{1,2}\|f_1\|_{1,T}\|f_2\|_{2,T})\,, \\ \|\mathcal{F}_2(f_1,f_2)\|_{2,T} &\leq M_2^I + T\left(\frac{\mu_{1,1}}{2\varepsilon}\|f_1\|_{1,T}^2 + \lambda_{1,2}\|f_1\|_{1,T}\|f_2\|_{2,T}\right), \end{aligned}$$

with $M_n^I := \int_{\mathbb{R}^n} f_n^I \, d(v_1,\dots,v_n)$. Here we have used that actually

$$\|S_3(\sigma)\|_{L^1(\mathbb{R}^3)\to L^1(\mathbb{R}^3)} \leq e^{-\mu_{1,2}\sigma}\,. \tag{2.29}$$

The above estimate implies immediately that, for T small enough, $\mathcal{F}$ maps the set

$$\mathcal{S} := \{(f_1,f_2) \in C([0,T];\, L^1_+(\mathbb{R}) \times L^1_+(\mathbb{R}^2)) :\, \|f_n\|_{n,T} \leq 2M_n^I,\, n = 1,2\}$$

into itself.

In order to show the contraction property of $\mathcal{F}$ we consider $(f_1,f_2), (\tilde f_1, \tilde f_2) \in \mathcal{S}$ and show Lipschitz continuity of the second and third terms on the right hand sides of (2.27a) and (2.27b). The first term is linear:

$$\mu_{1,1}\int_{\mathbb{R}}\left|\int_0^t S_1(s,t)\int_{\mathbb{R}}(f_2(s)-\tilde f_2(s))dv_2\,ds\right| dv_1 \leq T\mu_{1,1}\|f_2-\tilde f_2\|_{2,T}\,,$$

where we used that $S_1(s,t) \leq 1$. For the second term we again use (2.29):

$$\begin{aligned} &\varepsilon\mu_{1,2}\lambda_{1,2}\int_{\mathbb{R}}\left|\int_0^t S_1(s,t)\int_{\mathbb{R}^2}\int_0^\infty S_3(\sigma)\Big(f_1(s)\odot f_2(s) - \tilde f_1(s)\odot\tilde f_2(s)\Big)d\sigma\, d(v_2,v_3)ds\right| dv_1 \\ &\leq \varepsilon\lambda_{1,2}\int_0^t\int_{\mathbb{R}^3}\Big|f_1(s)\odot f_2(s) - \tilde f_1(s)\odot\tilde f_2(s)\Big|\, d(v_1,v_2,v_3)ds \\ &\leq \varepsilon\lambda_{1,2}\int_0^t\int_{\mathbb{R}^3}\Big(\Big|f_1(s)-\tilde f_1(s)\Big|\odot f_2(s) - \Big|f_2(s)-\tilde f_2(s)\Big|\odot\tilde f_1(s)\Big)\, d(v_1,v_2,v_3)ds \\ &\leq T\varepsilon\lambda_{1,2}\Big(2M_2^I\|f_1-\tilde f_1\|_{1,T} + 2M_1^I\|f_2-\tilde f_2\|_{2,T)}\Big)\,. \end{aligned}$$

Similar estimates can be carried for the right hand side of (2.27b). Indeed, we have

$$\begin{aligned} &\frac{\lambda_{1,1}}{2\varepsilon}\int_{\mathbb{R}^2}\left|\int_0^t S_2\left(\frac{s}{\varepsilon},\frac{t}{\varepsilon}\right)\Big(f_1(s)\otimes f_1(s) - \tilde f_1(s)\otimes\tilde f_1(s)\Big)\,ds\right| d(v_1,v_2) \\ &\leq T\frac{\lambda_{1,1}}{\varepsilon}2M_1^I\|f_1-\tilde f_1\|_{1,T}\,, \end{aligned}$$

and

$$\begin{aligned} &\mu_{2,1}\lambda_{1,2}\int_{\mathbb{R}^2}\left|\int_0^t S_2\left(\frac{s}{\varepsilon},\frac{t}{\varepsilon}\right)\int_{\mathbb{R}}\int_0^\infty S_3(\sigma)\Big(f_1(s)\odot f_2(s) - \tilde f_1(s)\odot\tilde f_2(s)\Big)\,d\sigma\, dv_3\, ds\right| d(v_1,v_2) \\ &\leq T\lambda_{1,2}\Big(2M_2^I\|f_1-\tilde f_1\|_{1,T} + 2M_1^I\|f_2-\tilde f_2\|_{2,T)}\Big)\,. \end{aligned}$$

These four estimates show that $\mathcal{F}$ is a contraction for T small enough, implying local existence and uniqueness.

Our procedure is consistent in the sense that, if (M_1, M_2) is a solution of (2.20) with $M_n(0) = M_n^I$, n=1,2, and (2.27) is solved with this (M_1, M_2) given in the definition of the semigroups, then $\int_{\mathbb{R}^n} f_n d(v_1, \dots, v_n) = M_n$, $n = 1, 2$. These remain bounded as a consequence of the convergence of $(M_1(t), M_2(t))$ to (M_1^∞, M_2^∞) as $t \to \infty$ (see (2.21)), which implies global existence. □

3.3 Instantaneous limit

The formal instantaneous limit $\varepsilon \to 0$ can be carried out in the same way as in Section 2. As an alternative one may start from (2.27b), carry out the coordinate change $s = t - \varepsilon\sigma$, and note that

$$S_{2,\varepsilon}\left(0, \frac{t}{\varepsilon}\right) \to 0\,, \qquad S_{2,\varepsilon}\left(\frac{t}{\varepsilon} - \sigma, \frac{t}{\varepsilon}\right) \to S_{2,0}(\sigma)\,, \qquad \text{as } \varepsilon \to 0\,.$$

Therefore (2.10) is the formal limit of (2.27b), and the formal limit of f_1 satisfies (2.13). The aim of this section is to make the limit rigorous.

Theorem 2. *Let the initial data satisfy* (2.18). *Then the solution* (f_1, f_2) *of* (2.17) *satisfies*

$$\lim_{\varepsilon\to 0} f_1(\cdot, t) = f_1^0(\cdot, t) \quad \textit{weakly in } L^1(\mathbb{R}), \textit{locally uniformly in } t \in [0, \infty),$$
$$\lim_{\varepsilon\to 0} f_2 = f_2^0 \quad \textit{tightly in } \mathbb{R}^2 \times (0, T), \textit{ for any } 0 < T < \infty\,,$$

where (f_1^0, f_2^0) *is a weak solution of* (2.9) *satisfying* $f_1^0(t = 0) = f_1^I$.

The proof of Theorem 2 is based on compactness arguments and will be given after two preliminary steps. First, uniform bounds (as $\varepsilon \to 0$) on the moments will be obtained, which gives compactness in the space of measures. An improvement for f_1 to L^1-compactness can be achieved in the second step by establishing a uniform bound on the logarithmic entropy.

Uniform moment bounds. The first goal is to obtain uniform-in-ε bounds for the moments, whose long time behaviour has been investigated in Section 3.1. We start with the system (2.20), which is singularly perturbed, since the small parameter multiplies the derivative of M_2, and the formal limit $\varepsilon \to 0$ reduces the differential order. The fact that the right hand side of the M_2-equation is linear in M_2 with a strictly negative derivative w.r.t. M_2 makes this system a classical case in singular perturbation theory.

The Tikhonov theorem (see e.g. [118], Theorem 8.1) states that the solution can be approximated uniformly in ε by the sum of a solution of the *reduced system* ($\varepsilon = 0$ in (2.20)) and of an *initial layer correction,* written in terms of the *fast variable* t/ε. Both contributions are bounded uniformly in ε, at least locally in time.

Combining this observation with the fact that the solution converges to a uniformly bounded limit as $t \to \infty$ implies uniform boundedness (as $\varepsilon \to 0$ and as $t \to \infty$) of M_1 and M_2. The same argument can be applied to system (2.23), showing that also I_1 and I_2 are uniformly bounded.

A uniform bound for the partial variance V_1 follows immediately, since the total variance is nonincreasing (2.26). For the second partial variance we use (2.24) and (2.25) to get

$$2\varepsilon \dot{V}_2 \leq \left(\lambda_{1,1} M_1 + \frac{2}{3}\varepsilon \lambda_{1,2} M_2\right) V_1 - \left(\mu_{1,1} + \frac{2}{3}\varepsilon \lambda_{1,2} M_1\right) V_2 \,,$$

implying uniform boundedness of V_2 by a comparison principle (explicitly solving the corresponding equation). Collecting these results we have:

Lemma 1. *Let the initial data satisfy* (2.18)*. Then the solution of* (2.27) *satisfies*

$$\int_{\mathbb{R}^n} (1 + v_1^2) f_n \, d(v_1, \ldots, v_n) < \infty \,, \qquad n = 1, 2,$$

uniformly as $\varepsilon \to 0$ *and* $t \to \infty$*.*

Logarithmic entropy. The leading order coagulation-fragmentation reactions in (2.17) have the equilibrium $\left(\bar{f}_1, \bar{f}_2\right) = (1, \lambda_{1,1}/\mu_{1,1})$. Motivated by the theory of chemical reaction networks [76], we investigate the corresponding logarithmic relative entropy

$$\mathcal{H}[f_1, f_2] := \int_{\mathbb{R}} f_1 \left(\log(f_1) - 1\right) \, dv_1 + \varepsilon \int_{\mathbb{R}^2} f_2 \left(\log\left(\frac{\mu_{1,1} f_2}{\lambda_{1,1}}\right) - 1\right) d(v_1, v_2) \,. \tag{2.30}$$

Along solutions of (2.17) we obtain

$$\begin{aligned} \frac{d}{dt}\mathcal{H}[f_1, f_2] = &- \frac{1}{2} \int_{\mathbb{R}^2} (\lambda_{1,1} f_1 \otimes f_1 - \mu_{1,1} f_2) \log\left(\frac{\lambda_{1,1} f_1 \otimes f_1}{\mu_{1,1} f_2}\right) d(v_1, v_2) \\ &+ \varepsilon \int_{\mathbb{R}^3} (\mu_{1,2} f_3 - \lambda_{1,2} f_1 \otimes f_2) \log\left(\frac{\mu_{1,1} f_1 \otimes f_2}{\lambda_{1,1}}\right) d(v_1, v_2, v_3) \\ &- \int_{\mathbb{R}^2} \nabla_{(v_1, v_2)} \cdot (U_2 f_2) \log\left(\frac{\mu_{1,1} f_2}{\lambda_{1,1}}\right) d(v_1, v_2) \,. \end{aligned}$$

The first term on the right hand side is the non-positive contribution from the leading order reactions, as expected. The last term, using two integrations by parts as well as $\nabla_{(v_1, v_2)} \cdot U_2 = -1$, can be computed as

$$- \int_{\mathbb{R}^2} \nabla_{(v_1, v_2)} \cdot (U_2 f_2) \log\left(\frac{\mu_{1,1} f_2}{\lambda_{1,1}}\right) d(v_1, v_2) = \int_{\mathbb{R}^2} U_2 \cdot \nabla_{(v_1, v_2)} f_2 \, d(v_1, v_2) = M_2 \,,$$

which is positive, but uniformly bounded. Finally, with the second term we produce a nonpositive contribution by subtracting and adding

$$\begin{aligned}
&\varepsilon \int_{\mathbb{R}^3} (\mu_{1,2} f_3 - \lambda_{1,2} f_1 \otimes f_2) \log\left(\frac{\mu_{1,1}\mu_{1,2} f_3}{\lambda_{1,1}\lambda_{1,2}}\right) d(v_1, v_2, v_3) \\
&= \varepsilon \int_{\mathbb{R}^3} (\mu_{1,2} f_3 - \lambda_{1,2} f_1 \odot f_2) \log\left(\frac{\mu_{1,1}\mu_{1,2} f_3}{\lambda_{1,1}\lambda_{1,2}}\right) d(v_1, v_2, v_3) \\
&= -\varepsilon \int_{\mathbb{R}^3} \nabla_{(v_1,v_2,v_3)} \cdot (U_3 f_3) \log\left(\frac{\mu_{1,1}\mu_{1,2} f_3}{\lambda_{1,1}\lambda_{1,2}}\right) d(v_1, v_2, v_3) \\
&= \varepsilon \int_{\mathbb{R}^3} U_3 \cdot \nabla_{(v_1,v_2,v_3)} f_3 \, d(v_1, v_2, v_3) = \varepsilon M_3 \,,
\end{aligned}$$

another positive but uniformly bounded contribution. For the second equality we have used (2.15). Combining these results, we have

$$\frac{d}{dt}\mathcal{H}[f_1, f_2] \leq M_2 + \varepsilon M_3 \,,$$

with the consequence

Lemma 2. *Let the assumptions of Lemma 1 hold and let* $0 < T < \infty$. *Then* $f_1 \log(f_1)$ *is bounded in* $L^\infty((0,T), L^1(\mathbb{R}))$ *uniformly as* $\varepsilon \to 0$.

Passing to the limit. The instantaneous limit will be based on the uniform bounds in Lemmas 1 and 2.

Proof of Theorem 2. Let $0 < T < \infty$. Then Lemma 1 implies that $\{f_1\}_\varepsilon$ and $\{f_2\}_\varepsilon$ are tight sets of measures on $\mathbb{R} \times (0,T)$ and, respectively, $\mathbb{R}^2 \times (0,T)$. Due to the Prokhorov theorem [104] this is equivalent to weak sequential compactness of $\{f_1\}_\varepsilon$ and $\{f_2\}_\varepsilon$ in the spaces of positive measures $\mathcal{M}^+(\mathbb{R} \times (0,T))$ and, respectively, $\mathcal{M}^+(\mathbb{R}^2 \times (0,T))$. The uniform tightness of f_1, together with the uniform entropy bound in Lemma 2, allow to apply the Dunford-Pettis criterion and to deduce weak sequential compactness of $\{f_1\}_\varepsilon$ in $L^1(\mathbb{R} \times (0,T))$. Additionally, from (2.17a) one can obtain the following L^1-bound on the time derivative of f_1:

$$\|\partial_t f_1\|_{L^1(\mathbb{R})} \leq \max\{\mu_{1,1} M_2, \lambda_{1,1} M_1^2\} + \varepsilon \lambda_{1,2} M_1 M_2 \,, \tag{2.31}$$

implying (by Lemma 1) uniform Lipschitz continuity of the map $t \mapsto f_1(\cdot, t)$ with respect to the $L^1(\mathbb{R})$-topology. Hence, we can deduce the existence of an accumulation point $f_1^0 \in C([0,\infty); L^1(\mathbb{R}))$ of the family $\{f_1\}_\varepsilon$, such that for a sequence $\varepsilon_n \to 0$, the sequence $\{f_1\}_{\varepsilon_n}$ converges to f_1^0 with respect to $L^1(\mathbb{R})$, locally uniformly in $t \in [0,\infty)$.

For the fast variable f_2 there is no uniform bound of the time derivative as for f_1. Therefore we only obtain tight convergence (up to subsequences).

Passing to the limit in (2.17) is straightforward, since the $O(\varepsilon)$-terms tend to zero by uniform boundedness, and the only leading order nonlinearity is $f_1 \otimes f_1$, where we use that weak convergence of two measures implies weak convergence of the product measure to the product measure of the limits ([14], Theorem 2.8 (ii)). Finally, the restriction to subsequences is not necessary, since uniqueness for the initial value problem for (2.13) can be shown analogously to the proof of Theorem 1. □

4 A first order accurate, non-instantaneous, scalar model

In Section 2 we derived system (2.17), describing a kinetic model including first order non-instantaneous correction terms for the interaction processes of the particles. This system promises to be a good candidate to model particle dynamics with close to instantaneous interactions, as the analysis in Section 3 shows. An obvious further question, matter of discussion in this section, is whether one can find a scalar equation, which gives a well-posed first order non-instantaneous approximation of the dynamics.

The basic idea will be to eliminate f_2 from (2.17). This is made feasible by the observation that in the first term on the second line of (2.17b), f_2 can be replaced by its formal limit as $\varepsilon \to 0$, since this will only introduce an $O(\varepsilon^2)$-error. The same argument could be used for the last term in the first line, but this would obstruct non-negativity of the approximation. Therefore we start from the mild formulation (2.27b), where we introduce the coordinate transformation $s = t - \varepsilon\sigma$:

$$\begin{aligned} f_2(t) = {} & S_{2,\varepsilon}\left(0, \frac{t}{\varepsilon}\right) f_2^I + \frac{\lambda_{1,1}}{2} \int_0^{t/\varepsilon} S_{2,\varepsilon}\left(\frac{t}{\varepsilon} - \sigma, \frac{t}{\varepsilon}\right) (f_1(t-\varepsilon\sigma) \otimes f_1(t-\varepsilon\sigma)) d\sigma \\ & + \varepsilon\mu_{1,2}\lambda_{1,2} \int_0^{t/\varepsilon} S_{2,\varepsilon}\left(\frac{t}{\varepsilon} - \sigma, \frac{t}{\varepsilon}\right) \int_{\mathbb{R}} \int_0^{\infty} S_3(\rho) \left(f_1(t-\varepsilon\sigma) \odot f_2(t-\varepsilon\sigma)\right) d\rho\, dv_3\, d\sigma\,. \end{aligned} \tag{2.32}$$

The right hand side will be approximated by dropping the first term, since it is exponentially small away from $t = 0$, and by passing to the limit in the coefficient of ε in the second line:

$$\begin{aligned} f_{2,as}(t) = {} & f_{2,1}(t) + \varepsilon f_{2,2}(t) \\ := {} & \frac{\lambda_{1,1}}{2} \int_0^{t/\varepsilon} \exp\left(-\lambda_{1,2} \int_{t-\varepsilon\sigma}^{t} M_1(s) ds\right) S_{2,0}(\sigma)(f_1(t-\varepsilon\sigma) \otimes f_1(t-\varepsilon\sigma)) d\sigma \\ & + \varepsilon\mu_{1,2}\lambda_{1,2} \int_0^{\infty} S_{2,0}(\sigma) \int_{\mathbb{R}} \int_0^{\infty} S_3(\rho) \left(f_1(t) \odot f_2^0(t)\right) d\rho\, dv_3\, d\sigma\,, \end{aligned} \tag{2.33}$$

with

$$f_2^0(t) = \frac{\lambda_{1,1}}{2} \int_0^{\infty} S_{2,0}(\sigma)(f_1(t) \otimes f_1(t)) d\sigma\,.$$

Note that (2.33) is a formal approximation of f_2 with an $O(\varepsilon^2)$-error, given explicitly in terms of f_1. Now these approximations are used in (2.17a) ($f_{2,as}$ in the leading order terms and f_2^0 in the $O(\varepsilon)$-terms):

$$\partial_t f_1 = Q_2(f_1, f_1) + \varepsilon Q_3(f_1, f_1, f_1)\,, \tag{2.34}$$

with

$$Q_2(f_1, f_1) = \lambda_{1,1} \int_{\mathbb{R}} \left[\frac{\mu_{11}}{2} \int_0^{t/\varepsilon} \exp\left(-\lambda_{1,2} \int_{t-\varepsilon\sigma}^{t} M_1(s) ds \right) \right.$$
$$\left. S_{2,0}(\sigma)(f_1(t-\varepsilon\sigma) \otimes f_1(t-\varepsilon\sigma)) d\sigma - f_1 \otimes f_1 \right] dv_2$$

and

$$Q_3(f_1, f_1, f_1) = \lambda_{1,2} \int_{\mathbb{R}^2} \left[\mu_{1,2} \left(1 + \mu_{1,1} \int_0^\infty S_{2,0}(\sigma) d\sigma \right) \int_0^\infty S_3(\rho)(f_1 \odot f_2^0) d\rho - f_1 \otimes f_2^0 \right] d(v_2, v_3)\,.$$

In the binary collision operator Q_2 collisions are non-instantaneous, causing delays in the gain term, as already observed in [80]. The ternary collision operator Q_3 is an instantaneous approximation. Taking into account non-instantaneous effects from the full model would only create $O(\varepsilon^2)$-corrections. The gain term of Q_3 involves iterated applications of the two-particle and three-particle semigroups, since a ternary collision requires a predecessing binary collision to happen. This structure is somewhat reminiscent of the Wild sum representation [125] of solutions of the Boltzmann equation, which has been related to iterated higher order collisions, e.g., by Villani [121]. However, different from that our semigroups also contain an account of the dynamics during collisions.

Model (2.34) preserves non-negativity of f_1. However, it does not conserve mass, which is no surprise because f_1 does not represent the particles involved in non-instantaneous binary collisions. This has also been observed in models for non-instantaneous collisions of quantum particles [85], where an auxiliary *correlated density* is introduced as a correction. In the following it will be shown that the one-particle marginal of $2\varepsilon f_{2,1}$ in (2.33) is a good approximation for the correlated density. Note that the contributions to $f_{2,as}$ satisfy the equations

$$\begin{aligned}
\varepsilon \partial_t f_{2,1} + \nabla_{(v_1,v_2)}(U_2 f_{2,1}) &= \frac{\lambda_{1,1}}{2} f_1 \otimes f_1 - \left(\frac{\mu_{1,1}}{2} + \varepsilon \lambda_{1,2} M_1 \right) f_{2,1}\,, \\
\nabla_{(v_1,v_2)}(U_2 f_{2,2}) &= \mu_{1,2} \int_{\mathbb{R}} f_3 \, dv_3 - \frac{\mu_{1,1}}{2} f_{2,2}\,, \qquad \text{with} \\
\nabla_{(v_1,v_2,v_3)}(U_3 f_3) &= \lambda_{1,2} f_1 \odot f_2^0 - \mu_{1,2} f_3\,,
\end{aligned}$$

implying

$$\begin{aligned}
\varepsilon \dot{M}_{2,1} &= \frac{\lambda_{1,1}}{2} M_1^2 - \left(\frac{\mu_{1,1}}{2} + \varepsilon \lambda_{1,2} M_1 \right) M_{2,1}\,, \\
\frac{\mu_{1,1}}{2} M_{2,2} &= \mu_{1,2} M_3 = \lambda_{1,2} M_1 M_2^0\,.
\end{aligned}$$

These and integration of (2.34) give

$$\frac{d}{dt}\left(M_1 + 2\varepsilon M_{2,1}\right) = 2\varepsilon\lambda_{1,2}M_1\left(M_2^0 - M_{2,1}\right) = O(\varepsilon^2)\,,$$

which is the desired result up to an $O(\varepsilon^2)$-error.

Chapter 3

Steady states of Transport-Coagulation-Nucleation models

Joint work with J. Delacour, M. Doumic and C. Schmeiser

The main result of this work is existence of steady states of a boundary value problem for a integro-differential equations modeling the dynamics of a size distribution function of polymers. The model describes the growth (polymerization) of small polymers created by nucleation, the shrinkage (depolymerization) of large polymers, and the coagulation of pairs of polymers. Growth and shrinkage is described by transport, the nucleation rate by a boundary condition, and coagulation by a stochastic jump process. Apart from the existence result, qualitative properties of steady states are illustrated both by explicit examples and by numerical experiments. The explicit results relate the growth behavior of the transport velocity and of the coagulation kernel to decay properties of steady states.

Contents

1 Introduction 72

2 The choice of the transport velocity 73

3 The inverse problem – explicit examples of steady state solutions 75

4 Existence and properties of steady states 77

4.1 Qualitative properties of steady states 81

5 Numerical results 82

5.1 Comparison with exact solutions 83

5.2 Behavior of the numerical solution close to x_0 84

1 Introduction

Coagulation equations constitute a fundamental class of integro-differential equations that describe the evolution of size-distributed particle systems undergoing binary aggregation. These models have been widely applied across the physical sciences, particularly in the context of aerosol dynamics [49], where the interaction and aggregation of gas particles or droplets are governed by collision mechanisms encoded in a coagulation kernel [56], [108]. In the biological sciences, coagulation-type equations have been employed to model processes such as the polymerization of macromolecules [127]. Given these numerous applications, coagulation equations – and more generally, coagulation-fragmentation equations (see, e.g., [10], [9] for comprehensive references on the topic) – have been extensively studied from both analytical and numerical perspectives. In contrast, coagulation equations incorporating a transport term in the size variable have received significantly less attention, despite their relevance in modeling systems where particles grow or shrink continuously in addition to coalescence. Such transport term, analogous to those used in structured population models such as the McKendrick-von Foerster equation [2], [101], may arise naturally in contexts where aggregates self-grow by surface accretion or shrink through degradation. An example and motivation for this work is the formation of protein aggregates in cells as a preparation for their recycling by autophagy [44].

We are concerned with the existence of steady state solutions of the following coagulation-transport-nucleation model:

$$\begin{aligned} \partial_t f(x,t) + \partial_x\Big(v(x)f(x,t)\Big) = \; & \tfrac{1}{2}\int_0^x K(x-y,y)f(x-y,t)f(y,t)dy \\ & - \int_0^\infty K(x,y)f(y,t)f(x,t)dy\,, \\ f(0,t) = f_0\,, & \end{aligned} \tag{3.1}$$

where $f(x,t)$ is the particle size distribution function at time $t \geq 0$, with particle size $x \in [0,\infty)$. The function $v(x) \in C^1(0,\infty)$ represents the size-dependent transport velocity (the particle growth or shrinkage rate) and $K(x,y)$ is a symmetric coagulation kernel describing the coagulation rate between particles of size x and y. The boundary condition $f(0,t) = f_0 > 0$ models nucleation, i.e. the continuous injection of monomeric units into the system, as observed in biological contexts such as protein synthesis, cell renewal, or polymer production. It only makes sense if small polymers are not decomposed immediately, i.e. if $v(x) > 0$ close to $x = 0$.

The problem of the existence of steady-state solutions has been extensively tackled in the context of coagulation-fragmentation equations. When both coagulation and fragmentation processes are present, the dynamics are reversible, and detailed balance conditions can often be written explicitly (see, e.g., Section 2.3.3 of [10]). In contrast,

when only coagulation or only fragmentation occurs, one might intuitively expect that no non-trivial steady states can exist, due to the inherently irreversible nature of these dynamics. Surprisingly, this intuition fails in certain cases: exact steady-state solutions have been constructed for specific classes of coagulation and multiple-fragmentation kernels, as shown in [51]. In a related direction, the existence and characterization of steady states have also been investigated for transport-fragmentation models, notably in [48], where the eigenelements of the associated eigenproblem are used to analyze the long-time behaviour of the system. Furthermore, the existence of stationary non-equilibrium solutions has been established in [54] for coagulation equations – both in the discrete and continuous setting – including a source term representing the continuous injection of small-sized particles. This scenario shares structural similarities with our setting, where the boundary condition at zero models the persistent input of monomeric units.

The aim of this work is to identify conditions on the transport velocity, under which (3.1) admits non-trivial steady-state profiles in the case of the multiplicative coagulation kernel $K(x, y) = xy$. We shall see in the following section that this is not the case for an everywhere positive transport velocity, since this leads to gelation in finite time. Therefore it will be assumed that large polymers tend to shrink, i.e. the transport velocity $v(x)$ is negative for large x. In Section 3 the inverse problem of prescribing a steady state solution and determining corresponding transport velocities will be considered. Several explicit solutions will serve as illustrations. Section 4 contains an existence result for steady states. The main assumption is that the transport velocity is not only negative for large x, but tends to $-\infty$ fast enough as $x \to \infty$. Some qualitative properties of steady states are discussed formally, in particular the fact that there can be a singularity at the zero of the transport velocity. Finally, our results are illustrated by numerical experiments in Section 5.

2 The choice of the transport velocity

We start this section by deriving explicit information on the solution of (3.1) for the constant positive transport velocity $v \equiv 1$. In this case both transport and coagulation increase the polymer size, and therefore convergence to a steady state cannot be expected. However the solution behavior also depends on the coagulation rate.

Constant transport velocity and constant coagulation rate. For $v \equiv K \equiv 1$ we can derive the closed system of ODEs

$$\dot{M}_0 = f_0 - \frac{1}{2}M_0^2\,, \qquad \dot{M}_1 = M_0\,,$$

governing the time evolution of the moments

$$M_0(t) = \int_0^\infty f(t,x)dx, \quad M_1(t) = \int_0^\infty xf(t,x)dx\,.$$

Note that the total particle number M_0 is influenced by nucleation and coagulation, and the total mass M_1 only by the transport. The total particle number tends to the limit $\sqrt{2f_0}$ as $t \to \infty$, and the total mass grows at an asymptotically linear rate.

Constant transport velocity and multiplicative coagulation rate. For $v \equiv 1$ and $K(x,y) = xy$, the equations for the moments are again a closed system:

$$\dot{M}_0 = f_0 - \frac{1}{2}M_1^2\,, \qquad \dot{M}_1 = M_0\,,$$

and differentiating the equation for M_1 yields the second-order Hamiltonian ODE

$$\ddot{M}_1 = f_0 - \frac{1}{2}M_1^2\,, \tag{3.2}$$

with the first integral

$$H = \frac{1}{2}\left(\dot{M}_1\right)^2 - f_0 M_1 + \frac{1}{6}M_1^3\,,$$

whose value is determined by the initial data. The solution of the first order ODE

$$\dot{M}_1 = \sqrt{2H + 2f_0 M_1 - \frac{1}{3}M_1^3}$$

increases and reaches the zero of the right hand side in finite time T because of the square root. At time T with $M_0(T) = 0$ and $M_1(T) > 0$ the model breaks down, which signals the occurrence of *gelation* in finite time, i.e. all the mass has been moved to $x = \infty$ at $t = T$.

Choosing a transport velocity with changing sign. The observations from above remain true. Changes of the total particle number are caused by nucleation and coagulation, and changes of the total mass by the transport:

$$\dot{M}_0 = v(0)f_0 - \frac{1}{2}\int_0^\infty \int_0^\infty K(x,y)f(x)f(y)dx\,dy\,, \qquad \dot{M}_1 = \int_0^\infty vf\,dx\,, \tag{3.3}$$

where in the first equation we have assumed that the flux at infinity vanishes, i.e.,

$$\lim_{x\to\infty} v(x)f(x,t) = 0\,. \tag{3.4}$$

Therefore a steady state needs to balance nucleation and coagulation, but also the production and consumption of monomers by the transport process. Obviously, the transport velocity needs to change sign such that the right hand side of the second

equation can vanish. The simplest possible model assumes the existence of an equilibrium size $x_0 > 0$ such that

$$\begin{aligned} v(x) &> 0\,, \qquad \text{for } 0 \le x < x_0\,, \\ v(x_0) &= 0\,, \qquad \text{for } x_0 > 0\,, \\ v(x) &< 0\,, \qquad \text{for } x > x_0\,. \end{aligned} \tag{3.5}$$

For well-posedness of the problem, this requires an additional boundary condition at $x = \infty$, such as (3.4). More generally, we shall pose

$$\lim_{x\to\infty} v(x)f(x,t) = j_\infty \le 0\,, \tag{3.6}$$

where $j_\infty < 0$ could be interpreted as nucleation of infinite size particles out of a background gel.

3 The inverse problem – explicit examples of steady state solutions

As a source of illustrative explicit examples we consider the inverse problem of prescribing a steady state $f(x)$ and determining corresponding transport velocities $v(x)$, such that

$$\partial_x\Big(v(x)f(x)\Big) = \frac{1}{2}\int_0^x K(x-y,y)f(x-y)f(y)dy - \int_0^\infty K(x,y)f(y)f(x)dy\,. \tag{3.7}$$

Obviously, $v(x)$ is only unique up to adding multiples of $1/f(x)$. We shall be interested in those solutions with minimal growth of $|v(x)|$ as $x \to \infty$, since we are mainly interested in the question, how much growth of $|v(x)|$ is needed for a certain decay behavior of $f(x)$. Another way of enforcing the requirement of minimal growth is to choose $j_\infty = 0$ in (3.6). The steady states considered in this section are by construction very special concerning their behavior close to zeroes of v, since the results of the following section will show that, in general, singularities have to be expected there.

Exponential steady states. For $f(x) = f_0 e^{-\lambda x}$, $\lambda > 0$, (3.7) becomes

$$v' - \lambda v = \frac{f_0}{2}\int_0^x K(x-y,y)dy - f_0\int_0^\infty K(x,y)e^{-\lambda y}dy\,.$$

If K is polynomial, so is the right hand side, and a polynomial solution v (which is in this case the one we are looking for) can be found by an ansatz. This is how we proceed in the first three examples below.

1. $K(x,y) = 2$: $\quad v(x) = \frac{f_0}{\lambda}\left(\frac{1}{\lambda} - x\right)$.

2. $K(x,y) = x + y$: $\quad v(x) = \frac{f_0}{2\lambda}\left(\frac{\sqrt{2}}{\lambda} + x\right)\left(\frac{\sqrt{2}}{\lambda} - x\right)$.

3. $K(x,y) = xy$: $\quad v(x) = \frac{f_0}{12\lambda^4}\left(6 + 6\lambda x - 3(\lambda x)^2 - (\lambda x)^3\right)$.
   It can be easily checked that v satisfies (3.5), as obviously also in the previous 2 examples. In all 3 examples so far the polynomial degree of v is by one higher than the polynomial degree of K.

4. For $K(x,y) = (xy)^\alpha$, $\alpha > 0$, we have to solve
$$v' - \lambda v = \frac{f_0}{2} B(\alpha+1, \alpha+1) x^{1+2\alpha} - \frac{f_0}{\lambda^{\alpha+1}} \Gamma(\alpha+1) x^\alpha \,, \tag{3.8}$$
   with the Beta-function B and the Gamma-function Γ. At least formally, it is straightforward to construct an asymptotic expansion for a solution
$$v(x) = -\frac{f_0}{2\lambda} B(\alpha+1, \alpha+1) x^{1+2\alpha} + O(x^{2\alpha}) \,, \qquad \text{as } x \to \infty \,.$$
   Note that the above mentioned observation $\deg(v) = \deg(K) + 1$ still holds.

Steady states with algebraic decay. We consider (3.7) with $f(x) = f_0(1 + x^\alpha)^{-1}$, $\alpha > 2$ such that the first order moment is finite.

1. For $K(x,y) = 2$ we obtain
$$\frac{1}{f_0}\partial_x\left(\frac{v(x)}{1+x^\alpha}\right) = \int_0^x \frac{1}{(1+(x-y)^\alpha)(1+y^\alpha)}\, dy - \frac{2}{1+x^\alpha}\int_0^\infty \frac{dy}{1+y^\alpha} \,. \tag{3.9}$$
   We shall investigate the asymptotic behavior of the right hand side as $x \to \infty$. This is subtle, since both terms are asymptotically equivalent to
$$\frac{2}{x^\alpha}\int_0^\infty \frac{dy}{1+y^\alpha} \,.$$
   The deviation of the first term from this is given by
$$\begin{aligned}
&2\int_0^{x/2} \frac{1}{(1+(x-y)^\alpha)(1+y^\alpha)}\, dy - \frac{2}{x^\alpha}\int_0^\infty \frac{dy}{1+y^\alpha} \\
&= \frac{2}{x^\alpha}\int_0^{x/2}\left(\frac{x^\alpha}{1+(x-y)^\alpha} - 1\right)\frac{dy}{1+y^\alpha} - \frac{2}{x^\alpha}\int_{x/2}^\infty \frac{dy}{1+y^\alpha} \\
&= \frac{2}{x^\alpha}\int_0^{x/2} \frac{1 - x^{-\alpha} - (1-y/x)^\alpha}{x^{-\alpha} + (1-y/x)^\alpha}\frac{dy}{1+y^\alpha} - \frac{2}{x^\alpha}\int_{x/2}^\infty \frac{dy}{1+y^\alpha} \\
&\approx \frac{2}{x^\alpha}\int_0^{x/2} \frac{\alpha y}{x}\frac{dy}{1+y^\alpha} - \frac{2}{x^\alpha}\int_{x/2}^\infty \frac{dy}{y^\alpha} \approx \frac{2\alpha}{x^{\alpha+1}}\int_0^\infty \frac{y\, dy}{1+y^\alpha} - \frac{2^\alpha}{(\alpha-1)x^{2\alpha-1}} \,.
\end{aligned}$$
   The first term on the right hand side dominates since $\alpha > 2$. For the last term in (3.9) we obtain
$$\frac{2}{1+x^\alpha}\int_0^\infty \frac{dy}{1+y^\alpha} - \frac{2}{x^\alpha}\int_0^\infty \frac{dy}{1+y^\alpha} \approx -\frac{2}{x^{2\alpha}}\int_0^\infty \frac{dy}{1+y^\alpha} \,,$$

which is also dominated by the first term above. Thus,

$$\partial_x \left(\frac{v(x)}{1+x^\alpha} \right) \approx \frac{f_0 \alpha c_\alpha}{x^{\alpha+1}} \qquad \text{with } c_\alpha = 2 \int_0^\infty \frac{y\,dy}{1+y^\alpha}\,.$$

Integration from x to ∞ and subsequent multiplication with $1+x^\alpha$ shows that the transport velocity has to satisfy

$$\lim_{x\to\infty} v(x) = -f_0 c_\alpha\,.$$

2. For $K(x,y)$ and now with the assumption $\alpha > 3$, analogous arguments lead to

$$v(x) \approx -f_0 \bar{c}_\alpha x \quad \text{as } x \to \infty\,, \qquad \bar{c}_\alpha > 0\,.$$

One conclusion of this section is that for $j_\infty = 0$ the forward problem of deducing the decay properties of steady states from the behavior of the transport velocity is rather subtle. The growth of the velocity at infinity is related to the type of decay behavior, but the rate constants depend on the coefficient.

4 Existence and properties of steady states

The stationary transport coagulation problem with multiplicative kernel reads

$$\begin{aligned} &\partial_x(v(x)f(x)) = \tfrac{1}{2}\int_0^x (x-y)f(x-y)yf(y)dy - \int_0^\infty xf(x)yf(y)dy\,, \\ &f(0) = f_0\,. \end{aligned} \tag{3.10}$$

As explained in Section 2, to ensure the existence of non-trivial steady-state solutions, the function $v(x)$ is assumed to exhibit a single transversal sign change, namely

$$v(x) = (x_0 - x)w(x)\,, \qquad w \in C^1([0,+\infty))\,, \qquad w(x) > 0 \quad \text{for } x \geq 0\,. \tag{3.11}$$

We shall look for a solution, where the transport flux $j = vf$ tends to a nonnegative value as $x \to \infty$. Therefore we complete the problem formulation by

$$\lim_{x\to\infty} v(x)f(x) = j_\infty \leq 0\,. \tag{3.12}$$

At first glance it looks wrong to have two boundary conditions for a first order ODE. However, due to the sign change of the velocity, this is a singular ODE, where the problems for $x \in [0, x_0)$ and for $x \in (x_0, \infty)$ can be treated separately. Actually the problem on $[0, x_0)$ is closed and its solution can be seen as data for the problem on (x_0, ∞).

With (3.12), formal integration of (3.10) leads to the equation

$$j_\infty - v(0)f_0 = -\frac{1}{2}M_1[f]^2\,,$$

for the first order moment

$$M_1[f] := \int_0^\infty x f(x) dx \,.$$

Therefore the value $\mathcal{M}_1 := \sqrt{2(v(0)f_0 - j_\infty)}$ will be fixed from now on. For existence of a non-trivial stationary solution, the transport needs to be strong enough to counteract the coagulation. This will be guaranteed by an additional assumption:

$$\exists A > 0,\, \overline{x} > x_0,\, \beta > 2 : \quad v(x) \geq -Ax^\beta \quad \text{for } x \geq \overline{x} \,. \tag{3.13}$$

We now define the notion of weak stationary solutions to the transport coagulation equation (3.10) to be used in the sequel.

Definition 1. *A weak solution of* (3.10), (3.12) *is a function* $f \geq 0$ *such that* $xf \in L^1(\mathbb{R}^+)$ *and*

$$\begin{aligned} &\Phi(\infty) j_\infty - \Phi(0) v(0) f_0 - \int_0^\infty \Phi'(x) v(x) f(x) dx \\ &= \frac{1}{2} \int_0^\infty \int_0^\infty x f(x) y f(y) \Phi(x+y) dx\, dy - \mathcal{M}_1 \int_0^\infty x f(x) \Phi(x) dx \,, \end{aligned}$$

for all $\Phi \in C^1_B([0,\infty))$, *where* Φ' *has compact support.*

The difficulties we face are connected to the singularity at $x = x_0$ and to the behavior as $x \to \infty$. Therefore we first consider a regularized version of (3.10), (3.12) with the transport flux as the unknown:

$$\partial_x j_\varepsilon + \frac{x \mathcal{M}_1}{v_\varepsilon} j_\varepsilon = h\left[j_\varepsilon / v_\varepsilon\right] \,, \tag{3.14}$$

$$j_\varepsilon(0) = v(0) f_0 \,, \qquad j_\varepsilon(1/\varepsilon) = j_\infty \,, \tag{3.15}$$

with $0 < \varepsilon < 1/x_0$, with

$$v_\varepsilon(x) = \begin{cases} v(x) + \varepsilon & \text{for } x \leq x_0 \,, \\ v(x) - \varepsilon & \text{for } x > x_0 \,, \end{cases}$$

implying $|v_\varepsilon| \geq \varepsilon$, and with

$$h[f](x) := \frac{1}{2} \int_0^x (x-y) f(x-y) y f(y) dy \,.$$

This defines j_ε on $[0, 1/\varepsilon]$, and it is extended to $[0,\infty)$ by the definition $j_\varepsilon = 0$ on $(1/\varepsilon, \infty)$. The regularized problem can be written as a fixed point problem:

$$j_\varepsilon(x) = F_\varepsilon[j_\varepsilon](x) := \begin{cases} G_\varepsilon(x,0) v(0) f_0 + \int_0^x G_\varepsilon(x,y) h\left[j_\varepsilon / v_\varepsilon\right](y) dy & \text{for } 0 \leq x \leq x_0 \,, \\ G_\varepsilon(x, 1/\varepsilon) j_\infty - \int_x^{1/\varepsilon} G_\varepsilon(x,y) h\left[j_\varepsilon / v_\varepsilon\right](y) dy & \text{for } x_0 < x \leq 1/\varepsilon \,, \\ 0 & \text{for } x > 1/\varepsilon \,, \end{cases} \tag{3.16}$$

with

$$G_\varepsilon(x,y) = \exp\left(-\mathcal{M}_1 \int_y^x \frac{z}{v_\varepsilon(z)} dz\right) .$$

Formal integration of (3.14) gives

$$j_\infty - v(0)f_0 + \mathcal{M}_1\, M_1[F_\varepsilon[j]/v_\varepsilon] = \frac{1}{2} M_1[j/v_\varepsilon]^2 .$$

This shows that the correct value of the first order moment is preserved by the fixed point map:

$$M_1[j/v_\varepsilon] = \mathcal{M}_1 \quad \Longrightarrow \quad M_1[F_\varepsilon[j]/v_\varepsilon] = \mathcal{M}_1 .$$

Lemma 3. *Let assumption* (3.11) *and* $0 < \varepsilon < 1/x_0$ *hold. Then problem* (3.14) *has a solution* $j_\varepsilon \in C^1([0,x_0]) \times C^1([x_0, 1/\varepsilon])$ *with* $j_\varepsilon/v_\varepsilon \geq 0$, $M_1[j_\varepsilon/v_\varepsilon] = \mathcal{M}_1$, *and*

$$|j_\varepsilon(x)| \leq J := \max\{v(0)f_0, -j_\infty\} + v(0)f_0 - j_\infty , \qquad x \geq 0 . \tag{3.17}$$

Remark 2. *As mentioned earlier, the problem can be separated into two parts. The properties of the solution have to be understood in the sense that the solution can have a jump at* x_0 *with finite one-sided limits.*

Proof. The proof is a rather simple application of the Schauder fixed point theorem. We start with the observation that for $0 \leq y \leq x \leq x_0$ as well as for $x_0 \leq x \leq y$, we have that $G_\varepsilon(x,y)$ is continuously differentiable and satisfies $0 < G_\varepsilon(x,y) \leq 1$. Note that one of these two cases for the arguments of G_ε always holds in (3.16).

The property $j/v_\varepsilon \geq 0$ is obviously preserved by F_ε, and so is $M_1[j/v_\varepsilon] = \mathcal{M}_1$, as derived above. The inequality (3.17) for $F[j]$ is a consequence of the above bound for G_ε and of

$$\int_0^\infty h[f] dx = \frac{1}{2} M_1[f]^2 .$$

Since obviously continuity on $[0,x_0]$ and on $[x_0, 1/\varepsilon]$ is also preserved, we have $F_\varepsilon : B \to B$ with the bounded, closed, convex subset

$$B := \{j \in C([0,x_0]) \times C([x_0,1/\varepsilon]) : \, j/v_\varepsilon \geq 0,\, M_1[j/v_\varepsilon] = \mathcal{M}_1,\, |j| \leq J\}$$

of the Banach space $C([0,x_0]) \times C([x_0,1/\varepsilon])$.

From the differential equation in (3.14) we obtain the bound

$$|F_\varepsilon[j]'(x)| \leq \frac{\mathcal{M}_1 J}{\varepsilon^2} + |h[j/v_\varepsilon](x)| \leq \frac{3\mathcal{M}_1 J}{2\varepsilon^2} ,$$

implying pre-compactness of $F_\varepsilon[B]$ by the Arzela-Ascoli theorem.

It remains to show the continuity of F_ε with respect to the supremum norm. This is obvious, however, since $F_\varepsilon[j]$ depends on j in a smooth way, and by the regularization all the coefficient functions as well as the x-intervall are bounded. Therefore the Schauder theorem can be applied and the proof is complete. □

An existence result for (3.10), (3.12) is achieved by passing to the limit $\varepsilon \to 0$:

Theorem 3. *Let v satisfy (3.11) and (3.13). Then (3.10), (3.12) has a weak solution.*

Proof. Let j_ε be a solution of (3.14) as in Lemma 3. Then $f_\varepsilon := j_\varepsilon / v_\varepsilon$ satisfies

$$\partial_x(v_\varepsilon f_\varepsilon) + x\mathcal{M}_1 f_\varepsilon = h\left[f_\varepsilon\right], \tag{3.18}$$

$$f_\varepsilon(0) = \frac{v(0)f_0}{v_\varepsilon(0)}, \qquad f_\varepsilon(1/\varepsilon) = \frac{j_\infty}{v_\varepsilon(1/\varepsilon)}, \tag{3.19}$$

and, with $f_\varepsilon(x) := 0$ for $x > 1/\varepsilon$, also the weak formulation

$$\begin{aligned} &\Phi(\infty)j_\infty - \Phi(0)v(0)f_0 - \int_0^\infty \Phi'(x)v_\varepsilon(x)f_\varepsilon(x)dx \\ &= \frac{1}{2}\int_0^\infty \int_0^\infty x f_\varepsilon(x) y f_\varepsilon(y)\Phi(x+y)dx\,dy - \mathcal{M}_1 \int_0^\infty x f_\varepsilon(x)\Phi(x)dx\,, \end{aligned} \tag{3.20}$$

with Φ as in Definition 1 and with ε small enough such that $1/\varepsilon$ is outside the support of Φ'.

The properties of v and of the solution of the regularized problem shown in Lemma 3 imply

$$\int_0^\infty f_\varepsilon\,dx \le \frac{x_0}{2}\frac{J}{(x_0 - x_0/2)\min_{[0,x_0/2]} w} + \int_{x_0/2}^\infty \frac{x}{x_0/2} f_\varepsilon\,dx \le \frac{J}{\min_{[0,x_0/2]} w} + \frac{2\mathcal{M}_1}{x_0}\,,$$

and, thus, uniform-in-ε boundedness of f_ε in $L^1(\mathbb{R}^+)$. Since $M_1[f_\varepsilon] = \mathcal{M}_1$, $\{f_\varepsilon\}_\varepsilon$ is a tight family of measures, and there exists by the Prokhorov theorem a weak accumulation point $f \in L^1(\mathbb{R}^+)$ with $xf \in L^1(\mathbb{R}^+)$.

Since xf_ε appears in the weak formulation, we need a little more to pass to the limit there. With $\delta := \beta/2 - 1 > 0$ we have

$$\begin{aligned} \int_0^\infty x^{1+\delta} f_\varepsilon\,dx &= \int_0^{x_0/2} x^{1+\delta} f_\varepsilon\,dx + \int_{x_0/2}^{\overline{x}} x^{1+\delta} f_\varepsilon\,dx + \int_{\overline{x}}^\infty x^{1+\delta} f_\varepsilon\,dx \\ &\le \frac{J(x_0/2)^{1+\delta}}{\min_{[0,x_0/2]} w} + \overline{x}^\delta \mathcal{M}_1 + \frac{J}{A}\int_{\overline{x}}^\infty x^{1+\delta-\beta}dx \\ &= \frac{J(x_0/2)^{\beta/2}}{\min_{[0,x_0/2]} w} + \overline{x}^{\beta/2-1}\mathcal{M}_1 + \frac{J\overline{x}^{1-\beta/2}}{A(\beta/2-1)}\,. \end{aligned}$$

This uniform estimate implies that also $\{xf_\varepsilon\}_\varepsilon$ is tight. We apply again the Prokhorov theorem to a sequence xf_{ε_n}, where $f_{\varepsilon_n} \rightharpoonup f$. For a subsequence, xf_ε converges weakly, and the limit has to be xf. Now we are ready to pass to the limit in (3.20). Since v_ε converges strongly, we have $v_\varepsilon f_\varepsilon \rightharpoonup vf$. Finally, we use that the tensor product of weakly converging measures converges weakly to the tensor product of the limits, which allows to pass to the limit on the right hand side of (3.20). □

4.1 Qualitative properties of steady states

Since the bound (3.17) remains valid in the limit $\varepsilon \to 0$, solutions of (3.10), (3.12) satisfy

$$0 \le f(x) \le \frac{J}{|v(x)|}\,, \qquad x \ge 0\,. \tag{3.21}$$

Therefore (by (3.11)) f has at most one singularity at $x = x_0$. However, close to x_0 the estimate is too pessimistic, since we know that f is integrable. On the other hand, the estimate is sharp (up to the constant) concerning the behavior as $x \to \infty$, as long as $j_\infty < 0$ in (3.12). For $j_\infty = 0$ we refer to the previous section.

We shall get more precise information on the behavior around $x = x_0$ and start with the mild formulation, formally passing to the limit $\varepsilon \to 0$ in (3.16):

$$v(x)f(x) = \begin{cases} G(x,0)v(0)f_0 + \int_0^x G(x,y)h[f](y)dy & \text{for } 0 \le x \le x_0\,, \\ G(x,\infty)j_\infty - \int_x^\infty G(x,y)h[f](y)dy & \text{for } x > x_0\,, \end{cases}$$

with

$$G(x,y) := \exp\left(-\mathcal{M}_1 \int_y^x \frac{z}{v(z)}dz\right)\,.$$

Note that $G(x,\infty)$ is well defined by (3.13). We need properties of G and of $h[f]$:

Lemma 4. *Let v satisfy (3.11). Then there exists a strictly positive function $G_0 \in C((\mathbb{R}^+)^2)$, such that*

$$G(x,y) = G_0(x,y)\left|\frac{x-x_0}{y-x_0}\right|^c \quad \textit{for } x,y \ge 0\,, \qquad \textit{with } c = \frac{\mathcal{M}_1 x_0}{w(x_0)}\,.$$

Proof. The integral in the exponent of $G(x,y)$ can be written as

$$\begin{aligned} \int_y^x \frac{z}{v(z)}dz &= \frac{x_0}{w(x_0)}\int_y^x \frac{1}{x_0 - z}dz + \int_y^x \frac{1}{x_0 - z}\left(\frac{z}{w(z)} - \frac{x_0}{w(x_0)}\right)dz \\ &= \frac{x_0}{w(x_0)}\log\left|\frac{y-x_0}{x-x_0}\right| + b(x,y)\,, \end{aligned}$$

with a continuous function b. This follows from an explicit integration and the smoothness assumption on w, and it completes the proof with $G_0(x,y) = \exp(-\mathcal{M}_1 b(x,y))$. □

Remark 3. *A similar treatment for $G(x,\infty)$ shows that it also behaves like $|x-x_0|^c$ close to $x = x_0$.*

By (3.21) the integrand of $h[f](y)$ has at most two singularities at x_0 and at $y - x_0$. As long as these are different, i.e. $y \ne 2x_0$, they are integrable, since f is. Therefore $h[f](y)$ has at most one (integrable) singularity at $y = 2x_0$. So this does not interfere with the singularity of $G(x,y)$ at $y = x_0$.

Collecting our results, we first observe that the terms resulting from the boundaries contribute to the solution f a behavior like $|x - x_0|^{c-1}$. For the integral terms, there are 3 cases:
a) If $c < 1$, then $|y - x_0|^{-c}$ is integrable at $y = x_0$, and there results another contribution like $|x - x_0|^{c-1}$.
b) If $c = 1$, then we obtain a contribution like $-\log|x - x_0|$.
c) If $c > 1$, the contribution from the integral does not have a singularity.
Obviously these contributions are always the dominant ones. We collect our results:

Behavior of solutions of (3.10)**,** (3.12) **close to $x = x_0$.** The behavior depends on the value of $c = \frac{\mathcal{M}_1 x_0}{w(x_0)}$.

- If $c < 1$, f has a singularity with $f(x) \approx C|x - x_0|^{c-1}$ as $x \to x_0$.
- If $c = 1$, f still has a singularity with $f(x) \approx -C\log|x - x_0|$ as $x \to x_0$.
- If $c > 1$, f is bounded.

5 Numerical results

Since the aggregate size variable x ranges over the unbounded domain $\mathbb{R}_+$, the first step is to restrict the problem to a finite computational domain. A common strategy is to introduce a cutoff by limiting the size variable to a maximal value X, as done for example in [55]. To simulate (3.1), we discretize the truncated domain $[0, X]$ in the following way:

$$t_k = k\Delta t\,, \quad x_j = j\,\Delta x\,, \quad f(j\Delta x, k\Delta t) \approx f_j^k\,, \quad j = 0, .. \bar{j}, .. J\,, \quad x_J = X\,, \quad x_0 = \bar{j}\Delta x\,, \tag{3.22}$$

such that equation (3.1) rewrites as

$$\frac{f_j^{k+1} - f_j^k}{\Delta t} + \frac{F_{j+1}^k - F_j^k}{\Delta x} = \frac{\Delta x}{2}\sum_{i=0}^{j} K_{j-i,i} f_{j-i}^k f_i^k - \Delta x \sum_{i=0}^{J} K_{j,i} f_j^k f_i^k := Q_j^k$$

where the the flux F_j is defined as the following

$$F_{j+1}^k = \begin{cases} v_j f_j^k & \text{if } j < \bar{j}\,, \\ v_{j+1} f_{j+1}^k & \text{if } j > \bar{j}\,, \\ 0 & \text{if } j = \bar{j}\,, \end{cases}$$

with boundary conditions

$$f_0^k = f(0, k\,\Delta t) = f_0 > 0\,, \quad f_J^k = f(J\,\Delta x, k\,\Delta t) = 0\,, \quad \forall k. \tag{3.23}$$

Furthermore, the following CFL condition has to hold

$$\frac{v_j \Delta t}{\Delta x} \geq \max |v(x)| \quad \forall\, 0 \leq x \leq x_J \,. \tag{3.24}$$

We now define the discrete first moment associated to the equation as

$$M_1^k = \Delta x \sum_{j=0}^{J} x_j f_j^k, \tag{3.25}$$

and we check that Q_j^c preserves the first moment M_1^k

$$\begin{aligned} \sum_{j=0}^{J} x_j Q_j^k &= \frac{\Delta x}{2} \sum_{j=0}^{J} x_j \sum_{i=0}^{j} K_{j-i,i} f_{j-i}^k f_i^k - \Delta x \sum_{j=0}^{J} x_j \sum_{i=0}^{J} K_{j,i} f_j^k f_i^k \\ &= \frac{\Delta x}{2} \sum_{j=0}^{J} f_n \sum_{i=0}^{J} (x_i + x_j) K_{i,j} f_i^k \; - \Delta x \sum_{j=0}^{J} x_j \sum_{i=0}^{J} K_{j,i} f_j^k f_i^k = 0 \,, \end{aligned} \tag{3.26}$$

where in the last equality we have used the symmetry of $K_{i,j}$.

5.1 Comparison with exact solutions

As a first step toward the validation of our scheme, we compare the numerical solutions with the explicit steady state solutions computed in Section 3. We consider three cases for which the explicit steady state solution $f_\infty = f_0 e^{-\lambda t}$ is expected. In particular, in the following we will use $\lambda = 1$.

Case $K(x, y) = 2$: Figure 3.1 shows that the numerical steady state solution is in good agreement with the analytically exact steady state solution. The initial profile $f(0, x) = f_0 e^{-(x-10)^2}$ is driven toward smaller x-values by the transport term, causing the largest clusters (those with size major than x_0) to diminish. Initially, all the mass is concentrated around $x = 10$ and, over time, binary coagulation generates additional peaks (blue lines), each resembling the original but at half the previous peak height. Notably, the spacing between these peaks remains unchanged; this is a direct consequence of the constant coagulation kernel. A video with the evolution of the numerical solution is available at:

https://figshare.com/s/1d6205cafe659f22ff31

We simulate the equation for increasingly finer spatial meshes, using $j = 125, 250, 500$. Figure 3.2, shows the evolution in time of the L^1 discrete error norm

$$\epsilon(t^n) = \Delta x \sum_{i=1}^{J} |f_i^n - f_i^\infty| \;,$$

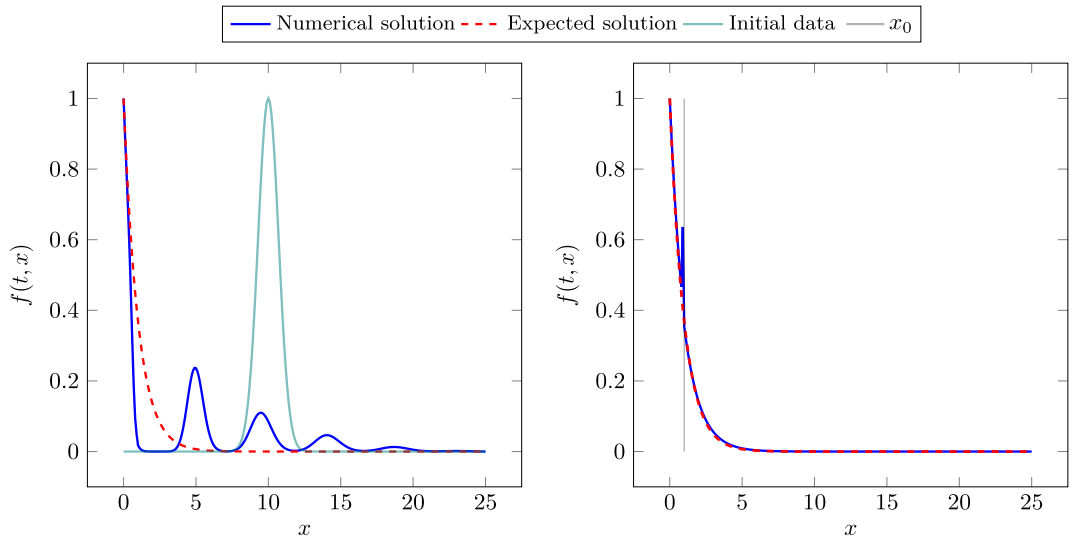

Figure 3.1: Comparison of the numerical and exact steady state solution for $K(x, y) = 2$. The left figure shows the initial profile of the numerical solution (green line), a snapshot of the numerical solution after 200 time steps (blue line), and the exact analytical solution derived in Section 3 (red dashed line). The right figure compares the numerical solution at final time (blue line) and the exact steady state solution computed in Section 4.1 (red dashed line). The peak of the numerical solution on the right at x_0 (gray vertical line) is a numerical error caused by the discontinuity of the numerical flux at x_0. This error diminishes as the spatial grid is refined, as evidenced by the decreasing L^1 discrete error norm plotted in Figure 3.2.

where f_i^n denotes the numerical solution at time step t^n, and f_i^∞ the reference steady-state profile. The error decreases as the mesh size becomes smaller, indicating the convergence of the numerical scheme with respect to the spatial discretization.

Qualitatively similar numerical results are observed for both the linear coagulation kernel $K(x, y) = x + y$ and the multiplicative coagulation kernel $K(x, y) = xy$. The corresponding figures and detailed results are presented in Appendix B.

5.2 Behavior of the numerical solution close to x_0

To gain further insight into the asymptotic behavior of the solution described in Section 4.1, we examine the numerical solution for $K(x, y) = xy$ near x_0, and compare its behavior to the theoretical scenarios corresponding to different values of the parameter $c = \frac{\mathcal{M}_1 x_0}{w(x_0)}$. In the followign we assume that $j_\infty = 0$.

Case $c < 1$: Choosing $v(x) = (1 - x)(1 + x^{3/2})$, one can easily check that $c = \frac{\sqrt{2}}{2} < 1$, hence the steady state solution is expected to behave as $f(x) \approx C|x - x_0|^{c-1}$ near $x = x_0$. Consistent with this analytical result, the numerical solution exhibits a singularity as

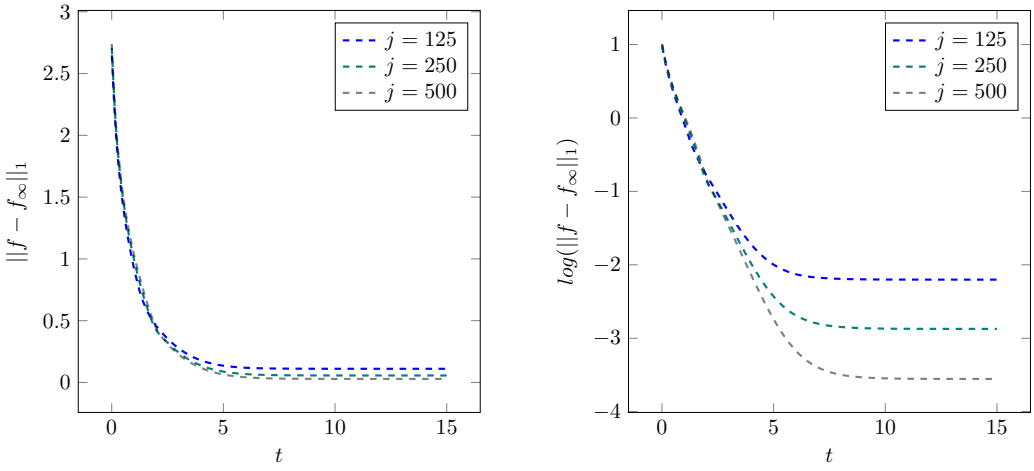

(a) **(b)**

Figure 3.2: Time evolution of the L^1-discrete error norm for $K(x, y) = 2$. (a) Discrete L^1-error in linear scale. The error decreases with respect to smaller values of Δx. The results are showed for $\Delta x = 0.12$ (blue dashed line), $\Delta x = 0.06$ (green dashed line) and $\Delta x = 0.03$ (gray dashed line). **(b)** Discrete L^1-error in semi-log scale, showing polynomial decay in time.

$x \to x_0$, as shown in Figure 3.3a. This figure displays the numerical profile at final time for decreasing values of Δx, showing the formation of a sharp peak near x_0. The maximum value of this peak increases as the Δx decreases, consistent with the presence of a local singularity in x_0. Moreover, in Figure 3.3d we plot the maximum value of the numerical solution as a function of Δx. For the case $c < 1$ (blue line), we observe that this maximum value increases as Δx decreases, providing further numerical evidence for the singular behavior near x_0. A video with the time evolution of the numerical solution is available at:

https://doi.org/10.6084/m9.figshare.29590550.v1

Case $c = 1$: Choosing $v(x) = (1 - x)(0.5 + 0.5x^2)$, one can easily check that $c = 1$, hence the steady state solution is expected to behave as $f(x) \approx -C \log |x - x_0|$ near $x = x_0$. As in the previous case, the behavior of the numerical solution is consistent with the analytical results, indeed it exhibits a singularity as $x \to x_0$, as shown in Figure 3.3.b. We observe that in this case the singularity grows much slower as Δx decreases, in line with the expectation that it should behave like a logarithmic function close to x_0, rather than a polynomial power. The difference with the previous case is more evident in Figure 3.3.d, where we see that the maximum value of the numerical solution increases much slower for

$c = 1$ (red line) rather than for $c < 1$ (blue line) for smaller Δx. A video with the time evolution of the numerical solution is available at:

https://doi.org/10.6084/m9.figshare.29590508.v2

Case $c > 1$: Choosing $v(x) = (1-x)(4-3x+x^2)$, one can easily check that $c = \sqrt{2} > 1$, hence the steady state solution is expected to be bounded near $x = x_0$. Also in this case, the behavior of the numerical solution is consistent with the analytical results, indeed it converges to a finite value as $x \to x_0$, as shown in Figure 3.3.c. We observe that indeed the pick that the solution has close to x_0 becomes smaller as Δx decreases. The convergence to a finite value is more evident in Figure 3.3.d, where we see that the maximum value of the numerical solution decreases with respect to smaller Δx. A video with the time evolution of the numerical solution is available at:

https://doi.org/10.6084/m9.figshare.29591678.v2

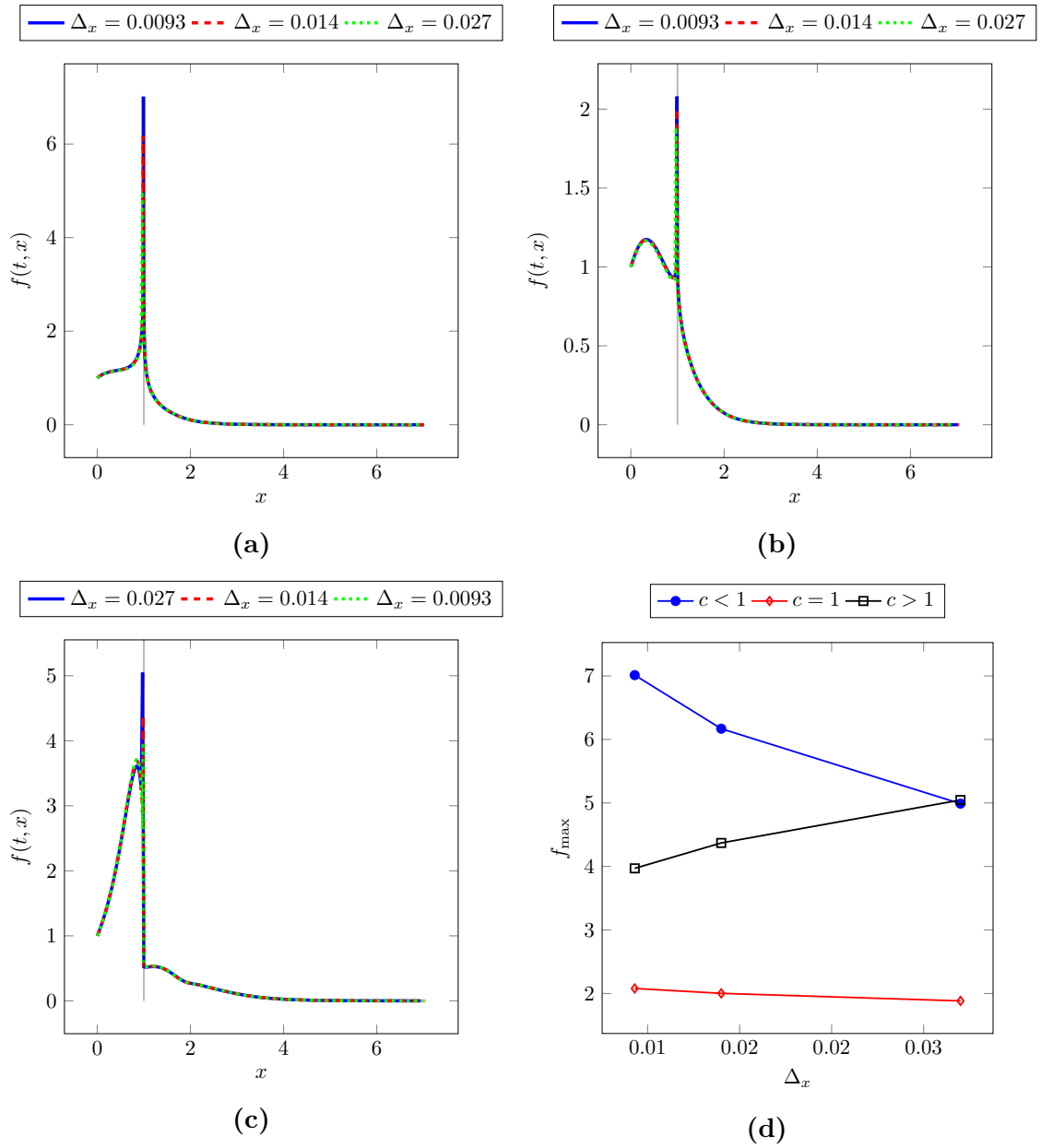

Figure 3.3: Behavior of the numerical solution near x_0 for $K(x,y) = xy$. **(a)** Numerical solution at the final time for different values of Δx, for $c < 1$. The results are shown for $\Delta x = 0.027$ (green dashed line), $\Delta x = 0.014$ (red dashed line), and $\Delta x = 0.0093$ (blue solid line). **(b)** Numerical solution at the final time for different values of Δx, for $c = 1$. **(c)** Numerical solution at the final time for different values of Δx, for $c > 1$. The results are shown for $\Delta x = 0.027$ (blue solid line), $\Delta x = 0.014$ (red dashed line), and $\Delta x = 0.0093$ (green dashed line). **(d)** Plot of the maximum value of the numerical solution at final time near x_0 for different values of Δx. The blue line corresponds to the case $c < 1$, the red line to $c = 1$, and the gray line to $c > 1$.

Chapter 4

Modeling protein diffusion across ER–Nuclear Envelope junctions reveals efficient transport via simple diffusion

Joint work with S. Merino-Aceituno, S. Otsuka, C. Schmeiser and J. Scholz

The endoplasmic reticulum (ER) is the largest continuous membrane-bound organelle in the cell and plays a central role in the synthesis and turnover of many lipids and proteins. It connects directly to the nucleus through specialized contact points known as ER–nuclear envelope (NE) junctions. In our recent study [19], we found that these ER–NE junctions are both narrow and infrequent, measuring less than 20 nanometers in diameter and occurring at a frequency of approximately 0.1 per square micrometer. However, it remains unclear whether such limited and narrow connections are sufficient to support efficient transport between the ER and NE. Here, we built a mathematical model of ER-to-NE protein diffusion, incorporating ultrastructural parameters, the frequency of ER–NE junctions, and the diffusion coefficient of proteins within the ER lumen. To validate the model, we experimentally quantified the transport rate of ER luminal proteins to the NE using fluorescence recovery after photobleaching (FRAP). Our model and experimental data demonstrate that simple diffusion is sufficient to account for the rapid transport of proteins from the ER to the NE, despite the limited and narrow nature of the connecting junctions. Together, these findings offer mechanistic insight into how ER–NE connectivity enables rapid protein transport and lay the groundwork for future studies on ER–nucleus communication.

Contents

1 Introduction 90

2 Materials and methods 91

2.1 Cell culture 91
2.2 Live cell imaging and photobleaching 91
2.3 Quantification of diffusion coefficient and transport rate constant 92
2.4 Shape of ER-NE junctions 92
2.5 The mathematical model 93
3 Results 94
3.1 Live-cell reporters for quantifying luminal protein flux 94
3.2 Quantifying ER-to-NE protein flux using photobleaching 95
3.3 Prediction of the transport rate by the mathematical model . . 95
3.4 Comparison between experimental observations and model predictions 96
4 Discussion 97

1 Introduction

The endoplasmic reticulum (ER) is a central organelle in eukaryotic cells, responsible for protein synthesis and quality control, lipid metabolism, and calcium storage. The nuclear envelope (NE), a specialized subdomain of the ER, encloses the nucleus and plays a crucial role in nucleocytoplasmic transport and gene regulation [53], [99]. The NE comprises inner and outer membranes, with the outer membrane being continuous with the ER [123], [124], [117], [46]. Although the exchange of membrane components and proteins between the ER and NE is vital for cellular homeostasis, the ultrastructural details of the physical connections supporting this exchange have only recently been described [19].

Studies using electron microscopy have revealed that the ER–NE junctions are spatially restricted and structurally narrow, typically less than 20 nm in diameter in plant and mammalian cells [33], [112], [19]. These junctions are also extremely sparse, with a spatial density of approximately 0.1 junctions/μm^2 [19], which is significantly lower than the density of nuclear pores (5–10 pores/μm^2) [96]. These structural constraints raise questions about how efficient transport can be achieved through such geometrically restricted junctions. Specifically, it remains unclear whether these narrow and rare junctions are capable of supporting sufficient luminal protein transport by passive diffusion alone or whether active transport processes might be required.

Previous research on ER luminal transport has largely focused on the mobility within the ER and how it is influenced by the ER architecture [38], [75], [77], [34], [81]. However, the dynamics of luminal transport between the ER and NE remain poorly characterized.

In this study, we address this gap by developing a model of protein diffusion from the ER to the NE. The model incorporates known geometric constraints imposed by the architecture of ER–NE junctions to predict the transport rate of proteins into the NE. To validate the model, we used fluorescence recovery after photobleaching (FRAP) to monitor the dynamics of ER luminal reporters of different sizes in live HeLa cells. By comparing experimental recovery curves to model simulations, we found that passive diffusion alone can account for the observed transport dynamics, even through rare and narrow ER–NE junctions.

2 Materials and methods

2.1 Cell culture

A plasmid encoding moxGFP-KDEL was a gift from Erik Snapp (Addgene plasmid #68072; http://n2t.net/addgene:68072; RRID:Addgene_68072; [32]). To generate NusA-moxGFPx2-KDEL, an HA-tagged NusA fragment was first amplified by PCR from the plasmid encoding 4xHA-NusA (a kind gift from J. Ellenberg lab, European Molecular Biology Laboratory) using the primers 5′-ACGACCGGTA- GCCACCATGGGATATCCCTACG-3′ (forward) and 5′-TCGACCGGTAAGCTTGCCGCTTCGTCA-CCGAACCAG-3′ (reverse). The amplified fragment was then inserted into the moxGFP-KDEL plasmid using AgeI (New England Biolabs). Subsequently, a second moxGFP fragment was amplified from moxGFP-KDEL by PCR using the primers 5′-AGGAAGCTTGGATCCAGTGTCCAAG-GGCGAGGAGCTG-3′ (forward) and 5′-TAGAAGCTTGCCTTGTACAGCTCGTCCATG CCGT-3′ (reverse), and inserted between the HA-NusA and moxGFP-KDEL sequence using HindIII (New England Biolabs).

2.2 Live cell imaging and photobleaching

moxGFP-KDEL was introduced by transient transfection with Lipofectamine 3000 (Thermo Fisher Scientific, L3000001). NusA-moxGFP×2-KDEL was delivered either by transient transfection or via a lentiviral vector system using pMD2.G and pSPAX (gift from R. Foisner lab, Max Perutz Labs). At least 1 hour prior to imaging, cells were washed with 1X PBS (Sigma-Aldrich, D8537-500ML) and the medium was exchanged to imaging media (DMEM without Riboflavin and Phenol Red, Thermo Fisher Scientific, Gibco 041-96205M), containing 10% FBS, 1% penicillin/streptomycin, and 50nM SiR-DNA (Spirochrome, SC007). Image acquisition and photobleaching experiments were performed by spinning disc microscopy (Yokogawa CSU-X1-A1 Nipkow) with a Plan-Apochromat 63x/1.4 NA oil immersion objective (Carl Zeiss), maintained at 37°C with 5% CO2 in

a microscope-body-enclosing incubator. For the control experiment that estimates the bleaching depth, cells were fixed with 4% paraformaldehyde (PFA) in phosphate-buffered saline (PBS) at 37°C for 30 min, followed by replacement with fresh PFA for an additional 30 minutes. After multiple washes in PBS, cells were incubated with imaging media and imaged in 3D using spinning disc microscopy under the following conditions: 69 optical sections, z-stacks every 250 nm, and xy pixel size of 212 nm.

To measure diffusion coefficients, a small region of the ER was photobleached using a 488 nm laser, and images were acquired every 0.25 seconds to monitor fluorescence recovery. For moxGFP-KDEL a square region (4.23 x 4.23 μm) was photobleached, while for NusA-moxGFPx2-KDEL, rectangular regions (1.48 x 5.29 μm or 7.4 x 7.4 μm) were used. For ER-to-NE transport measurements, the entire nucleus was photobleached, and recovery of fluorescence was tracked every 1 second. SiR-DNA signal was simultaneously recorded using a 640 nm laser to define the nuclear periphery for subsequent image analysis.

2.3 Quantification of diffusion coefficient and transport rate constant

We used the ImageJ plugin simFRAP [15] to measure the diffusion coefficient. Briefly, the polygon tool was used to select the whole ER (excluding the nucleus) of the bleached cell and of a reference (unbleached) cell. A rectangle was used to select the bleached area (moxGFP-KDEL: 3.60 $\times$ 3.60 μm, NusA-moxGFPx2-KDEL: 1.27 $\times$ 4.87 μm).

To quantify ER-to-NE transport, fluorescence intensity was measured at each frame of the time-lapse images at the NE. An NE mask with a width of 2 pixels (corresponding to 423 nm) was generated from the SiR-DNA channel, which was first median-filtered (radius = 3) and then thresholded. The intensity values were corrected for photobleaching by using non-bleached cells as a reference after background subtraction. The intensity at the first post-bleach time point was normalized to zero, and the upper plateau that was normalized to the fitted value obtained by applying a single exponential decay model (using a one-phase association in GraphPad Prism version 9.02 for Windows, GraphPad Software, www.graphpad.com). The normalized intensity curves were then aligned to the photobleaching time point and averaged across cells. All image analyses were performed using Fiji [107].

2.4 Shape of ER-NE junctions

3D ultrastructure of ER-NE junctions were visualized using electron tomography and the 3D meshes were generated in a previous study [19]. Cross-sections were taken at regular

intervals along the axis of each 3D junction meshes. The radius was determined from the cross-section with the smallest surface area. To obtain the average junction shape, cross-sectional areas were measured along the junction axis for each mesh and aligned based on their minimal area. The averaged cross-sectional area was then calculated from –2.5 nm to 10 nm along the junction axis. Finally, the area was converted to radius and plotted.

2.5 The mathematical model

The dynamics of the unbleached cargo protein will be described, concentrating on the junctions between ER and NE. The densities within the ER and the NE are assumed to be approximately homogeneous and their values at time t are denoted by $\rho_{ER}(t)$ and $\rho_{NE}(t)$. For simplicity, the junctions are assumed to have identical shapes and equal dynamics, such that it is sufficient to describe one of them. We note that the junction length L is not well defined, as there is no clear criterion for determining where the junction ends. For simplicity, and given the limited knowledge of the precise junction geometry, we assume that L is large compared to the junction width, which allows for a simplified analysis. The diffusion through a junction can then be described by a one-dimensional model, where the protein density $\rho_J(z,t)$ in the junction depends only on the longitudinal variable z, varying between $z = 0$ and $z = L$, corresponding to the connections with the NE and, respectively, the ER. The diffusive flux through the junction cross section at position z and time t is then given by the Fourier law $-DA(z)\frac{\partial \rho_J}{\partial z}(z,t)$ with the diffusivity D and the cross section area $A(z)$. Therefore the one-dimensional density $A\rho_J$ solves the diffusion equation

$$A(z)\frac{\partial \rho_J}{\partial t}(z,t) = \frac{\partial}{\partial z}\left(DA(z)\frac{\partial \rho_J}{\partial z}(z,t)\right). \tag{4.1}$$

The amount of protein in the ER changes only by the flux in and out of the junctions, and therefore

$$V_{ER}\frac{d\rho_{ER}}{dt}(t) = -kDA(L)\frac{\partial \rho_J}{\partial z}(L,t)\,, \tag{4.2}$$

with the total ER volume V_{ER} and with the number k of junctions. Analogously, for the NE:

$$V_{NE}\frac{d\rho_{NE}}{dt}(t) = kDA(0)\frac{\partial \rho_J}{\partial z}(0,t)\,. \tag{4.3}$$

The signs in (4.2) and (4.3) are a consequence of the z-direction pointing into the ER and out of the NE.

The equations (4.1)–(4.3) are a complete model for the densities ρ_J, ρ_{ER}, and ρ_{NE}, if complemented by initial conditions and the natural boundary conditions at the ends of the junction:

$$\rho_J(0,t) = \rho_{NE}(t)\,, \qquad \rho_J(L,t) = \rho_{ER}(t)\,. \tag{4.4}$$

A further simplification results from the fact that the total volume of the ER is much bigger than the volume of the NE, and this in turn is much bigger than the total volume of the junctions. This has the consequence that the differential equations (4.1)–(4.3) act on 3 strongly different time scales. The dynamics in the junctions is much faster than the dynamics in the NE, which in turn is much faster than the dynamics in the ER. Since the experimental observations are concerned with the NE, we concentrate on the intermediate time scale and approximate the fast dynamics in the junctions by a quasistationary model, replacing (4.1) by

$$0 = \frac{\partial}{\partial z}\left(DA(z)\frac{\partial \rho_J}{\partial z}(z,t)\right), \tag{4.5}$$

and the slow dynamics in the ER by

$$\frac{d\rho_{ER}}{dt}(t) = 0\,, \tag{4.6}$$

instead of (4.2).

The model contains all the cross section areas of the junction between the connections to the ER and to the NE. Only an average value will be needed, which is computed by the inverse mean value:

$$\frac{1}{A^*} = \frac{1}{L}\int_0^L \frac{dz}{A(z)}\,. \tag{4.7}$$

The average radius then satisfies the formula $R^{*2}\pi = A^*$. The values for L and R^* in the table are rough estimates, obtained from visual inspection of EM representations of several junctions. For R^*, we use an effective radius defined as the difference between the radius of the junction and that of the reporter, since the reporter's size is of the same order of magnitude as the junction radius. For more details on the model derivation we refer to the appendix, in particular for the derivation of the one-dimensional model (4.1) and the passage from (4.1)–(4.4) to (4.3)–(4.6) by formal asymptotic methods.

3 Results

3.1 Live-cell reporters for quantifying luminal protein flux

We used two reporters of different sizes to quantify protein flux between the ER and NE lumen (Figure 1A). The first is moxGFP, a monomeric GFP variant optimized for oxidizing environments such as the ER [32], fused with the ER retention signal KDEL. This smaller reporter has a molecular weight of approximately 30 kDa. The second, referred to as the larger reporter, consists of two tandem moxGFP fused to the inert, bulky protein NusA and KDEL, with a total molecular weight of about 120 kDa. When expressed in HeLa cells, both reporters showed even localization throughout the ER

and NE (Figure 1B). Photobleaching of small regions within the ER showed that the smaller reporter diffuses rapidly throughout the ER lumen (Figure 1B). Quantification of fluorescence recovery closely matched simulated diffusion kinetics (Figure 1C). The apparent diffusion coefficient was 3.3±1.3 μm^2/sec (mean ± s.d., n = 7 cells), which is consistent with reported values for GFP within the ER [38]. In contrast, the larger reporter had a significantly lower diffusion coefficient of 0.52±0.44μm²/s (n = 17 cells) (Figure 1C), likely due to its elongated shape and increased molecular size. These results show that both reporters serve as effective tools for studying how protein size influences diffusion dynamics within the ER and NE lumen in live cells.

3.2 Quantifying ER-to-NE protein flux using photobleaching

The ER and NE lumen are connected through narrow membranous junctions (Figure 1A). To measure protein flux from the ER to the NE, we photobleached the reporters specifically within the NE, and then monitored how unbleached reporters from the ER accumulate in the NE over time. To ensure complete photobleaching of the entire NE in 3D, we repeated the experiment in fixed cells where no diffusion can occur, and confirmed that our bleaching conditions were effective (Figure 1D). In live cells, both the smaller and larger reporters rapidly diffused into the NE following bleaching. The smaller reporter reached a steady-state level within 20 seconds, while the larger reporter did so within 2 minutes (Figure 1E,F). Given that the junctions connecting the ER to the NE are narrow and infrequent [19], we next investigated whether the observed rapid flux could be explained by passive diffusion alone or whether active transport mechanisms were involved.

3.3 Prediction of the transport rate by the mathematical model

The model (4.3)–(4.6) is simple enough to be solved explicitly. Equation (4.5) implies that the diffusive flux in the junction is independent from the position z:

$$j_J(t) = -DA(z)\frac{\partial \rho_J}{\partial z}(z,t)\,.$$

Division by DA, integration with respect to z, and the boundary conditions (4.4) imply

$$j_J(t) = -DA^* \,\frac{\rho_{ER}(t) - \rho_{NE}(t)}{L}\,,$$

with the average cross section area (4.7). From (4.6) we have

$$\rho_{ER}(t) = \rho_{ER,0}\,,$$

the constant value of the density in the ER. With these results, (4.3) can be written as

$$\frac{d\rho_{NE}}{dt}(t) = \kappa\Big(\rho_{ER,0} - \rho_{NE}(t)\Big)\,, \qquad \text{with } \kappa = \frac{kDA^*}{V_{NE}L}\,. \tag{4.8}$$

If $t = 0$ denotes the end of the bleaching process, implying $\rho_{NE}(0) = 0$, then the solution of this differential equation is given by

$$\rho_{NE}(t) = \rho_{ER,0}\left(1 - e^{-\kappa t}\right)\,,$$

showing that κ is the desired prediction of the transport rate constant.

3.4 Comparison between experimental observations and model predictions

We formulated a mathematical model that describes the flux of proteins between the ER and the NE, using a differential equation and incorporating structural constraints at the ER–NE junctions (Figure 2A, details in Methods). This model assumes uniform protein concentrations within the ER and NE and focuses on protein movement through the junctions. The shape of the junctions were based on our previous measurements [19] (Figure 2B), and we used an averaged geometry for the mathematical model (Figure 2A, right panel). To simplify the analysis, all junctions are assumed to share this average form. Because the junctions are approximated as long and narrow, we modeled them as one dimensional systems where protein movement follows a simplified diffusion equation. We used this model to simulate ER-to-NE diffusion of the two reporters and compared the results with our experimental data. All parameters required for the simulation were either measured experimentally or estimated based on data from previous studies. A summary of the parameter values used in the model is provided in Table 4.1. Because the length and angle of the junctions cannot be clearly determined from our EM images, we treated these features as variables in the model. We then compared the measured flux of ER-luminal reporters to the NE with model simulations at different junction lengths (5, 10, and 20 nm) and membrane angles (0°, 25°, and 50°).

For the smaller reporter, the experimentally measured flux was slightly faster than the simulated values at a junction length of 10 nm and membrane angle of 25°, but remained closely aligned in magnitude (Figure 2C,D). Since these parameters fall within the observed structural range (Figure 2B), the model successfully captures the essential transport dynamics and approximates the correct order of magnitude. For the larger reporter, the measured flux deviates more noticeably from the simulated values, likely due to its elongated shape (Figure 1A). Unlike the globular smaller reporter, an elongated reporter may experience orientation-dependent diffusion, especially near membrane surfaces

Parameter	Value	Description
D_l	$0.52\mu m^2/s$	Diffusion coefficient of a large reporter
D_s	$3.3\mu m^2/s$	Diffusion coefficient of a small reporter
k	40	Number of junctions
V_{ER}	$200\mu m^3$	Total volume of the ER
V_{NE}	$30\mu m^3$	Volume of the NE
L	$5,\ 10,\ 20 \times 10^{-3}$ μm	Height of a junction
R	11×10^{-3} μm	Average radius of a junction
r_l	2.5×10^{-3} μm	Average radius of the small reporter
r_s	1.75×10^{-3} μm	Average radius of the large reporter
α	0°, 25°, 50°	Opening angle of the truncated cone

Table 4.1: Parameters values used in the mathematical model. Apparent diffusion coefficients for the small and large protein reporters were obtained from FRAP measurements (Figure 1B,C). Volumes of the ER and the NE are based on data from volume electron microscopy studies [64], [73]. Junction number and radius were quantified using electron tomography, as described in a previous study [19]. Although two types of junctions were identified in that study (those with and without lumen), only lumen-containing junctions were included in the model, as junctions lacking lumen are unlikely to contribute to luminal ER-to-NE transport. A correction factor was applied to account for a 17% shrinkage caused by the electron microscopy process.

or within confined spaces. Nonetheless, the observed flux of the larger reporter remained within the range of model predictions for junction lengths of 5–10 nm and angles of 25°–50° (Figure 2E,F), suggesting that its ER-to-NE flux can still be explained by simple diffusion. Altogether, these results support the conclusion that simple diffusion is sufficient to explain the rapid transport of proteins from the ER to the NE, despite the narrow and limited geometry of the connecting junctions. We discuss potential biophysical and geometric factors contributing to the slightly faster-than-predicted flux in the Discussion section.

4 Discussion

In this study, we combined live-cell imaging and computational modeling to investigate whether passive diffusion alone can account for luminal protein flux from the ER to NE. Although ER–NE junctions are both narrow and occur infrequently, our results show that simple diffusion is sufficient to explain the observed kinetics of protein accumulation in

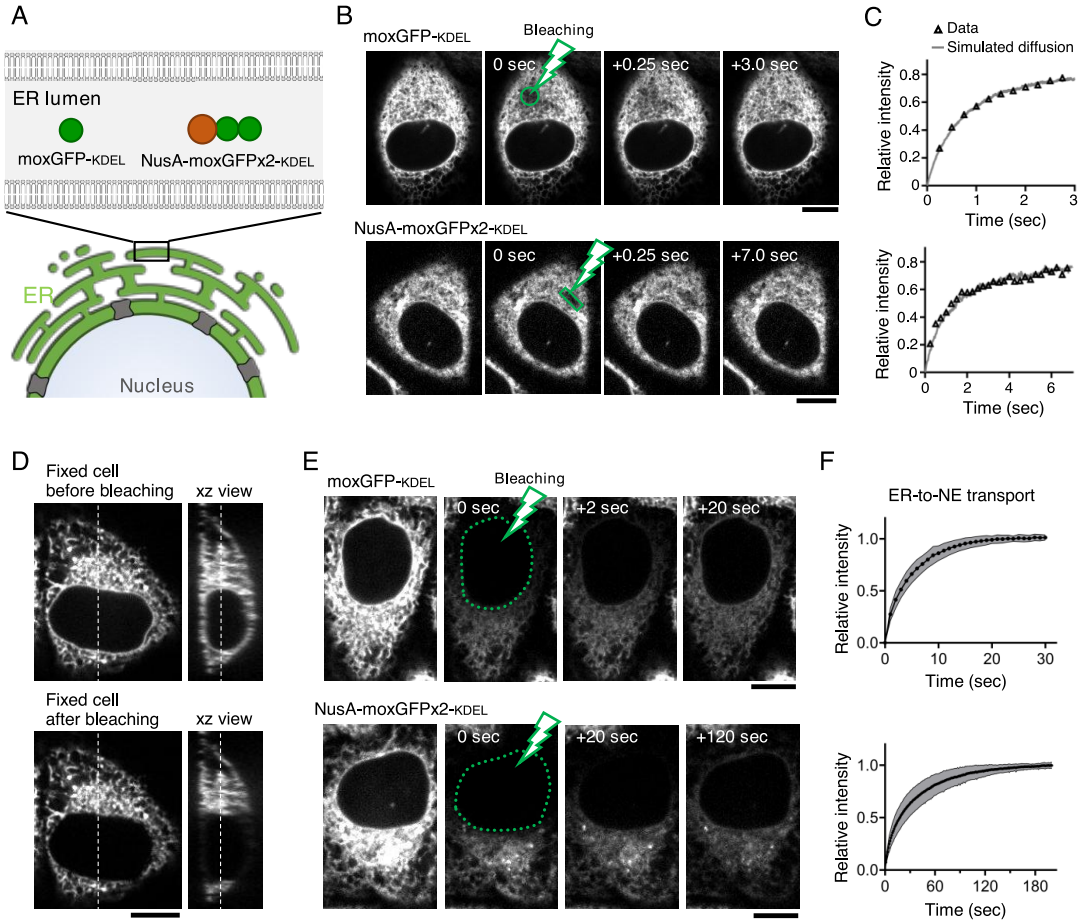

Figure 4.1: Quantifying ER-to-NE transport of luminal proteins. **(A)** Illustration of two reporters used to measure intraluminal protein transport between the ER and NE. **(B)** Representative images of HeLa cells expressing the transport reporters: moxGFP-KDEL (top) and NusA-moxGFPx2-KDEL (bottom). Diffusion within the ER was monitored by photobleaching a small region (indicated by the green line) and tracking fluorescence recovery over time. **(C)** Fluorescence intensity in the bleached area was quantified for moxGFP-KDEL (top) and NusA-moxGFPx2-KDEL (bottom). Experimental data (black triangles) and simulated diffusion curves (gray lines) for the cells shown in (B) are shown. **(D)** Photobleaching in fixed cells to assess the degree of fluorescence loss across the entire NE, serving as a control for ER-to-NE transport measurements. The left panels show a HeLa cell expressing moxGFP-KDEL before (top) and after (bottom) photobleaching the entire NE. Orthogonal views of the indicated positions (white dashed lines) are shown on the right. **(E)** ER-to-NE diffusion of two reporters was monitored following photobleaching of the entire NE, indicated by white dotted lines. **(F)** Fluorescence intensity at the NE was quantified. Black and gray lines represent the mean and standard deviation (s.d.) of measurements from 40 cells across 4 independent experiments for moxGFP-KDEL (top) and 71 cells across 4 independent experiments for NusA-moxGFPx2-KDEL (bottom). Scale bars: 10 μm.

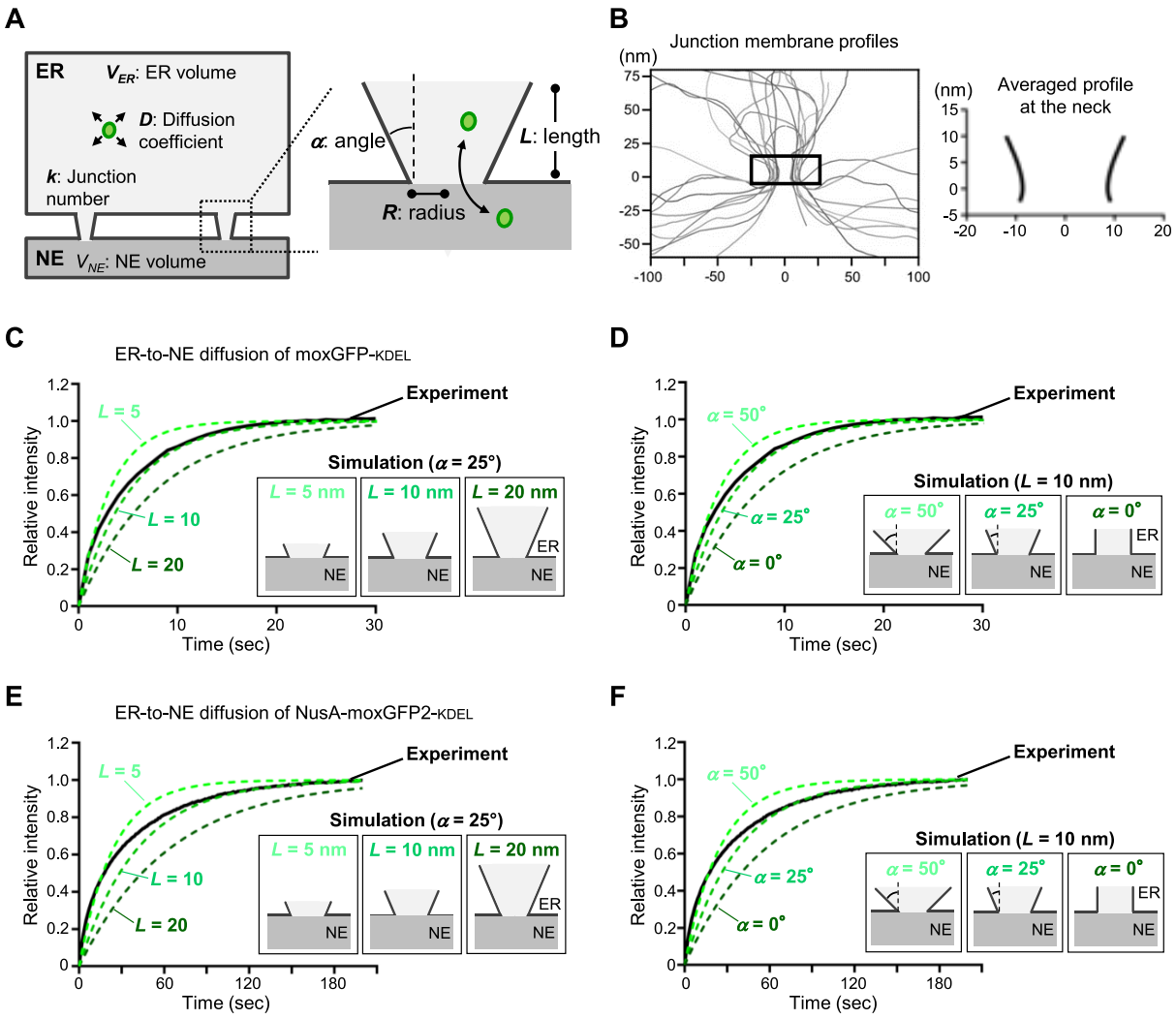

Figure 4.2: The differential equation model with a geometric constraint predicted ER-to-NE flux that closely matches the experimental data. (A) Schematic illustration of the parameters used in the mathematical model. **(B)** Membrane profiles of the ER-NE junction from a previous study [19]. Although two types of junctions were identified in that study (those with a visible lumen and those without), only lumen- containing junctions were included in the model, as the non-luminal junctions are unlikely to support luminal ER-to-NE transport. The averaged shape of the junction neck, highlighted by a bold rectangle in the left panel, is shown in the right panel. **(C,D)** Simulated ER-to-NE diffusion at different junction length **(C)** and membrane angles **(D)** (green dotted lines) compared with experimental data from Figure 1E,F (black solid line) for moxGFP-KDEL. **(E,F)** Simulated ER-to-NE diffusion at different junction length **(E)** and membrane angles **(F)** (green dotted lines) compared with experimental data from Figure 1E,F (black solid line) for NusA-moxGFPx2-KDEL.

the NE following photobleaching. This finding addresses a central question in cell biology: how does luminal communication between the ER and NE occur efficiently despite limited architectural connectivity? While previous studies have described the continuity of the ER and NE [123], [124], [103], [53], [99], whether the continuity enables functionally sufficient transport had not been quantitatively tested. Our FRAP experiments reveal that proteins as large as 120 kDa can reach the NE from the ER within minutes, even when diffusion must occur through rare and narrow junctions. This suggests that the ER–NE system has evolved to permit efficient luminal equilibration without the need for active transport mechanisms.

The mathematical model we developed predicts the correct order of magnitude of the transport rate for both reporters across a physiologically realistic range of junction geometries. However, in both cases, the experimentally observed flux was slightly faster than predicted by the model (Figure 2C–F). These discrepancies are not unexpected, since the model makes several very rough approximations in order to allow for explicit computations. It can be expected to capture the correct order of magnitude of the transport rate rather than precise values. These discrepancies arise not only because of the approximations done in the model, but also from the variability in junction architecture. Indeed, the ER is highly dynamic [94], and we observed considerable variability in the ER membrane morphology adjacent to (approximately 10 nm above) the ER–NE junctions (Figure 2B). These structural fluctuations in junction length or angle could facilitate more efficient diffusion than static geometries allow. Our model assumes steady-state conditions and uniform junction geometry, which may not capture the spatial and temporal heterogeneity of live cells. Additionally, while the FRAP analysis provides robust average measurements of diffusion, it does not resolve single-molecule trajectories or identify subpopulations with distinct diffusion properties. Future studies combining live-cell-compatible super-resolution microscopy, such as MINFLUX [66], combined with single-particle tracking, could provide deeper insights into the dynamics of ER-to-NE transport. From the modeling point of view, the junction geometry enters the theoretical prediction through

$$\frac{A^*}{L} = \left(\int_0^L \frac{dz}{A(z)} \right)^{-1} .$$

From EM representations of junctions, the points of connections with the ER are not clearly defined, resulting in an ambiguity concerning the choice of the junction height L. We claim that this is not a very critical issue. Typically, the junction geometry is conical, and a model of the form $A(z) = (r + z \tan \alpha)^2 \pi$ seems reasonable, with the radius r at the connection to the NE and the opening angle α of the cone. This gives $A^* = r\pi(r + L \tan \alpha)$, and therefore A^*/L tends to the limit $r\pi \tan \alpha$, as L tends to infinity. This shows that the choice of L does not have a strong influence, as long as it is chosen not too small.

Altogether, our results support a simple but robust mechanism of ER-to-NE protein transport driven by passive diffusion. These findings demonstrate that even minimal physical connectivity is sufficient for functionally effective luminal exchange and provide a quantitative basis for future studies exploring how ER–NE transport is modulated under various physiological conditions, developmental stages, or disease states.

Appendices

Appendix A

List of supplementary videos to Chapter 1

The supplementary videos can be found at the following link:

https://figshare.com/s/d31fdf846e210f7ffe13

1 Particle simulations

These videos illustrate the phenomena described in Section 4.2.

Video 1. Video corresponding to Figure 1.1, with parameters described in Table 1.1, and $k_\theta = k_\omega = 1$, $R = 2$. In this regime, the system self-organizes into rotating, cluster-like aggregates. Although all clusters share the same angular velocity (in absolute value), their rotational phases differ, leading to a configuration of multiple rotating clusters without phase synchronization.

Video 2. Video corresponding to Figure 1.2, with parameters described in Table 1.1, and $k_\theta = 21$, $k_\omega = 81$, and $R = 2$. In this regime, the system exhibits a traveling wave configuration in the orientation field while maintaining a nearly uniform spatial distribution.

Video 3. Video corresponding to Figure 1.3, with parameters described in Table 1.1, and $k_\theta = k_\omega = 71$, and $R = 2$. In this regime, the particles are uniformly distributed in space and exhibit collective rotation, moving as a unique rigid body.

Video 4. Time evolution of the microscopic Vicsek–Kuramoto system used for qualitative comparison with the macroscopic simulation in Figure 1.4. The simulation is performed with $N = 2 \cdot 10^4$ particles, alignment strengths $k_\theta = 25.0$, $k_\omega = 50.0$, noise intensities $\sqrt{2\alpha^2} = 2.5$, $\sqrt{2\beta^2} = 2.5$, self-propulsion speed $c = 0.1$, interaction radius $R = 0.04$,

and domain size $L = 1$. In this regime, the system exhibits the same pulsating behavior observed in Video 3. This behavior qualitatively matches the macroscopic dynamics observed when $k_\theta/\alpha^2 = 8$.

2 Macroscopic simulations

Video 5. Time evolution of the macroscopic Vicsek–Kuramoto system simulated with $k_\theta/\alpha^2 = 8$, corresponding to the results shown in Figure 1.4. The color scale represents the density $\rho(x, t)$ of the system.

Video 6. Same simulation as in Video 5. The color scale now represents the average orientation angle $\theta(x, t)$ between $[-\pi, \pi]$.

Appendix B

Supplementary numerical results to Chapter 3

Case $K(x, y) = x + y$: Figure B.1 shows that the numerical steady state solution is in good agreement with the analytically exact steady state solution. The dynamics resemble the case of the constant kernel $K(x, y) = 2$. Initially, most of the mass is concentrated around $x = 10$. Over time, binary coagulation produces additional peaks, which gradually deform and shift toward smaller value of x. Moreover, in this case, the spacing between these peaks is not constant due to the bigger coagulation rate for larger clusters. A video with the evolution of the numerical solution is available at:

https://doi.org/10.6084/m9.figshare.29593238.v1

Case $K(x, y) = xy$: The dynamics observed for the multiplicative kernel closely resemble the case of the additive kernel (see Figure B.3). A video with the time evolution of the numerical solution is available at:

https://doi.org/10.6084/m9.figshare.29593472.v2.

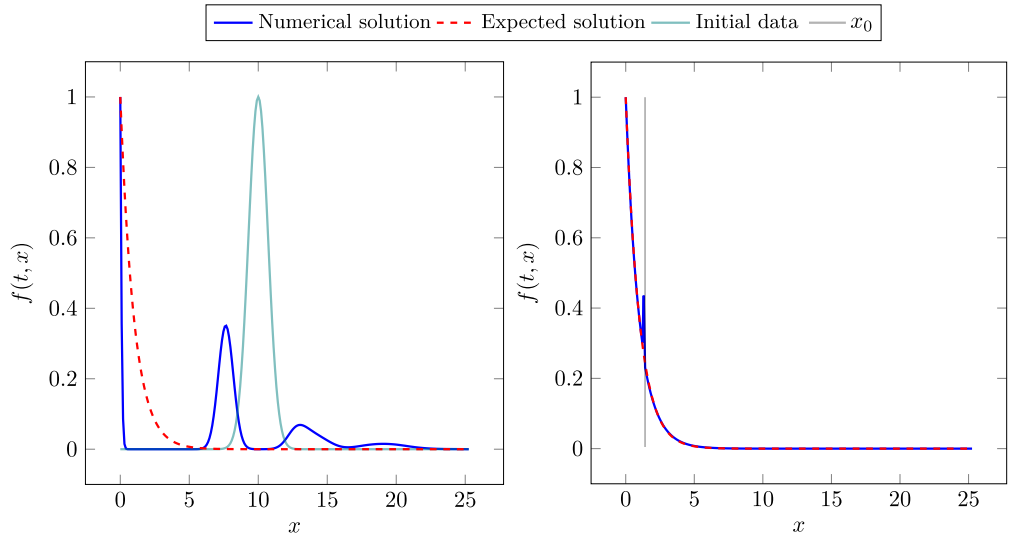

Figure B.1: Comparison of the numerical and exact steady state solution for $K(x,y) = x + y$. The left figure shows the initial profile of the numerical solution (green line), a snapshot of the numerical solution after 200 time steps (blue line), and the exact analytical solution (red dashed line). The right figure compares the numerical solution at final time (blue line) and the exact steady state solution (red dashed line). The peak of the numerical solution on the right at x_0 (gray vertical line) is a numerical error caused by the discontinuity of the numerical flux at x_0. This error diminishes as the spatial grid is refined, as evidenced by the decreasing L^1 discrete error norm plotted in Figure B.2.

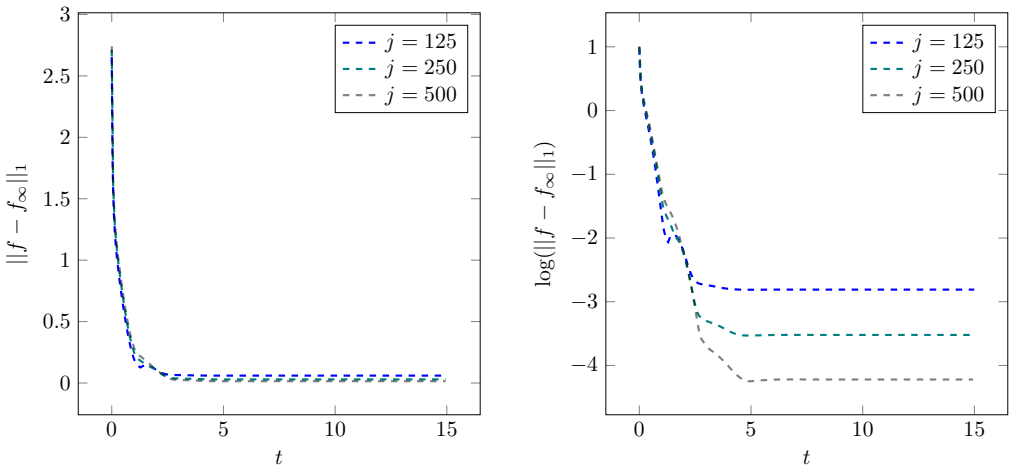

(a) **(b)**

Figure B.2: Time evolution of the L^1-discrete error norm for $K(x,y) = x + y$. **(a)** Discrete L^1-error in linear scale. The error decreases with respect to smaller values of Δx. The results are showed for $\Delta x = 0.12$ (blue dashed line), $\Delta x = 0.06$ (green dashed line) and $\Delta x = 0.03$ (gray dashed line). **(b)** Discrete L^1-error in semi-log scale. Although the error decreases over time, it does not follow a clear decay trend.

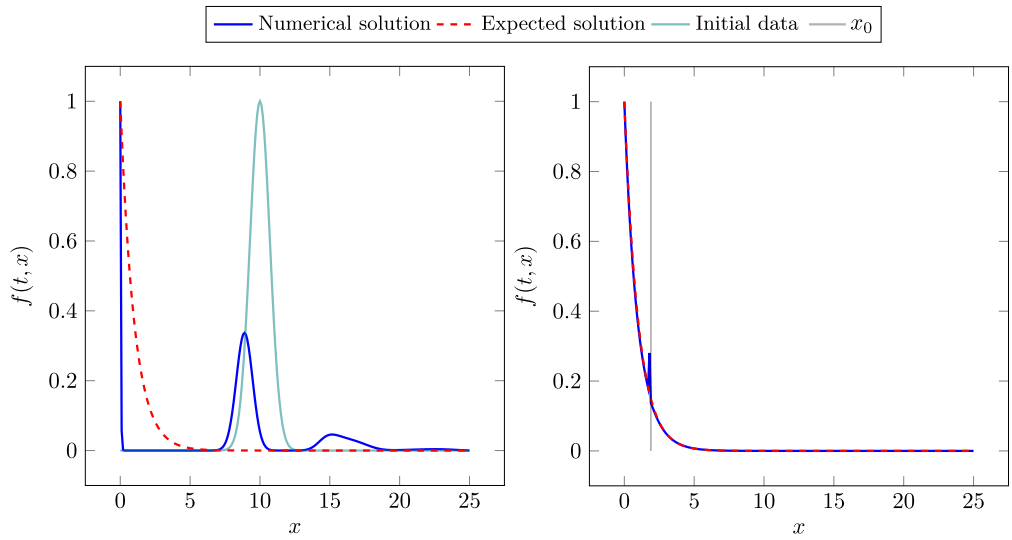

Figure B.3: Comparison of the numerical and exact steady state solution for $K(x,y) = xy$. The corresponding L^1 discrete error norm is plotted in Figure B.4.

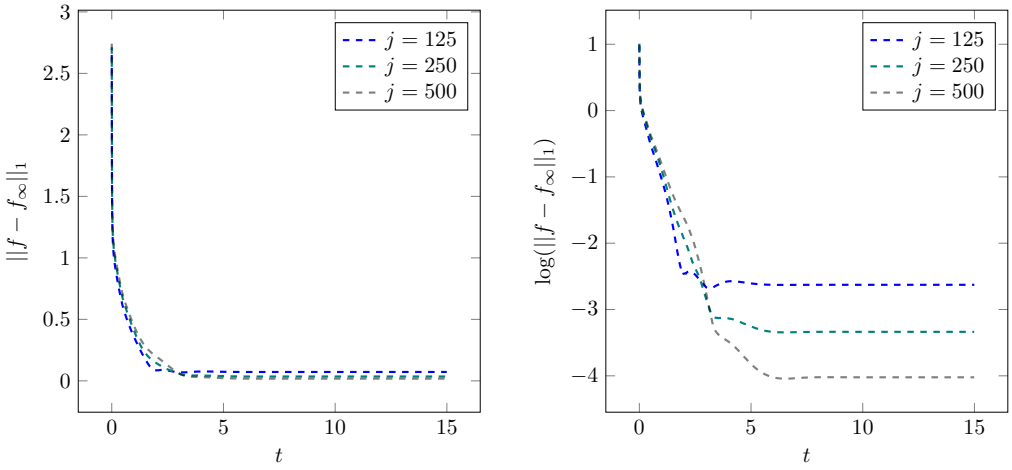

Figure B.4: Time evolution of the L^1-discrete error norm for $K(x,y) = xy$. **(a)** Discrete L^1-error in linear scale. The error decreases with respect to smaller values of Δx. The results are showed for $\Delta x = 0.12$ (blue dashed line), $\Delta x = 0.06$ (green dashed line) and $\Delta x = 0.03$ (gray dashed line). **(b)** Discrete L^1-error in semi-log scale. As in the case of the linear coagulation kernel, the error decreases over time, but it does not follow a clear decay trend.

Appendix C

Derivation of the mathematical model of Chapter 4

The derivation of (4.1) starts with the three-dimensional diffusion equation

$$\frac{\partial \rho_J}{\partial t} = D\Delta\rho_J = D\left(\frac{\partial^2 \rho_J}{\partial x^2} + \frac{\partial^2 \rho_J}{\partial y^2} + \frac{\partial^2 \rho_J}{\partial z^2}\right),$$

holding within the junction, where z is the longitudinal position variable, as above, and cross sections are parallel to the (x, y)-plane. The dimension reduction asymptotics is a classical procedure for problems with extreme aspect ratios. Here we assume that the average radius R^* of the junction is small compared to its height L, i.e., that the aspect ratio $\varepsilon = R^*/L$ is small. In the diffusion equation the position variables and time are non-dimensionalized by

$$(x, y) \to R^*(x, y)\,, \qquad z \to Lz\,, \qquad t \to \frac{L^2}{D}t\,,$$

leading to the scaled version

$$\varepsilon^2 \frac{\partial \rho_J}{\partial t} = \frac{\partial^2 \rho_J}{\partial x^2} + \frac{\partial^2 \rho_J}{\partial y^2} + \varepsilon^2 \frac{\partial^2 \rho_J}{\partial z^2}\,. \tag{C.1}$$

For a thin cross-sectional slice lying between z and $z + h$ (see Figure C.1), changes of mass are due to the flow through the bottom and top cross sections, denoted by $C(z)$ and, respectively, $C(z + h)$.

Mathematically, this is the consequence of applying zero flux boundary conditions along the walls of the junction, integrating (C.1) (divided by ε) over the slice, and using the divergence theorem:

$$\begin{aligned} &\frac{d}{dt}\int_z^{z+h}\int_{C(\zeta)} \rho_J(x, y, \zeta, t)d(x, y)d\zeta \\ &= \int_{C(z+h)} \frac{\partial \rho_J}{\partial z}(x, y, z + h, t)d(x, y) - \int_{C(z)} \frac{\partial \rho_J}{\partial z}(x, y, z, t)d(x, y)\,. \end{aligned} \tag{C.2}$$

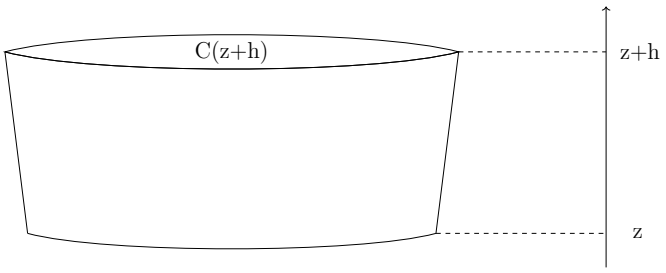

Figure C.1: Cross-sectional slice of a junction

The limit of (C.1) as $\varepsilon \to 0$ is the two-dimensional Laplace (stationary diffusion) equation

$$\frac{\partial^2 \rho_J}{\partial x^2} + \frac{\partial^2 \rho_J}{\partial y^2} = 0\,,$$

which, together with no-flux boundary conditions through the junction walls, implies that the density is independent of (x, y), thus $\rho_J = \rho_J(z, t)$. Therefore, passing to the limit $\varepsilon \to 0$ in (C.2) gives

$$\int_z^{z+h} A(\zeta) \frac{\partial \rho_J}{\partial t}(\zeta, t) d\zeta = A(z+h)\rho_J(z+h, t) - A(z)\rho_J(z, t)\,.$$

The final steps in the derivation of the nondimensionalized version of (4.1) are division by h and passage to the limit $h \to 0$.

The second goal is to derive (4.3)–(4.6) as an approximation for (4.1)–(4.4). Again the first step is a non-dimensionalization (of (4.1)–(4.3)). However, now we concentrate on the time scale relevant for the dynamics in the NE:

$$z \to Lz\,, \qquad t \to \frac{V_{NE} L}{k D A^*} t\,, \qquad A \to A^* A\,.$$

The scaled version of (4.1)–(4.3) then reads

$$\begin{aligned}
\delta_1 A(z) \frac{\partial \rho_J}{\partial t}(z, t) &= \frac{\partial}{\partial z}\left(A(z) \frac{\partial \rho_J}{\partial z}(z, t) \right)\,, \\
\frac{d\rho_{ER}}{dt}(t) &= -\delta_2 A(1) \frac{\partial \rho_J}{\partial z}(1, t)\,, \\
\frac{d\rho_{NE}}{dt}(t) &= A(0) \frac{\partial \rho_J}{\partial z}(0, t)\,,
\end{aligned}$$

with the dimensionless parameters

$$\delta_1 = \frac{kLA^*}{V_{NE}}\,, \qquad \delta_2 = \frac{V_{NE}}{V_{ER}}\,,$$

the ratios of the total junction volume to the NE volume and, respectively, the NE volume to the total ER volume. As mentioned in Section 2, both these ratios are small, justifying the approximation $\delta_1 = \delta_2 = 0$, leading to the scaled version of (4.3)–(4.6).

Bibliography

[1] **Acebrón, J. A., Bonilla, L. L., Pérez Vicente, C. J., Ritort, F., & Spigler, R. (2005)**. The Kuramoto model: A simple paradigm for synchronization phenomena. *Reviews of modern physics*, *77*(1), 137–185 (cit. on pp. 6, 25).

[2] **Ackleh, A. S., & Fitzpatrick, B. G. (1997)**. Modeling aggregation and growth processes in an algal population model: Analysis and computations. *Journal of Mathematical Biology*, *35*, 480–502 (cit. on p. 72).

[3] **Aizenman, M., & Bak, T. (1979)**. Convergence to equilibrium in a system of reacting polymers. *Communications in Mathematical Physics*, *65*, 203–230 (cit. on p. 55).

[4] **Aldana, M., Dossetti, V., Huepe, C., Kenkre, V. M., & Larralde, H. (2007)**. Phase transitions in systems of self-propelled agents and related network models. *Physical Review Letters*, *98*(9), 095702 (cit. on pp. 5, 25).

[5] **Ampatzoglou, I., & Pavlović, N. (2021)**. Rigorous derivation of a ternary Boltzmann equation for a classical system of particles. *Communications in Mathematical Physics*, *387*(2), 793–863 (cit. on p. 52).

[6] **Aranson, I., & Tsimring, L. (2005)**. Pattern formation of microtubules and motors: Inelastic interaction of polar rods. *Physical Review E*, *71*(5), 050901 (cit. on p. 52).

[7] **Balagam, R., & Igoshin, O. A. (2015)**. Mechanism for collective cell alignment in myxococcus xanthus bacteria. *PLoS computational biology*, *11*(8), e1004474 (cit. on p. 53).

[8] **Ball, J., & Carr, J. (1990)**. The discrete coagulation-fragmentation equations: Existence, uniqueness, and density conservation. *Journal of Statistical Physics*, *61*, 203–234 (cit. on pp. 52, 53, 55).

[9] **Banasiak, J., Lamb, W., & Laurencot, P. (2019a)**. *Analytic methods for coagulation-fragmentation models, volume ii*. Chapman; Hall/CRC. (Cit. on pp. 18, 72).

[10] **Banasiak, J., Lamb, W., & Laurençot, P. (2019b)**. *Analytic methods for coagulation-fragmentation models, volume i*. Chapman; Hall/CRC. (Cit. on pp. 18, 72).

[11] **Bechinger, C., Di Leonardo, R., Löwen, H., Reichhardt, C., Volpe, G., & Volpe, G. (2016)**. Active particles in complex and crowded environments. *Reviews of modern physics*, *88*(4), 045006 (cit. on p. 3).

[12] **Berg, H. C. (2004)**. *E. coli in motion*. Springer. (Cit. on p. 13).

[13] **Bertin, E., Droz, M., & Grégoire, G. (2009)**. Hydrodynamic equations for self-propelled particles: Microscopic derivation and stability analysis. *Journal of Physics A: Mathematical and Theoretical*, *42*(44), 445001 (cit. on p. 52).

[14] **Billingsley, P. (2013)**. *Convergence of probability measures*. John Wiley & Sons. (Cit. on p. 68).

[15] **Blumenthal, D., Goldstien, L., Edidin, M., & Gheber, L. A. (2015)**. Universal approach to FRAP analysis of arbitrary bleaching patterns. *Biophysical Journal*, *108*(2), 77a (cit. on p. 92).

[16] **Bobylev, A., Carrillo, J., & Gamba, I. (2000)**. On some properties of kinetic and hydrodynamic equations for inelastic interactions. *Journal of Statistical Physics*, *98*, 743–773 (cit. on p. 52).

[17] **Bolley, F., Cañizo, J., & Carrillo, J. (2012)**. Mean-field limit for the stochastic Vicsek model. *Applied Mathematics Letters*, *25*(3), 339–343 (cit. on pp. 25, 29, 52).

[18] **Boltzmann, L. (1872)**. *Weitere studien über das wärmegleichgewicht unter gasmolekülen* (Vol. 66). Aus der kk Hot-und Staatsdruckerei. (Cit. on p. 9).

[19] **Bragulat-Teixidor, H., Ishihara, K., Szücs, G. M., & Otsuka, S. (2024)**. The endoplasmic reticulum connects to the nucleus by constricted junctions that mature after mitosis. *EMBO reports*, *25*(7), 3137–3159 (cit. on pp. 89, 90, 92, 95–97, 99).

[20] **Briant, M., Diez, A., & Merino-Aceituno, S. (2022)**. Cauchy theory for general kinetic Vicsek models in collective dynamics and mean-field limit approximations. *SIAM Journal on Mathematical Analysis*, *54*(1), 1131–1168 (cit. on p. 52).

[21] **Calvez, V., Raoul, G., & Schmeiser, C. (2014)**. Confinement by biased velocity jumps: Aggregation of escherichia coli. *arXiv preprint arXiv:1404.0643* (cit. on pp. 13, 52).

[22] **Carlen, E., Carvalho, M., Degond, P., & Wennberg, B. (2015)**. A Boltzmann model for rod alignment and schooling fish. *Nonlinearity*, *28*(6), 1783 (cit. on p. 52).

[23] **Carmona, R. (2016)**. *Lectures on bsdes, stochastic control, and stochastic differential games with financial applications*. SIAM. (Cit. on p. 29).

[24] **Carrillo, J., & Toscani, G. (2007)**. Contractive probability metrics and asymptotic behavior of dissipative kinetic equations. *Rivista di Matematica della Università di Parma, Series 7*, *6*, 75–198 (cit. on p. 52).

[25] **Carrillo, J. A., D'Orsogna, M. R., & Panferov, V. (2009)**. Double milling in self-propelled swarms from kinetic theory. *Kinet. Relat. Models*, *2*(2), 363–378 (cit. on p. 26).

[26] **Cercignani, C., Illner, R., & Pulvirenti, M. (2013)**. *The mathematical theory of dilute gases*. Springer Science & Business Media. (Cit. on pp. 51, 52).

[27] **Cercignani, C. (1988)**. *The Boltzmann equation*. Springer. (Cit. on pp. 3, 14).

[28] **Chaintron, L.-P., & Diez, A. (2021)**. Propagation of chaos: A review of models, methods and applications. ii. applications. *arXiv preprint arXiv:2106.14812* (cit. on p. 9).

[29] **Chaintron, L.-P., & Diez, A. (2022)**. Propagation of chaos: A review of models, methods and applications. i. models and methods. *arXiv preprint arXiv:2203.00446* (cit. on p. 9).

[30] **Chalub, F. A., Markowich, P. A., Perthame, B., & Schmeiser, C. (2004)**. *Kinetic models for chemotaxis and their drift-diffusion limits*. Springer. (Cit. on p. 3).

[31] **Chaté, H., Ginelli, F., Grégoire, G., & Raynaud, F. (2008)**. Collective motion of self-propelled particles interacting without cohesion. *Physical Review E*, *77*(4), 046113 (cit. on pp. 5, 25).

[32] **Costantini, L. M., Baloban, M., Markwardt, M. L., Rizzo, M., Guo, F., Verkhusha, V. V., & Snapp, E. L. (2015)**. A palette of fluorescent proteins optimized for diverse cellular environments. *Nature Communications*, *6*, 7670 (cit. on pp. 91, 94).

[33] **Craig, S., & Staehelin, L. A. (1988)**. High pressure freezing of intact plant tissues: Evaluation and characterization of novel features of the endoplasmic reticulum and associated membrane systems. *European Journal of Cell Biology*, *46*(1), 81–93 (cit. on p. 90).

[34] **Crapart, C. C., Scott, Z. C., Konno, T., Sharma, A., Parutto, P., Bailey, D. M. D., Westrate, L. M., Avezov, E., & Koslover, E. F. (2024)**. Luminal transport through intact endoplasmic reticulum limits the magnitude of localized ca^{2+} signals. *Proceedings of the National Academy of Sciences of the United States of America*, *121*(13), e2312172121 (cit. on p. 90).

[35] **Cucker, F., & Smale, S. (2007)**. Emergent behavior in flocks. *IEEE Transactions on automatic control*, *52*(5), 852–862 (cit. on pp. 5, 6).

[36] **Cumin, D., & Unsworth, C. (2007)**. Generalising the Kuramoto model for the study of neuronal synchronisation in the brain. *Physica D: Nonlinear Phenomena*, *226*(2), 181–196 (cit. on p. 7).

[37] **Davis, J. R., Luchici, A., Mosis, F., Thackery, J., Salazar, J. A., Mao, Y., Dunn, G. A., Betz, T., Miodownik, M., & Stramer, B. M. (2015)**. Inter-cellular forces orchestrate contact inhibition of locomotion. *Cell*, *161*(2), 361–373 (cit. on p. 13).

[38] **Dayel, M. J., Hom, E. F. Y., & Verkman, A. S. (1999)**. Diffusion of Green Fluorescent Protein in the aqueous-phase lumen of endoplasmic reticulum. *Biophysical Journal*, *76*(5), 2843–2851 (cit. on pp. 90, 95).

[39] **Degond, P., Diez, A., & Walczak, A. (2022)**. Topological states and continuum model for swarmalators without force reciprocity. *Analysis and applications*, *20*(06), 1215–1270 (cit. on p. 26).

[40] **Degond, P., Dimarco, G., & Mac, T. B. N. (2014)**. Hydrodynamics of the Kuramoto–Vicsek model of rotating self-propelled particles. *Mathematical Models and Methods in Applied Sciences*, *24*(02), 277–325 (cit. on pp. 12, 26, 32).

[41] **Degond, P., Frouvelle, A., & Liu, J.-G. (2015)**. Phase transitions, hysteresis, and hyperbolicity for self-organized alignment dynamics. *Archive for Rational Mechanics and Analysis*, *216*(1), 63–115 (cit. on pp. 5, 25).

[42] **Degond, P., & Motsch, S. (2008)**. Continuum limit of self-driven particles with orientation interaction. *Mathematical Models and Methods in Applied Sciences*, *18*(supp01), 1193–1215 (cit. on pp. 5, 10, 11, 25, 32–34).

[43] **Degond, P., & Motsch, S. (2011)**. A macroscopic model for a system of swarming agents using curvature control. *Journal of Statistical Physics*, *143*(4), 685–714 (cit. on pp. 11, 24, 32).

[44] **Delacour, J., Doumic, M., Martens, S., Schmeiser, C., & Zaffagnini, G. (2022)**. A mathematical model of p62-ubiquitin aggregates in autophagy. *Journal of Mathematical Biology*, *84*(1), 3 (cit. on pp. 16, 17, 72).

[45] **Deng, Y., Hani, Z., & Ma, X. (2025)**. Hilbert's sixth problem: Derivation of fluid equations via Boltzmann's kinetic theory. *arXiv preprint arXiv:2503.01800* (cit. on p. 9).

[46] **Deolal, P., Scholz, J., Ren, K., Bragulat-Teixidor, H., & Otsuka, S. (2024)**. Sculpting nuclear envelope identity from the endoplasmic reticulum during the cell cycle. *Nucleus*, *15*(1), 2299632 (cit. on p. 90).

[47] **Dimarco, G., & Motsch, S. (2016)**. Self-alignment driven by jump processes: Macroscopic limit and numerical investigation. *Mathematical Models and Methods in Applied Sciences*, *26*(07), 1385–1410 (cit. on p. 7).

[48] **Doumic Jauffret, M., & Gabriel, P. (2010)**. Eigenelements of a general aggregation-fragmentation model. *Mathematical Models and Methods in Applied Sciences*, *20*(05), 757–783 (cit. on p. 73).

[49] **Drake, R. L. (1972)**. A general mathematical survey of the coagulation equation. *International Reviews in Aerosol Physics and Chemistry*, *3*, 201–376 (cit. on pp. 18, 72).

[50] **Driver, R., Sasser, D., & Slater, M. (1973)**. The equation $x'(t) = ax(t) + bx(t-\tau)$ with "small" delay. *The American Mathematical Monthly*, *80*(9), 990–995 (cit. on pp. 16, 53).

[51] **Dubovskii, P., Galkin, V., & Stewart, I. (1992)**. Exact solutions for the coagulation-fragmentation equation. *Journal of Physics A: Mathematical and General*, *25*(18), 4737 (cit. on pp. 18, 73).

[52] **Düring, B., & Wolfram, M.-T. (2015)**. Opinion dynamics: Inhomogeneous Boltzmann-type equations modelling opinion leadership and political segregation. *Proceedings of the Royal Society A*, *471*(2182), 20150345 (cit. on pp. 13, 52).

[53] **Ellenberg, J., Siggia, E. D., Moreira, J. E., Smith, C. L., Presley, J. F., Worman, H. J., & Lippincott-Schwartz, J. (1997)**. Nuclear membrane dynamics and reassembly in living cells: Targeting of an inner nuclear membrane

protein in interphase and mitosis. *Journal of Cell Biology*, *138*(6), 1193–1206 (cit. on pp. 90, 100).

[54] **Ferreira, M. A., Lukkarinen, J., Nota, A., & Velázquez, J. J. (2021)**. Stationary non-equilibrium solutions for coagulation systems. *Archive for Rational Mechanics and Analysis*, *240*, 809–875 (cit. on pp. 18, 73).

[55] **Filbet, F., & Laurençot, P. (2004)**. Numerical simulation of the smoluchowski coagulation equation. *SIAM Journal on Scientific Computing*, *25*(6), 2004–2028 (cit. on p. 82).

[56] **Friedlander, S. K. et al. (2000)**. *Smoke, dust, and haze* (Vol. 198). Oxford university press New York. (Cit. on pp. 18, 72).

[57] **Frouvelle, A. (2012)**. A continuum model for alignment of self-propelled particles with anisotropy and density-dependent parameters. *Mathematical Models and Methods in Applied Sciences*, *22*(07), 1250011 (cit. on p. 34).

[58] **Gajewski, H. (1983)**. On a first order partial differential equation with nonlocal nonlinearity. *Mathematische Nachrichten*, *111*(1), 289–300 (cit. on p. 18).

[59] **Gajewski, H., & Zacharias, K. (1982)**. On an initial value problem for a coagulation equation with growth term. *Mathematische Nachrichten*, *109*(1), 135–156 (cit. on p. 18).

[60] **Gallagher, I., Saint-Raymond, L., & Texier, B. (2013)**. *From Newton to Boltzmann: Hard spheres and short-range potentials*. European Mathematical Society. (Cit. on p. 9).

[61] **Gautrais, J., Jost, C., Soria, M., Campo, A., Motsch, S., Fournier, R., Blanco, S., & Theraulaz, G. (2009)**. Analyzing fish movement as a persistent turning walker. *Journal of mathematical biology*, *58*, 429–445 (cit. on pp. 11, 24).

[62] **Ginelli, F. (2016)**. The physics of the Vicsek model. *The European Physical Journal Special Topics*, *225*, 2099–2117 (cit. on p. 25).

[63] **Giri, A. K., Laurençot, P., & Si, S. (2025)**. Well-posedness of the growth-coagulation equation with singular kernels. *Nonlinear Analysis: Real World Applications*, *84*, 104300 (cit. on p. 19).

[64] **Griffiths, G., Warren, G., Quinn, P., Mathieu-Costello, O., & Hoppeler, H. (1984)**. Density of newly synthesized plasma membrane proteins in intracellular membranes: I. stereological studies. *Journal of Cell Biology*, *98*(6), 2133–2141 (cit. on p. 97).

[65] **Gu, F., Guiselin, B., Bain, N., Zuriguel, I., & Bartolo, D. (2025)**. Emergence of collective oscillations in massive human crowds. *Nature*, *638*(8049), 112–119. https://doi.org/10.1038/s41586-024-08514-6 (cit. on p. 1)

[66] **Gwosch, K. C., Pape, J. K., Balzarotti, F., Hoess, P., Ellenberg, J., Ries, J., & Hell, S. W. (2020)**. MINFLUX nanoscopy delivers 3d multicolor nanometer resolution in cells. *Nature Methods*, *17*(2), 217–224 (cit. on p. 100).

[67] **Ha, S.-Y., Kim, H. K., & Ryoo, S.-Y. (2016)**. Emergence of phase-locked states for the Kuramoto model in a large coupling regime. *Communications in Mathematical Sciences*, *14*(4), 1073–1091 (cit. on p. 7).

[68] **Ha, S.-Y., & Liu, J.-G. (2009)**. A simple proof of cucker–Smale flocking dynamics and mean-field limit. *Communications in Mathematical Sciences*, *7*(2), 297–325 (cit. on p. 25).

[69] **Ha, S., & Tadmor, E. (2008)**. From particle to kinetic and hydrodynamic descriptions of flocking. *Kinetic and Related Models*, *1*(3), 415–435 (cit. on p. 25).

[70] **Harvey, C., Morcos, F., Sweet, C., Kaiser, D., Chatterjee, S., Liu, X., Chen, D., & Alber, M. (2011)**. Study of elastic collisions of myxococcus xanthus in swarms. *Physical Biology*, *8*(2), 026016 (cit. on p. 52).

[71] **Haskovec, J. (2013)**. Flocking dynamics and mean-field limit in the Cucker–Smale-type model with topological interactions. *Physica D: Nonlinear Phenomena*, *261*, 42–51 (cit. on p. 6).

[72] **Haskovec, J. (2022)**. Flocking in the Cucker-Smale model with self-delay and non-symmetric interaction weights. *Journal of Mathematical Analysis and Applications*, *514*(1), 126261 (cit. on p. 6).

[73] **Heinrich, L., Bennett, D., Ackerman, D., Park, W., Bogovic, J., Eckstein, N., Petruncio, A., Clements, J., Pang, S., Xu, C. S., Funke, J., Korff, W., Hess, H. F., Lippincott-Schwartz, J., Saalfeld, S., Weigel, A. V., Ali, R., Arruda, R., Bahtra, R., & Nguyen, D. (2021)**. Whole-cell organelle segmentation in volume electron microscopy. *Nature*, *599*, 141–146 (cit. on p. 97).

[74] **Hittmeir, S., Kanzler, L., Manhart, A., & Schmeiser, C. (2021)**. Kinetic modelling of colonies of myxobacteria. *Kinetic and Related Models*, *14*(1), 1–24 (cit. on p. 52).

[75] **Holcman, D., Parutto, P., Chambers, J. E., Fantham, M., Young, L. J., Marciniak, S. J., Kaminski, C. F., Ron, D., & Avezov, E. (2018)**. Single

particle trajectories reveal active endoplasmic reticulum luminal flow. *Nature Cell Biology*, *20*(10), 1118–1125 (cit. on p. 90).

[76] **Horn, F., & Jackson, R. (1972)**. General mass action kinetics. *Archive for Rational Mechanics and Analysis*, *47*, 81–116 (cit. on pp. 55, 66).

[77] **Htet, P. H., Avezov, E., & Lauga, E. (2024)**. Fluid mechanics of luminal transport in actively contracting endoplasmic reticulum. *eLife*, *13*, RP93518 (cit. on p. 90).

[78] **Jiang, N., Xiong, L., & Zhang, T.-F. (2016)**. Hydrodynamic limits of the kinetic self-organized models. *SIAM Journal on Mathematical Analysis*, *48*(5), 3383–3411 (cit. on p. 25).

[79] **Kac, M. (1956)**. Foundations of kinetic theory In *Proceedings of the third berkeley symposium on mathematical statistics and probability*. 171–197. (Cit. on p. 9).

[80] **Kanzler, L., Schmeiser, C., & Tora, V. (2024)**. Two kinetic models for non-instantaneous binary alignment collisions. *Kinetic and Related Models*, *17*(5), 697–712 (cit. on pp. 13, 16, 51–53, 58, 69).

[81] **Konno, T., Parutto, P., Crapart, C. C., Dav'ı, V., Bailey, D. M. D., Awadelkareem, M. A., Hockings, C., Brown, A. I., Xiang, K. M., Agrawal, A., Chambers, J. E., Vander Werp, M. J., Koning, K. M., Elfari, L. M., Steen, S., Metzakopian, E., Westrate, L. M., Koslover, E. F., & Avezov, E. (2024)**. Endoplasmic reticulum morphology regulation by RTN4 modulates neuronal regeneration by curbing luminal transport. *Cell Reports*, *43*(7), 114357 (cit. on p. 90).

[82] **Kurzweil, J. (2006)**. Small delays don't matter. In *Proceedings of the symposium on differential equations and dynamical systems* (pp. 47–49). Springer. (Cit. on pp. 16, 53).

[83] **LeVeque, R. J. (2002)**. *Finite volume methods for hyperbolic problems* (Vol. 31). Cambridge university press. (Cit. on p. 45).

[84] **Liebchen, B., & Levis, D. (2016)**. The rotating Vicsek model: Pattern formation and enhanced flocking in chiral active matter. *arXiv preprint arXiv:1701.00091* (cit. on p. 25).

[85] **Lipavský, P., Špička, V., & Morawetz, K. (1999)**. Noninstantaneous collisions and two concepts of quasiparticles. *Physical Review E*, *59*(2), R1291 (cit. on pp. 52, 69).

[86] **Martinez, L. (2022)**. Celllistmap. jl: Efficient and customizable cell list implementation for calculation of pairwise particle properties within a cutoff. *Computer Physics Communications*, *279*, 108452 (cit. on p. 40).

[87] **Maxwell, J. C. (1867)**. Iv. on the dynamical theory of gases. *Philosophical transactions of the Royal Society of London*, (157), 49–88 (cit. on p. 9).

[88] **McKean Jr, H. P. (1966)**. A class of markov processes associated with nonlinear parabolic equations. *Proceedings of the National Academy of Sciences*, *56*(6), 1907–1911 (cit. on p. 9).

[89] **Merino-Aceituno, S., Plunder, S., Wytrzens, C., & Yoldaş, H. (2025)**. Macroscopic effects of an anisotropic gaussian-type repulsive potential: Nematic alignment and spatial effects. *Mathematical Models and Methods in Applied Sciences* (cit. on p. 25).

[90] **Mischler, S., Mouhot, C., & Ricard, M. R. (2006)**. Cooling process for inelastic Boltzmann equations for hard spheres, part i: The cauchy problem. *Journal of Statistical Physics*, *124*, 655–702 (cit. on p. 52).

[91] **Motsch, S., & Navoret, L. (2011)**. Numerical simulations of a nonconservative hyperbolic system with geometric constraints describing swarming behavior. *Multiscale Modeling & Simulation*, *9*(3), 1253–1275 (cit. on pp. 12, 44).

[92] **Murphy, P., Perepelitsa, M., Timofeyev, I., Lieber-Kotz, M., Islas, B., & Igoshin, O. (2024)**. Breakdown of Boltzmann-type models for the alignment of self-propelled rods. *Mathematical Biosciences*, *376*, 109266 (cit. on p. 52).

[93] **Nagai, K. H., Sumino, Y., Montagne, R., Aranson, I. S., & Chaté, H. (2015)**. Collective motion of self-propelled particles with memory. *Physical review letters*, *114*(16), 168001 (cit. on p. 24).

[94] **Nixon-Abell, J., Obara, C. J., Weigel, A. V., Li, D., Legant, W. R., Xu, C. S., Pasolli, H. A., Harvey, K., Hess, H. F., Betzig, E., Blackstone, C., & Lippincott-Schwartz, J. (2016)**. Increased spatiotemporal resolution reveals highly dynamic dense tubular matrices in the peripheral ER. *Science*, *354*(6311), aaf3928 (cit. on p. 100).

[95] **Oswald, P., & Pieranski, P. (2005)**. *Nematic and cholesteric liquid crystals: Concepts and physical properties illustrated by experiments*. CRC press. (Cit. on p. 53).

[96] **Otsuka, S., Bui, K. H., Schorb, M., Hossain, M. J., Politi, A. Z., Koch, B., Eltsov, M., Beck, M., & Ellenberg, J. (2016)**. Nuclear pore assembly proceeds by an inside-out extrusion of the nuclear envelope. *eLife*, *5*, e19071 (cit. on p. 90).

[97] **Paley, D. A. (2007)**. Stability, convergence, and robustness of power-directed sensor networks. *IEEE Control Systems Magazine*, *27*(4), 89–90 (cit. on pp. 5, 25).

[98] **Parisi, G. (2002)**. Complex systems: A physicist's viewpoint. *arXiv preprint cond-mat/0205297* (cit. on p. 2).

[99] **Pawar, S., & Kutay, U. (2021)**. The diverse cellular functions of inner nuclear membrane proteins. *Cold Spring Harbor Perspectives in Biology*, *13*(9), a040477 (cit. on pp. 90, 100).

[100] **Paxton, W. F., Kistler, K. C., Olmeda, C. C., Sen, A., St. Angelo, S. K., Cao, Y., Mallouk, T. E., Lammert, P. E., & Crespi, V. H. (2004)**. Catalytic nanomotors: Autonomous movement of striped nanorods. *Journal of the American Chemical Society*, *126*(41), 13424–13431 (cit. on p. 24).

[101] **Perthame, B. (2006)**. *Transport equations in biology*. Springer Science & Business Media. (Cit. on p. 72).

[102] **Peruani, F., Deutsch, A., & Bär, M. (2006)**. Nonequilibrium clustering of self-propelled rods. *Physical Review E*, *74*(3), 030904 (cit. on p. 25).

[103] **Powell, L., & Burke, B. (1990)**. Internuclear exchange of an inner nuclear membrane protein (p55) in heterokaryons: *In Vivo* evidence for the interaction of p55 with the nuclear lamina. *Journal of Cell Biology*, *111*(6), 2225–2234 (cit. on p. 100).

[104] **Prokhorov, Y. (1956)**. Convergence of random processes and limit theorems in probability theory. *Theory of Probability & Its Applications*, *1*(2), 157–214 (cit. on p. 67).

[105] **Rackauckas, C., & Nie, Q. (2017)**. Differentialequations.jl–a performant and feature-rich ecosystem for solving differential equations in julia. *Journal of Open Research Software*, *5*(1), 15 (cit. on p. 40).

[106] **Riedel, I. H., Kruse, K., & Howard, J. (2005)**. A self-organized vortex array of hydrodynamically entrained sperm cells. *Science*, *309*(5732), 300–303 (cit. on pp. 11, 25).

[107] **Schindelin, J., Arganda-Carreras, I., Frise, E., Kaynig, V., Longair, M., Pietzsch, T., Preibisch, S., Rueden, C., Saalfeld, S., Schmid, B., Tinevez, J. Y., White, D. J., Hartenstein, V., Eliceiri, K., Tomancak, P., & Cardona, A. (2012)**. Fiji: An open-source platform for biological-image analysis. *Nature Methods*, *9*(7), 676–682 (cit. on p. 92).

[108] **Seinfeld, J. H., & Pandis, S. N. (2016)**. *Atmospheric chemistry and physics: From air pollution to climate change*. John Wiley & Sons. (Cit. on pp. 18, 72).

[109] **Sengers, J. (1973)**. The three-particle collision term in the generalized Boltzmann equation. In *The Boltzmann equation: Theory and applications* (pp. 177–208). Springer. (Cit. on p. 52).

[110] **Shen, J. (2008)**. Cucker–Smale flocking under hierarchical leadership. *SIAM Journal on Applied Mathematics*, *68*(3), 694–719 (cit. on p. 6).

[111] **Spohn, H. (2012)**. *Large scale dynamics of interacting particles*. Springer Science & Business Media. (Cit. on p. 28).

[112] **Staehelin, L. A. (1997)**. The plant ER: A dynamic organelle composed of a large number of discrete functional domains. *The Plant Journal*, *11*(6), 1151–1165 (cit. on p. 90).

[113] **Sumino, Y., Nagai, K. H., Shitaka, Y., Tanaka, D., Yoshikawa, K., Chaté, H., & Oiwa, K. (2012)**. Large-scale vortex lattice emerging from collectively moving microtubules. *Nature*, *483*(7390), 448–452 (cit. on pp. 11, 24, 25).

[114] **Sznitman, A.-S. (1991)**. Topics in propagation of chaos. *Ecole d'été de probabilités de Saint-Flour XIX—1989*, *1464*, 165–251 (cit. on pp. 9, 29).

[115] **Takagi, D., Braunschweig, A. B., Zhang, J., & Shelley, M. J. (2013)**. Dispersion of self-propelled rods undergoing fluctuation-driven flips. *Physical Review Letters*, *110*, 038301 (cit. on p. 24).

[116] **Toscani, G. (2006)**. Kinetic models of opinion formation. *Communications in Mathematical Sciences*, *4*(3), 481–496 (cit. on pp. 3, 52, 53).

[117] **Ungricht, R., & Kutay, U. (2017)**. Mechanisms and functions of nuclear envelope remodelling. *Nature Reviews Molecular Cell Biology*, *18*(4), 229–245 (cit. on p. 90).

[118] **Verhulst, F. (2006)**. *Methods and applications of singular perturbations: Boundary layers and multiple timescale dynamics*. Springer. (Cit. on p. 66).

[119] **Vicsek, T., Czirók, A., Ben-Jacob, E., Cohen, I., & Shochet, O. (1995)**. Novel type of phase transition in a system of self-driven particles. *Physical review letters*, *75*(6), 1226 (cit. on pp. 5, 25, 52).

[120] **Vicsek, T., & Zafeiris, A. (2012)**. Collective motion. *Physics reports*, *517*(3-4), 71–140 (cit. on pp. 5, 25).

[121] **Villani, C. (2002)**. A review of mathematical topics in collisional kinetic theory. *Handbook of mathematical fluid dynamics*, *1*, 71–74 (cit. on p. 69).

[122] **Von Smoluchowski, M. (1906)**. Zur kinetischen theorie der brownschen molekularbewegung und der suspensionen. *Annalen der physik*, *326*(14), 756–780 (cit. on p. 17).

[123] **Watson, M. L. (1955)**. The nuclear envelope. *Journal of Cell Biology*, *1*(3), 257–270 (cit. on pp. 90, 100).

[124] **Whaley, W. G., Mollenhauer, H. H., & Leech, J. H. (1960)**. Some observations on the nuclear envelope. *Journal of Cell Biology*, *8*(1), 233–245 (cit. on pp. 90, 100).

[125] **Wild, E. (1951)**. On Boltzmann's equation in the kinetic theory of gases. *Mathematical Proceedings of the Cambridge Philosophical Society*, *47*(3), 602–609 (cit. on p. 69).

[126] **Zaffagnini, G., Savova, A., Danieli, A., Romanov, J., Tremel, S., Ebner, M., Peterbauer, T., Sztacho, M., Trapannone, R., Tarafder, A. K. et al. (2018)**. P62 filaments capture and present ubiquitinated cargos for autophagy. *The EMBO journal*, *37*(5), e98308 (cit. on p. 17).

[127] **Ziff, R. M. (1980)**. Kinetics of polymerization. *Journal of Statistical Physics*, *23*(2), 241–263 (cit. on pp. 18, 72).